國立臺灣大學理學院化學系

學士班學生論文

Department of Chemistry
College of Science
National Taiwan University
Bachelor Degree Thesis

系統性設計雙極性基質應用在基質輔助雷射脫附質譜游離法

Toward the Rational Design of Universal Dual Polarity Matrix for MALDI Mass Spectrometry

黃鵬軒

Penghsuan Huang

指導教授：徐丞志 博士

Advisor: Cheng-Chih Hsu, Ph.D.

中華民國 109 年 6 月

June 2020

國立臺灣大學學士班學生論文
口試委員會審定書

系統性設計雙極性基質應用在基質輔助雷射脫附質譜游離法
Toward the Rational Design of Universal Dual Polarity Matrix for MALDI Mass Spectrometry

本論文係黃鵬軒君（學號 B05203067）在國立臺灣大學化學系完成之學士班學生論文，於民國 109 年05月05日承下列考試委員審查通過及口試及格，特此證明

口試委員：

（簽名）

（指導教授）

梁文傑

金必耀 劉緒宗

系 主 任： 梁文傑 （簽名）

（是否須簽章依各院系規定）

序言

時光匆匆，還來不及好好享受大學的生活，路就走到了盡頭。細數過去兩年的時間，自從加入 CCH LAB 的那天開始，一直在一個未知的路上往前走，不知道前方會有什麼，縱使數度因為壓力很大，躲在宿舍不想做實驗，可是往往時間到了還是默默將實驗進度補上，繼續往前走，也許是因為自己奴性很重，抑或是真心喜歡著做研究的感覺。

大四這年，可以說是我人生的轉捩點，歷經了許多許多事情，有好的，也有壞的。從系上碩班推甄放榜的那天，跟著實驗室學長姐去系辦詢問結果，卻得到許小姐令人沮喪的結果。以及無論數次翻找正取以及備取名單，上面都找不到我的名字，還因此默默躲在宿舍難過了一個星期。那時的我若不是徐老師和實驗室的大家安慰我要我放下，再努力向前走，也許會一蹶不振吧！後來的我，在大家的扶持之下，更加努力不分日夜和假日地做實驗，只為了讓自己站得更穩，不會再次被擊倒。

感謝這一路走來，總是陪伴在我身邊的人們。其中，特別感謝徐老師對我的栽培，信任我讓我能夠去澳門參加研討會，和將許多重要的任務交付在我身上，更讓我能夠在大四這年就完成了一篇 *Anal. Chem.* 感謝我在 CCH LAB 的另一位人生導師-竹平，讓我在這條路上不怕犯錯地往前走，教會了我好多事情，又為我指引了人生的方向。感謝周老師幫了我很多，為我寫了許多推薦信。感謝引我入門的立恩，總是能作為我的後盾，默默為我做了許多事情，就算後來到了很猛的 Caltech，還是很關心我，在 CCH LAB 沒有你，也就不會有今天的我。感謝 CCH LAB 最凱瑞的興翔，就算自己身兼實驗室裡數不清的任務，還是用著你智商 160 拯救廢廢的我。對於我而言，你就像我的大哥。感謝廷浩，在這條路上給了我好多意見，和陪我打了不少桌球。感謝學姊欣蓓，教會我用 HPLC，還有當我有問題時都能問你，讓我真的很安心。感謝承鈺，實驗室裡的另一個大哥，帶領我走過許多有趣的日子，希望你在 UC Davis 能夠走得順遂，等我如願去了美國再去加州找你。感謝和我一起進來的雅貞和洪鈺，有你們在的這段時光，讓我能夠享受在實驗室裡的溫馨，和大姐姐們的關愛。感謝已經不在實驗室的凱鴻，雖然你總是裝出對我很兇的樣子，可是內心裡總是關心著我這個學弟。感謝心思細

膩的欣媛，忙碌之餘總不忘記關心學弟。感謝致霖，帶著我切片，做許多的實驗，沒想到後來的我竟然會跟著你一起申請美國的學校，一起加油吧。感謝映晨，人很好的實驗室大姊姊，希望你過得很好，早日去歐洲工作或是讀書。感謝羅靖，雖然總是看你很累，但還是會跟我們亂聊天。感謝鐿綾，有你在實驗室裡，大家總是很開心。感謝裴博和呂強，來自對岸的大師們，希望你們未來的教職都能順順利利。感謝厚鈞，在實驗室裡陪我度過許多時光，祝你明年的時候能夠順順利利地畢業。感謝立網，雖然你在實驗室裡的日子不長，可是還是讓我學到很多，還有跟你一起研究攝影的日子，我好開心，畢竟這是我人生中的另一個所愛。感謝威傑，在我大學部專題兩年的時間，和我一起奮鬥過好多個晚上和半夜，為著老師催促的Data 努力，雖然沒法再和你一起讀兩年，但還是在這裡先預祝你碩班順利。感謝中途下車的禹涵，陪我聊天陪我做實驗，有你在的實驗室很開心，永遠不會忘記陪你一起去收油煙的日子 XD 希望你在以後的路上，能夠順順利利，當著讓國家驕傲的米蟲 XD 感謝 Ethan，來自加拿大的你，雖然只是短暫停留，但跟你一起合作很開心，跟你聊天跟你做實驗，都讓我覺得自己很幸福呢！等我去了美國，我們再約那裡見面吧！感謝 Kevin，在實驗室為我們帶來許多歡笑，還有凱瑞我們 QQQ。感謝 Laura，離開家鄉來台灣好辛苦，認真做實驗的你，一定會好好過下去的！加油！感謝學姊汝汝，雖然總是在嗆你，但其實我還是很尊敬你的！希望你接下來都能順利。實驗順利、碩班順利。

感謝其他 CCH LAB 的大家和質譜室的大姊姊們，有你們陪著我走完我剩下的時間，用歡笑和溫馨填滿了我在台大日子，我真的很幸福呢！等我離開這裡之後，應該會很想念這裡吧！

感謝我身邊的朋友們，在我忙碌做實驗的日子，不忘記定時把我拉出去玩，陪我聊天喝酒，希望大家的碩班都能順順利利。感謝每一個你/妳，走出現在我的人生中，沒有你們的支持鼓勵，我撐不到今天。感謝你們！

鵬軒 2020/07/15

中文摘要

基質輔助雷射脫附游離/飛行時間質譜法 (**MALDI-TOF**) 是一種強大的質譜分析方法，具有高通量的游離特性，現今在學界和醫學界經常被用來分析生物分子。由於這種游離方法具備相對容易的操作，以及簡單快速地樣品前處理的特性，至今，**MALDI-TOF** 廣泛在各家醫院被用來鑑定並區分不同的菌相。然而，在使用這項技術上，若想要讓分析物的訊號清晰、訊號雜訊比較大，那選擇一個適合的基質便是一門很大的學問。科學家自從 **MALDI** 在 1985 年被研發出來，便一直對於歸納配對不同分析物所適合的基質有著很大的熱情，如何使用適合的基質讓想看的分析物有較好的游離效率，至今還沒有一個有系統的解釋。在我們的研究當中，我們提供一套有系統的方法設計 **MALDI** 的基質，並且讓這些基質具備有雙極性的特性 (能同時在正離子以及負離子模式使用)。而這套系統性的方法，最終讓我們找到一個化合物適合去分析生物樣品中的生物分子，並且具有高敏度的特性，更能應用在質譜影像的分析，讓我們觀測到化學分子在生物組織二維平面上的分佈。

這項研究當中，我們設計並合成出一系列的新興鄰氨基苯甲酸衍生物 (化合物 **I-IV**)，而其中化合物 **I (COOH-NH$_2$)** 和化合物 **IV (COOH-NHMe)** 被設計同時具有酸和鹼的官能基，讓這兩個分子在 **MALDI** 游離源上具有雙極性的特性，並可以用來作為直譜影像所使用的基質，觀測生物分子的分佈，特別是生物體中的脂質分佈。除了實際應用面外，我們也對於基底研究提出了我們的理論，在 355-nm 波長激發下 (**UV-MALDI** 經常配備的波長) ，系統性地研究化合物 **I-IV** 分子之間的質子化、去質子化和質子轉移能量，並對於基質可能具備有雙極性特性進行解釋，而我們的結果指出這樣的性質來自於分子本身的酸鹼性質。

除此之外，我們在研究中發現，化合物 **IV (COOH-NHMe)** 具有相當好的基質表現，並能成功應用在鼠腦的 **MALDI** 以及 **MALDI** 質譜影像分析，相對於市面上販售的基質能偵測到更多種脂質和蛋白質，這樣的基質表現，讓我們認為化合物 **IV(COOH-NHMe)** 在未來具有潛力成為廣用型雙極性 **MALDI** 基質。

關鍵字：基質輔助雷射脫附游離法、質譜儀、質譜影像、MALDI 基質、雙極性

Abstract

Matrix-assisted laser desorption/ionization time-of- flight (**MALDI-TOF**) is one of the most powerful high-throughput ionization methods in mass spectrometry for detecting biomolecules. With relatively easy and fast sample preparation and analysis, MALDI is now employed in hospitals to differentiate bacteria species. However, different analytes require different matrices to enhance their ionization efficiency. Thus, researchers are often tasked with the difficulty of selecting a proper matrix for their desired analytes. In this work, we will provide some insight towards a systematically designed universal matrix that can be applied to MALDI mass spectrometry imaging (MSI) in both positive and negative ion modes. This deliberate approach led to a compound that is suitable for analyzing the main major biomolecules in tissue samples with high intensity.

In this study, a series of novel anthranilic acid derivatives **I-IV**, of which COOH-NH2 (**I**) and COOH-NHMe (**IV**) are endowed with acid and base bifunctionality, were designed and synthesized for MALDI-TOF mass spectrometry applications in dual polarity molecular imaging of biological samples, particularly for lipids. The heat of protonation, deprotonation and proton transfer reaction as well as the capability of analyzing biomolecules in both positive and negative ion modes for **I-IV** were systematically investigated under standard 355-nm laser excitation. The results indicate correlation between dual polarity and acid-base property. Further, COOH-NHMe (**IV**) showed a unique performance and was successfully applied as the matrix for MALDI-TOF mass spectrometry imaging (MSI) for studying the mouse brain. Our results demonstrate the superiority of COOH-NHMe (**IV**) in detecting more lipid and protein species compared to commercially available matrices. Moreover, MALDI-TOF MSI results were obtained for lipid distributions, making COOH-NHMe (**IV**) a potential next generation universal matrix.

Keywords: MALDI, Mass Spectrometry, MSI, MALDI matrix, Dual-polarity,

Content

LIST OF FIGURES

LIST OF TABLES

Introduction

1-1 Mass Spectrometry

Mass spectrometry (**MS**), with its high sensitivity and selectivity, has been utilized in analyzing chemical molecules over several decades. Owing to the high sensitivity in MS, the acquisitions of low abundance molecules in a mixture become possible.[1] As for its advantages that can detect a wide range of chemicals ranging from small molecules such as carbohydrates to super large proteins, MS nowadays has already become indispensable in chemistry research.

The data provided by MS not only qualitative but also quantitative, which enhances the ability for chemists to have better insight into their desired compounds. Furthermore, MS is famous for its high-throughput property, which displays the capability of untargeted analysis.[2] Every millisecond, hundreds or thousands of pieces of the chemical information are detected by the sensor. This fast analysis process enables MS to accomplish truly real-time analysis.

The recent development of MS with various of different ionization methods, such as electrospray ionization (**ESI**), matrix-assisted laser desorption/ionization (**MALDI**), and desorption electrospray ionization method (**DESI**), enrich the analysis of different categories and types of samples. Also, they thoroughly minimize the sample pretreatment and separation; hence accelerate the duration time of analysis.

1-2 Mass Spectrometry Imaging (MSI)

In recent 10 years, mass spectrometry imaging has significantly improved. Many research fields have been benefited by this emerging technology, such as “Metabolomics”, “Proteomics”, “Pharmacodynamics”, and “Toxicology”.[3–5] The distribution of various compounds on the sample visualize some precious biological information which gives scientists better insight on pathology and suspicious biomarker for diseases.[6–9]

While searching the keyword, “mass spectrometry imaging”, on PubChem online, the number of publications showing in **Table 1** below reveals the increasing trend of publications. Thus, we can know that scientists gradually put more emphasis on this research field.

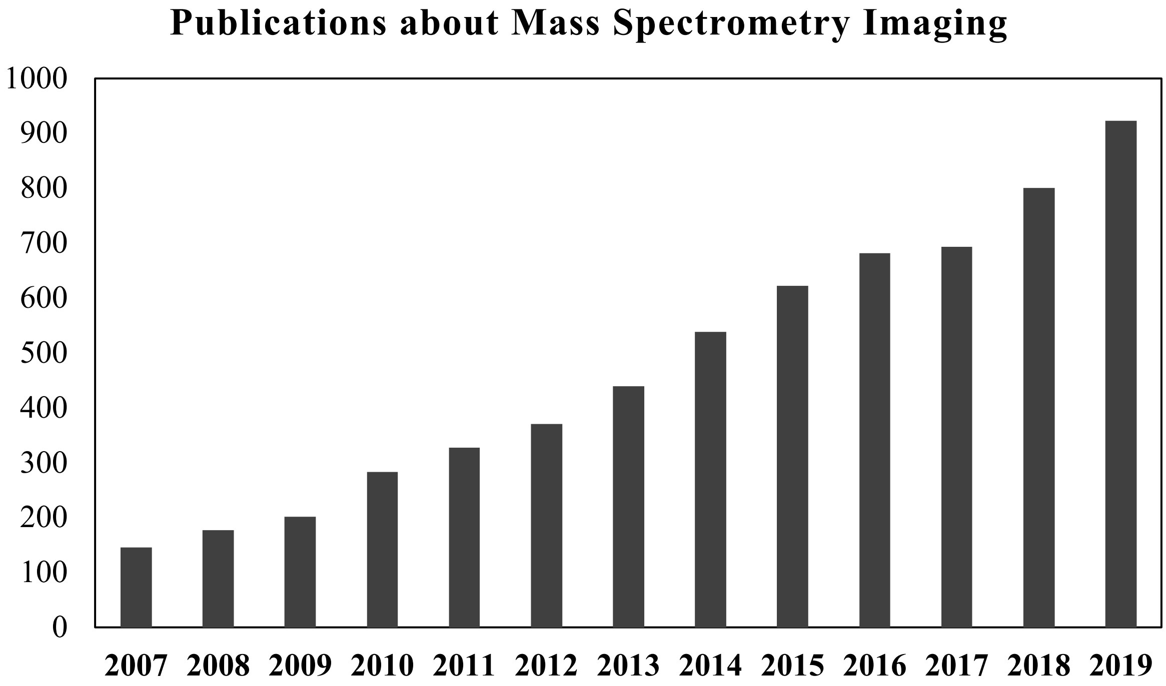

Table 1. Number of recent publications about “mass spectrometry imaging” on PubChem.

Mass spectrometry imaging offers the 2-Dimension biological information on sample sections and depicts the chemical molecules' spatial distribution. By this emerging technology, the changing profiles of metabolites ex vivo nowadays can be realized.

Owing to the "untargeted analysis" advantage of MS, the capability of simultaneous detection with multiple chemical compounds becomes the niche of this technology on metabolomics and proteomics. Taking the commonly used technology - Liquid-Chromatography Mass Spectrometry (**LC-MS**) for instance, LC-MS indeed has this advantage; however, time-consuming, less productivity, and lacking spatial information restrict the knowledge we can get from the samples.

Another technology is called "Immunohistochemistry Staining (**IHC staining**)", this technology traditionally uses the antibodies to identify their desired proteins or antigens and stains the targets with dyes. This method although it can reach the same goal as MSI to plot the distribution of the molecules on samples, the costly antibody and targeted analysis become the shortage of it. Furthermore, the targeted analysis of IHC staining shrinks the detection range of chemicals, and it is really a time-consuming step to search for suitable antibodies and dyes.[10]

Due to these issues, mass spectrometry imaging combining both untargeted and image analysis solves the problems with label-free imaging, offering spatial distribution of chemical molecules; hence, it so far applied to detect cancers and some suspicious biomarkers.

1-3 Matrix-Assisted Laser Desorption/Ionization Method (MALDI)

Since its inception in 1985, matrix-assisted laser desorption/ionization (MALDI) coupled with time-of-flight (**TOF**) has shown great promise for biochemical studies.[11] In 2002, the technique even shared the Nobel Prize in Chemistry with ESI and NMR application on protein structure.[12] With more than three decades of development, MALDI has become one of the most powerful tools for proteomics and lipidomics high-throughput analyses.[13–16] Many research groups have attempted to unveil the mystery behind how the MALDI mechanism works in order to fully realize this technique.[17–19] While these theories propose how the laser and the matrix combined induce the ionization and desorption process, there is no universal explanation to date. Without enough knowledge on the mechanism of MALDI, the development of matrix can only be trial-and-error process.[20] Although nowadays there are many small organic compounds, large molecules with aromaticity characteristic, and nano-particles proposed, the designs of these matrix candidates were only based on their laser absorption capability and ionization efficiency.[21,22] The rest of work to test whether they can serve as MALDI matrix were only confirmed by analytes tests and real samples analysis. In our study, we explored a possible physical chemical reason to explain the desorption/ionization phase. We then employed our theory to successfully design a small organic compound as a MALDI matrix. This matrix has high ionization efficiency, high sensitivity towards analytes, and can simultaneously serve for positive and negative ion mode.

1-4 Application of MALDI on Biological Analysis

Lipids are essential building blocks for cells, storing energy as well as many biological functions, such as cell signaling.[23,24] Their accumulation is highly correlated with many diseases.[25,26] Changes in lipid localization and profile are key features of diseases such as cancer,[25,26] metabolic disorders[27] and neurodegenerative disorders.[28] Molecular imaging techniques of lipid species in tissues are important for researchers to gain insight into the biochemical mechanisms involved and possibly provide clinical evaluations of the disease status.[27] Among these, mass spectrometry imaging (MSI) is a powerful tool for discerning the spatial localization of biomolecules.[29–31] Matrix-assisted laser desorption/ionization time-of-flight (MALDI-TOF) MSI is a high spatial resolution technique capable of analyzing a wide variety of biomolecules simultaneously[32–36] and have been applied in determining biomarkers of diseases and tracking target molecule such as administered drugs.[25,37–41] Imaging of lipid species is one of the most widely utilized applications using MALDI-TOF MSI.[36,424344]

Lipids have diverse chemical structures and many of them are more easily detected in one ionization polarity than the other, positive or negative ion mode. For example, phosphatidylcholines (PC) are typically observed as positive ions, whereas many other lipids, such as phosphatidic acids (PA), phosphatidylethanolamine (PE), phosphatidylserines (PS), phosphatidylinositols (PI) and sulfatides (ST) are usually observed as negative ions in MALDI-TOF MSI.[20] However, most commercial MALDI matrices are only suitable for single polarity detection. For example, 2,5-dihydroxybenzoic acid (2,5-DHB) and α-cyano-4-hydroxybenzoic acid (CHCA) are most often used in positive ion detection because their carboxyl group acts as a proton donor, while 9-aminoacridine (9-AA) is favored in negative ion detection because its amine group acts as the proton acceptor.[20,45] A dual polarity MALDI matrix is one approach that allows universal mass spectrometric analysis of both positively- and negatively-charged lipid species on one sample.

Researchers have discovered a few dual-polarity matrices suitable for MALDI MSI at high spatial resolution. One early example is 1,5-diaminonaphthalene (1,5-DAN) proposed by Thomas *et al*[46–48] and more recently 3-aminophthalhydrazide (luminol) proposed by Li *et al*.[49] However, in both cases, only MSI results of lipids and small metabolites are shown. Their effectiveness for protein and peptide detection not demonstrated. More interestingly, neither of the two compounds possess a carboxylic group for enhanced ionization efficiency in positive ion mode.

To discover a truly universal dual-polarity matrix, we used a rational design approach to determine the most probable matrix candidates before synthesis and experimentation. In essence, an ideal matrix for would have: (i) a high absorption coefficient at the commercial laser wavelength, (ii) a simple and low matrix background below 1000 Da and (iii) the ability to observe both positive and negative lipid ions. Based on these criteria and the dual acid-base functionality, we strategically designed and synthesized a series of new MALDI matrices **I-IV** (see **Scheme 1** in **Results and Discussion** section) containing a simple aniline derivative anchored by a carboxyl group for $COOH-NH_2$ (**I**) and COOH-NHMe (**IV**) , and formyl group for $CHO-NH_2$ **(II)** and CHO-NHAc **(III)**. Though **I-IV** have been synthesized previously, their related application as a MALDI matrix as part of a rationally designed strategy have not been proposed, especially for **II-IV**. [50–53] The amphoteric property of $COOH-NH_2$ (**I**) and COOH-NHMe (**IV**)[54] could allow the detection of both positive and negative ions in MALDI. In this study, we demonstrated that these dual polarity MALDI matrix, $COOH-NH_2$ (**I**) and COOH-NHMe (**IV**), allowed complementary analysis of lipids and proteins, including the positively charged and negatively charged species, within one experiment. Moreover, this novel matrix, COOH-NHMe (**IV**), enables the MSI of phospholipids with enhanced sensitivity as demonstrated from mouse brain sections using MALDI-TOF.

Experimental Section

2-1 Material and Instruments

2,5-DHB and 1,5-DAN were purchased from Tokyo Chemical Industry Co., Ltd. (Tokyo, Japan), while sinapic acid (SA), CHCA and 9-AA were purchased from Sigma-Aldrich (St. Louis, MO, USA). 2',5'-dihydroxyacetophenone (2,5-DHAP) was purchased from Alfa Aesar (Ward Hill, MA, USA), and 2',6'-dihydroxyacetophenone (2,6-DHAP) from Acros Organics (Geel, Belgium). PC(14:0/14:0), PE(14:0/14:0), PA(14:0/14:0), PS(14:0/14:0) and phosphatidylglycerol PG(14:0/14:0) were purchased from Avanti Polar Lipids, Inc. (Alabaster, AL, USA) Mouse brains were purchased from BioLASCO Taiwan Co., Ltd (Taipei, Taiwan). Indium tin oxide (ITO)-coated glass slides were purchased from Ruilong (Taichung, Taiwan). Protein calibration I kit was purchased from Bruker Daltonics (Bremen, Germany). Methanol (MeOH), acetonitrile (ACN), chloroform and ethyl acetate (EA) used as extraction solvent were purchased from Duksan (Korea), J.T. Baker (USA) and Macron (USA), respectively.

The Bruker Autoflex Speed mass spectrometer (Bruker Daltonics, Bremen, Germany) equipped with a Smartbeam II Nd:YAG laser (355 nm) was used in this study. The LC-MS/MS system was a hybrid LTQ-Orbitrap Elite Mass Spectrometer (Thermo Fisher Scientific, Waltham, Massachusetts, US) couple with Vanquish™ Flex Quaternary UHPLC. A sublimation apparatus (Singlong, Taichung, Taiwan) and Leica CM1950 cryostat (Leica Microsystem Inc., Wetzlar, Germany) were used in tissue preparation.

2-2 Sample Preparation

A 0.1 M solution of each matrix was prepared in acetonitrile and water (1:1, v/v). Individual lipid solutions of PS(14:0/14:0), PE(14:0/14:0) and PC(14:0/14:0) at 0.2 mg/mL was prepared in chloroform and methanol (1:1, v/v). A lipid mixture of PS(14:0/14:0), PE(14:0/14:0), PC(14:0/14:0), PA(14:0/14:0) and PG(14:0/14:0) was prepared at the same concentration and in the same solvent system. The protein calibration I kit was dissolved in 150 μL of deionized water to make the protein mixture. The matrix and standard solutions were mixed 1:1 (v/v) and 1.4 μL of each mixture was spotted onto the sample plate and left to air dry. MALDI samples with different pH value were evaluated in **Figure S1-S2**. (See the Figure in **Appendix B**.)

2-3 Tissue preparation for mouse brain extract.

Mouse brains were grounded into powder in liquid nitrogen. The powder was then mixed with MeOH/ACN/EA 10:7:3 (v/v/v) and sonicated for 15 minutes to extract the lipid species. One milliliter of the supernatant was transferred to a clean Eppendorf tube and concentrated to 250 μL under vacuum. The lipid extract was stored under -20°C until needed. Like the standard profile, the matrix and extracts were mixed 1:1 (v/v) and 1.4 μL of the mixture was spotted onto the sample plate and air-dried. The remaining pellet after lipid removal was mixed with 1 mL water/ACN/TFA 50:50:1 (v/v/v) solution and sonicated for 2 minutes to extract the protein species[55]. In this case, the supernatant was transferred to a clean Eppendorf tube and 1 mL of the supernatant was mixed with 10 mL of one of four saturated matrix solutions (COOH-NHMe, 2,5-DHB, 2,5-DHAP and 1,5-DAN) for analysis.

2-4 Tissue preparation for MSI.

A mouse brain was sectioned at 12 μm thickness using a Leica CM1950 cryostat following a previously described protocol.[56] In short, the tissue was sectioned at -20°C and thaw-mounted onto a ITO-coated glass slide. The slides were then stored under -80°C until needed. After desiccation for >30mins, sublimation was carried out using a home-built sublimation system where 0.5mg/cm^2 of matrix was deposited onto the sample at 60 °C with a 0.7 Torr vacuum for 10 seconds.

MALDI-MSI of lipid distribution in a 12-μm thick coronal mice brain section is shown in **Figure 11.** MALDI-MSI of lipid distribution in a 12-μm thick horizontal mice brain section is shown in **Figure S11.** In short, serial sections of mouse brain were thaw-mounted on the same ITO-coated glass slide and stored in -80°C until needed. Prior to matrix deposition by sublimation, tissue sections were thawed in a desiccator for ~30 minutes under reduced pressure. Sublimation was carried out using 150 mg of matrix at 60 °C with a 0.7 Torr vacuum for 10 seconds. Matrix deposition was carried out as mentioned in the manuscript with the 0.5 mg/cm^2 thickness. As per the parameters mentioned in the manuscript, we conducted the dual mode MSI experiments with two different sections for positive and negative mode respectively. The detector gain was set at 1837 V for positive mode and1841 V for negative mode. Mass spectrometry images (MSI) were accumulated at 100 laser shots per pixel and at a 1 kHz repetition rate. Laser operating power was set at 50% with a raster size of 150 μm. The measurement order was set at **Fast** (from top to bottom). The imaging data were normalized by total ion counts (TIC). Sublimation for 9-AA was carried out using 150 mg of 9-AA at 150 °C with a 0.7 Torr vacuum for 800 seconds. Matrix deposition was carried out as mentioned in the manuscript to achieve 0.8 mg/cm^2 thickness. The performance of 9AA-sublimed tissue section had poor results mainly due to the poor interaction between analytes and matrix.[48] (See the reference in **Table 1.** The author investigated in different matrices performance by sublimation method and made the conclusion that 9AA showed poor capability in negative polarity MSI.)

2-5 MALDI-TOF mass spectrometry.

Both MALDI-TOF MS and MALDI-TOF MSI were performed on a Bruker Autoflex Speed mass spectrometer in reflectron geometry at 1 kHz repetition rate. For profiling, mass spectra were obtained by accumulating 1500 laser shots with the “random walk” setting. The detector gain was set at 2016 V for positive mode and 2012 V for negative mode. Mass spectrometry images (MSI) were acquired at 150 μm spatial resolution with 1000 laser shots per pixel, with the laser operating power at 50% and a 1 kHz repetition rate. The laser spot size was set at “medium”, ~80 μm in diameter. The measurement order was set at Fast (from top to bottom). The imaging results shown were normalized by total ion counts (TIC). Image acquisition was carried out using FlexImaging 3.0, and spectral analysis was performed with FlexAnalysis 3.4.

2-6 LC-MS/MS lipid identify

LC-MS/MS was performed on a hybrid LTQ-Orbitrap Elite Mass Spectrometer couple with Vanquish™ Flex Quaternary UHPLC. A heated electrospray ionization (HESI) was used to the ionization source with the following parameters: spray voltage at 4.0 kV in both positive and negative ion mode; capillary temperature at 320 °C; HESI heater temperature at 180 °C; sheath gas flow at 30 and auxiliary gas at 10. Liquid chromatography was performed using a Unitary C18 column (4.6 × 250 mm, 5 μm, ACCHROM, China). A binary gradient was performed with mobile phase A of ACN/water 40:60 (v/v) and mobile phase B of IPA/ACN 90:10 (v/v). Both A and B solvents contain 0.1% ammonium acetate for negative ion mode, and 0.1% FA for positive ion mode. The flow rate was 0.5 mL/min, and a 50-min gradient was established as: 0-

3 min, 20% B; 3-8 min, 20-70% B; 8-30 min, 70-90% B; 30-30.5 min, 90-99% B; 30.5-40 min, 99% B; 40-41 min, 99-20% B; 41-50 min, 20%.

The setting method for lipidomics analysis has been described in the previous report.[57] Three μL mice brain lipid extract was injected for LC-MS/MS analysis. A top-10 data-dependent acquisition (DDA) method was applied. MS/MS spectra were acquired via collision induced dissociation (CID) with an isolation width of 2.0 Th, normalized collision energy of 40.0, activation Q of 0.250, and activation time of 10.00 ms.

2-7 pH control experiment.

COOH-NHMe (IV) and COOH-NH_2 (I) were dissolved in acetonitrile and water (1:1, v/v) at a concentration of 0.1 M. The pH values of matrix solutions are around 4. Trifluoroacetic acid (TFA) and ammonium hydroxide (NH_4OH) were used to adjust the pH value of those matrix solutions. Since COOH-NHMe (IV) and COOH-NH_2 (I) are zwitterionic and weak acid, they work as buffering agents. Mass spectra of lipid signals obtained similar with different pH value (See **Figure S1-S2** in **Appendix B.**). Therefore, it is not essential to adjust the pH value of MALDI sample when COOH-NHMe (IV) and COOH-NH_2 (I) were used as matrix.

2-8 General information and materials.

Unless otherwise mentioned, commercially available reagents were purchased from Sigma-Aldrich and Acros Organics without further purification. Solvent purification was accomplished according to *Purification of Laboratory Chemicals* (Perrin, D. D.; Armarego, W. L. and Perrins, D. R., Pergamon Press: Oxford, 1980). All reactions were carried out under nitrogen and monitored by TLC. Column chromatography used silica gel (230−400 mesh) supplied by Merck.

^{1}H, ^{13}C and ^{19}F NMR spectra were recorded at 22 °C on a Varian Unity 400 spectrometer at 400, 100 MHz and 376 MHz, respectively; the chemical shifts (δ in ppm) were determined with respect to residual non-deuterated solvent as an internal reference (DMSO, δ 2.50 ppm for ^{1}H NMR and δ 39.52 for ^{13}C NMR). The following abbreviations were used to explain the multiplicities: s = singlet, d = doublet, t = triplet, q = quartet, brs = broad singlet, m = multiplet, td = triplet of doublets, dt = doublet of triplets. Low- and high-resolution mass spectra were performed on a JEOL model JMS-700 mass spectrometer using electron ionization (EI) and fast atom bombardment (FAB). X-ray crystallography were conducted using a Bruker D8 VENTURE Single-crystal XRD equipped with Oxford Cryostream 800+. The anthranilic acid (COOH-NH$_2$, **I**) and 2-dimethylaminobenzoic acid (COOH-NMe$_2$, **VIII**) were bought from Sigma-Aldrich company.

2-9 Computation Methodology.

All theoretical calculations were performed using the Gaussian 09 program. The corresponding reaction energy of proton affinity, deprotonation, and proton transfer reaction for the selected compounds in the gas phase were acquired by the density functional theory (**DFT**) method with B3LYP hybrid function. The 6-31+G(d,p) basis set was employed for all atoms.

2-10 Photophysical Measurement.

Steady-state absorption and emission spectra were measured under room temperature with a Hitachi (U-3310) spectrophotometer and an Edinburgh (FS920) fluorimeter, respectively. All wavelength-dependent excitation and emission responses of the fluorimeter have been calibrated. Solvents used for photophysical measurements were spectroscopic grade (Merck Inc.).

Fluorescence lifetime measurement for COOH-NH_2 (**I**), CHO-NH_2 (**II**), COOH-NHMe (**IV**) were performed with an Edinburgh FL 900 time-correlated single photon-counting (TCSPC) system with a hydrogen-filled lamp as the excitation source with 40kHz repetition rate. Fluorescence lifetime measurement for CHO-NHAc (**III**) were performed by TCSPC system (OB-900L Lifetime spectrometer, Edinburgh). The light source was generated from Ti sapphire laser (Tsunami, Spectra Physics, 82 MHz), followed by second harmonic generation to produce excitation beam (380 nm). The polarization of the pump laser was set at the magic angle (54.7˚) with respect to pump beam, in order to eliminate the anisotropy. The temporal resolution is about 20 ps.

Results and Discussion

3-1 Design and Synthesis of Organic Compounds

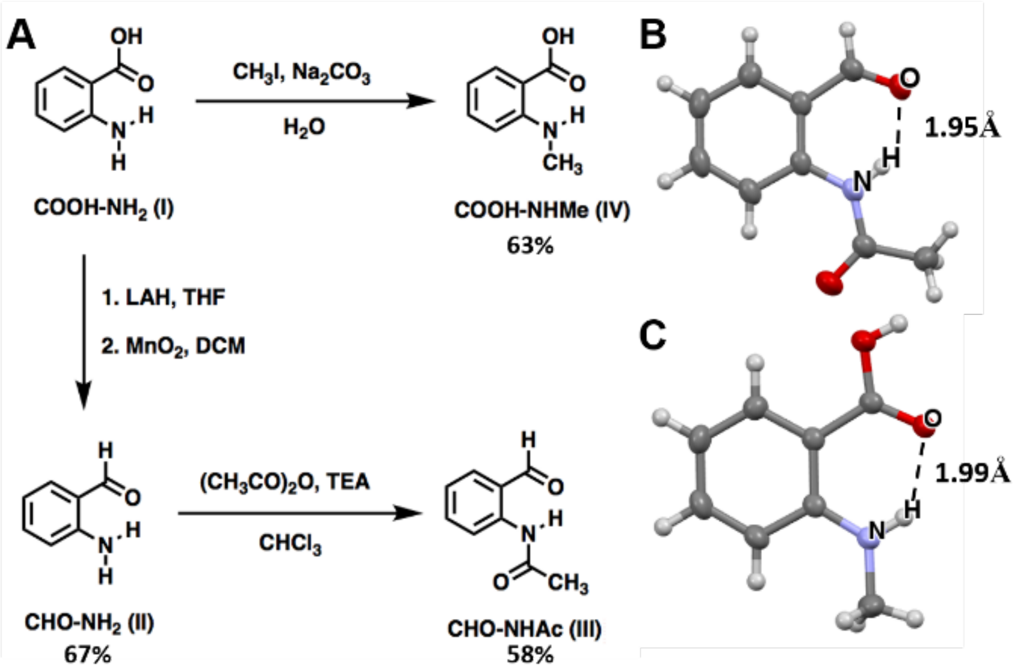

Scheme 1. (A) Synthesis pathway for the anthranilic acid derivatives and X-ray structure of **III** and **IV**. Molecular structure of (B) **III** and (C) **IV** resolved from single crystal X-ray analysis.

The synthetic routes of the title compounds are depicted in **Scheme 1A**. Commercially available COOH-NH$_2$ (**I**) was the initial reactant for the synthesis. COOH-NH$_2$ (**I**) is first reduced by lithium aluminum hydride, followed by an oxidation reaction with MnO$_2$, yielding aldehyde CHO-NH$_2$(**II**). CHO-NH$_2$ (**II**) was then strategically modified into acetamide derivative CHO-NHAc (**III**). Meanwhile, the amino group of COOH-NH$_2$ (**I**) is also functionalized so that one of the amino hydrogen has been replaced with alkyl substituent (-CH$_3$) to obtain derivative COOH-NHMe (**IV**). Notably, the reactions adopted in this study are facile and produces title molecules with good yields (> 50%). Detailed synthetic procedures and characterization of these compounds are provided in the **Appendix A** section. The crystal structures of COOH-NH_2 (**I**) and COOH-NHMe (**IV**) have been resolved in the literature; however, for readers' convenience the prerequisite structural information of **I** and **IV** was shown in this study, as well.[58,59] **Scheme 1B** and **1C** depict the X-ray structure of CHO-NHAc (**III**) and COOH-NHMe (**IV**) (see **Figure S3** in **Appendix B-2.** for COOH-NH_2, **I**), respectively, both of which are in a planar configuration. Although the N-H hydrogen atom is artificially added in solving the X-ray structure, the N-H---O=C intramolecular H-bond formation can be supported by the ^{1}H NMR measurement, in which COOH-NH_2 (**I**) in DMSO-d_6 and **II-IV** in benzene-d_6 show downfield shift of the N-H proton in the range of 5.78-11.03 ppm (see **Figures S4-7** in **Appendix B-2.**).

3-2 Dual-Polarity Characteristics and Physical Properties Measurement

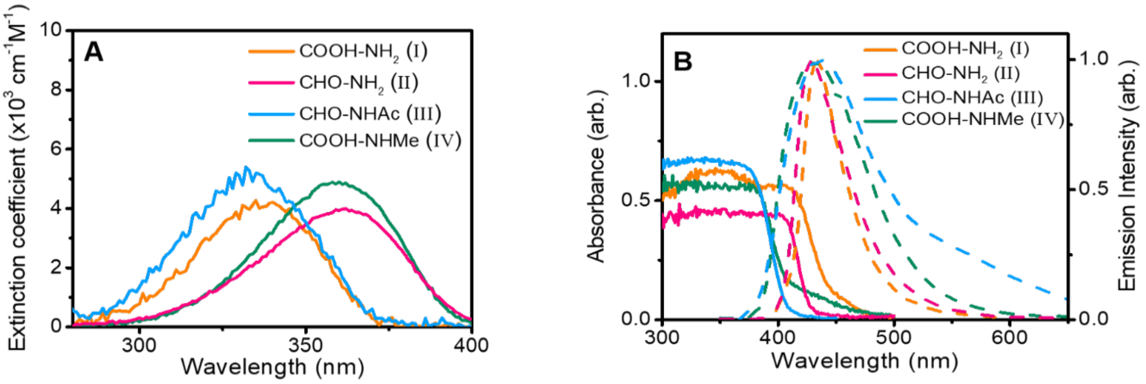

Figure 1. (A) Absorption spectra of matrix **I-IV** measured in dichloromethane (DCM). (B) Absorption (solid line) and emission spectra (dash line) of matrix **I-IV** measured in solid state. λ_{ex} = 340 nm for COOH-NH$_2$ (**I**), CHO-NH$_2$ (**II**), COOH-NHMe (**IV**) and λ_{ex} = 320 nm for CHO-NHAc (**III**).

For COOH-NH$_2$ (**I**) and COOH-NHMe (**IV**), the carboxylic and amino groups that serve as proton donor and proton acceptor, respectively, are expected to effectively produce positive and negative ions. CHO-NH$_2$(**II**) and CHO-NHAc (**III**), lacking the potent proton donor site, were compared with COOH-NH$_2$ (**I**) and COOH-NHMe (**IV**) in terms of their dual polarity properties. These compounds were rationally designed for the carboxylic/carbonyl group and amino derivatives to be in the ortho position in order to form an intramolecular hydrogen bond (H-bond) between the carboxylic/carbonyl and amino hydrogen. This strategy has two major characteristics. Firstly, the intramolecular H-bond induced π-conjugation, which decreases the HOMO-LUMO energy gap to reach the absorption maximum suitable for commercial laser excitation (third harmonic Nd:YAG laser, 355 nm).[11,60] In addition, the formation of intramolecular H-bond is expected to reduce the intermolecular H-bond interaction and hence to increase the efficiency of the desorption.

Figure 1A shows the absorption spectra of compounds **I-IV** in dichloromethane (DCM), which all exhibit the lowest lying absorption bands in the range of 300 to 400 nm. Nevertheless, appreciable absorption extinction of > 2000 cm^{-1} M^{-1} was observed for all **I-IV** at 355 nm of the third harmonic Nd:YAG laser, the most popular commercial excitation source for MALDI.[5061] Among the title compounds, COOH-NHMe (**IV**) exhibits the highest extinction coefficient at 355 nm. It is also worth noting that the formation of intramolecular H-bond is critical to enhance the charge transfer character and hence the red shift of the absorption. For example, anchoring carboxyl and amino groups in meta- and para- positions with no intramolecular H-bond formation causes the blue shift of the absorption with peak wavelength being far blue shifted from 355 nm (See **Table 3** for the detailed information of the references).[62–64] In fact, aside from I-IV, other derivatives have also been synthesized (see compounds **V-IX** in **Appendix A.**); however, those compounds show either unsuitable absorption band (**V-VIII**) or low melting points (**IX**) and hence were not investigated further in this study. **Figure 1B** shows the absorption and emission spectra of matrix **I-IV** measured in solid state. The different absorption pattern of matrix **I-IV** between solution and solid phase suggests slightly intermolecular interaction existing in solid state.

3-3 Photophysical Properties and Explanation

The computational approach (TD-DFT, B3LYP/6-31+g(d,p)) depicted in **Table S1** in **Appendix B-3**, clearly reveals that HOMO and LUMO have contribution, in part, from -NHR and carbonyl (CHO or COOH), respectively and the transition possess partial charge transfer character. Therefore, with the same -NH_2 functional group, the stronger electron withdrawing CHO group (cf. COOH) decreases LUMO energy, rationalizing the lowest lying absorption peak wavelength for CHO-NH_2 (**II**) being red shifted relative to that of COOH-NH_2 (**I**). Similarly, with the same -CHO group, the -NHAc donating group in CHO- NHAc (**III**) is weaker than that of –NH_2 in CHO-NH_2 (**II**). As a. result, the HOMO energy of CHO-NHAc (**III**) decreases, explaining its blue shifted absorption compared with CHO-NH_2 (**II**). Also, the stronger electron donating strength for –NHMe lifts the HOMO energy, making COOH-NHMe (**IV**) much more red shifted than that of COOH-NH_2 (**I**). The trend of the absorption gap is thus in the order of CHO-NHAc (**III**) > COOH-NH_2 (**I**) > COOH-NHMe (**IV**) > CHO-NH_2 (**II**).

Table 2. Time-resolved fluorescence measurements and quantum yield (Q.Y.) compound I-IV in solid phase.

Compounds	**Q.Y. (%)**	**Monitor wavelength (nm)**	**Lifetime (ns)**
COOH-NH_2 (**I**)	15.3	480	14.6
CHO-NH_2 (**II**)	5.3	480	1.25
CHO-NHAc (**III**)	2.9	440	0.112, 1.08
COOH-NHMe (**IV**)	43.1	480	8.95

[a] λ_{ex} = 340 nm for COOH-NH_2, CHO-NH_2, COOH-NHMe and λ_{ex} = 320 nm for CHO-NHAc.

[b] λ_{ex} = 340 nm for COOH-NH_2, CHO-NH_2, COOH-NHMe and λ_{ex} = 380 nm for CHO-NHAc.

COOH-NH_2 (**I**) and COOH-NHMe (**IV**) show strong fluorescence with quantum yield (QY) of 15.3% and 43.1%, respectively, in solid state, and the corresponding lifetime was determined to be as long as 14.6 ns (COOH-NH_2, **I**) and 8.9 ns (COOH-NHMe, **IV**) (**Table 2**). Decent fluorescence yield was measured for CHO-NH_2 (**II**) (QY = 5.3%) and CHO-NHAc (**III**) (QY = 2.9%); their fluorescence lifetime in solid matrix was measured to be 1.3 and 1.1 ns, respectively. Protonated ion and deprotonated ion are generated by proton transfer reaction and ion-ion recombination among matrix (M) and analyte (A) compounds (e.g. $M+M \rightleftarrows [M+H]^{+}+[M-H]^{-}$, $M+A \rightleftarrows [M+H]^{+}+[A-H]^{-}$ and $M+A \rightleftarrows [M-H]^{-}+ [A+H]^{+}$)[17,19] ; however, these reactions may not reach equilibrium in the gas phase. In contrast, ion-molecule reaction (e.g. $[M+H]^{+}+A \rightleftarrows M+ [A+H]^{+}$ and $[M-H]^{-}+A \rightleftarrows M +[A-H]^{-}$) may reach equilibrium, which has high correlation to intensity of analyte ion.[19,65,66]

As shown in **Table 4**, on the one hand, the PA exhibits a trend with COOH-NHMe (**IV**) > COOH-NH_2 (**I**) > CHO-NH_2 (**II**) > CHO-NHAc (**III**), which can be rationalized by the chemical modification on the -NHR. The substitution with alkyl group increased basicity of the lone pair electron on the nitrogen, and hence provides greater driving force for deprotonation. On the other hand, the relatively lower DE of COOH-NH_2 (**I**) and COOH-NHMe (**IV**) (cf. CHO-NH_2, **II** and CHO-NHAc, **III**) suggested that they were more readily to be protonated with carboxylic group, rendering a more positive ion signal of the analytes. Moreover, the heat of proton transfer reaction between matrix-analyte and matrix-matrix was also deduced by DE – PA (**Table 4**). As a result, the heat of reaction of CHO-NH_2 (**II**) and CHO-NHAc (**III**) is more endothermic than that of COOH-NHMe (**IV**) and COOH-NH_2 (**I**) during MALDI process, suggesting an unfavorable proton transfer reaction. The estimation of the ion yield can be calculated from the following equation.[67]

$$\text{Ion yield} = e^{-\frac{\Delta H}{2kT}} \qquad (1)$$

According to eq. (1), as the heat of reaction increases, the ion yield should decrease.

Table 3. Absorption peak wavelength of the reported aminobenzoic acid and aminobenzaldehyde derivatives.

aminobenzoic acid derivatives		**aminobenzaldehyde derivatives**	
compound	**λ_{abs} (nm) / solvent**[a]	**compound**	**λ_{abs} (nm) / solvent**[a]
p-aminobenzoic acid	290 / methanol[63]	*p*-aminobenzaldehyde	296 / cyclohexane[68]
m-aminobenzoic acid	306 / ethanol[69]	*m*-aminobenzaldehyde	327 / cyclohexane[68]
N-methyl-*p*-aminobenzoic acid	299 / ethanol[70]		

[a] Solvent used for the absorption measurements.

Table 4. Heat (kcal/mol) of protonation, deprotonation, and proton transfer reaction for the compounds in the gas phase (Calculated results are from DFT). Considerations of absorption characteristics at 355 nm.

Matrix (M)	**Proton affinity** **$M+H^+ \rightarrow [M+H]^+$**	**Deprotonation energy** **$M \rightarrow [M-H]^- + H^+$**	**Proton transfer reaction** **$M+M \rightarrow [M+H]^+ + [M-H]^-$**	**Extinction coefficient**[b] **($cm^{-1}M^{-1}$)**
COOH-NHMe (**IV**)	219	333	114	4800
CHO-NH_2 (**II**)	205	362	157	3800
CHO-NHAc (**III**)	197	349	152	2600
COOH-NH_2 (**I**)	207	336	129	2400
CHO-$NHCOCF_3$ (**VII**)	189	335	146	390
COOH-$NHCOCF_3$ (**VI**)	190	317	127	60
COOH-NMe_2 (**IIIV**)	224	339	115	3
CHCA	197[a]	316[a]	119[a]	13000
2,5-DHB	202, 200[a]	323, 325[a]	121, 120[a]	2200

2,5-DHAP	209[a]	338[a]	129[a]	1100
SA	212	328	116	2500
9-AA	204	340	136	2100
1,5-DAN	216	358	142	1100

---

[a] Calculated results are from ab initio quantum chemistry calculations.

[b] All compounds were dissolved in DCM for UV-visible measurement

3-4 Standards Analysis and Observation with Physical Explanations

We then used **I-IV** as the matrix and PS(14:0/14:0) as the analyte to demonstrate the 355-nm laser desorption property. COOH-NHMe (IV) clearly shows the highest ion signal (see **Figure 2**) due to its strongest absorption at 355 nm among **I-IV** (**Table 4.**), suggesting that the ion efficiency is highly related to the extinction coefficient. Moreover, the characteristic signals for PC(14:0/14:0), PS(14:0/14:0) and PE(14:0/14:0) were most strongly detected by COOH-NH2 (**I**) and COOH-NHMe (**IV**) (**Figure 3**). In fact, only COOH-NH$_2$ (**I**) and COOH-NHMe (**IV**) yielded signals for PS(14:0/14:0), while no signal could be observed when applying CHO-NH$_2$(**II**) and CHO-NHAc (**III**) as the matrix (see **Figure 2**).

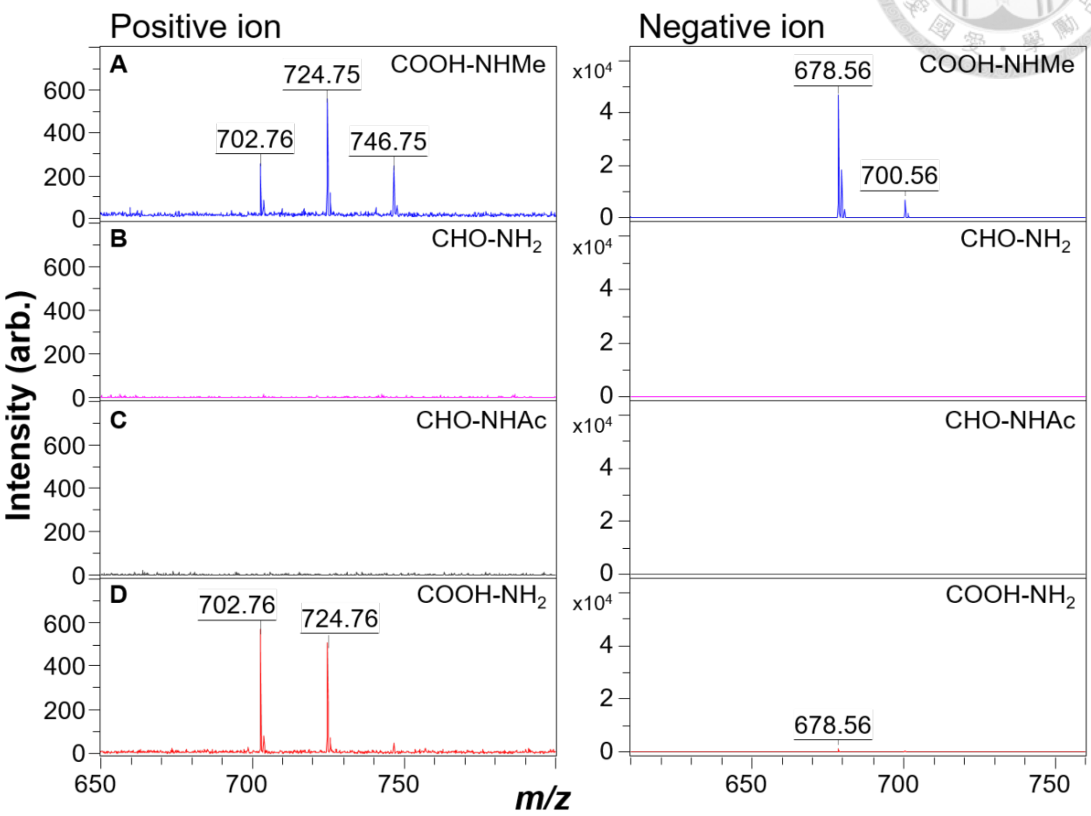

Figure 2. Mass spectra of PS(14:0/14:0) obtained from samples prepared with different matrices (A) COOH-NHMe (**IV**), (B) CHO-NH$_2$ (**II**), (C) CHO-NHAc (**III**) and (D) COOH-NH$_2$ (**I**) in positive and negative ion mode, respectively. Left column represents the positive ion detection, while the right column represents the negative ion detection.

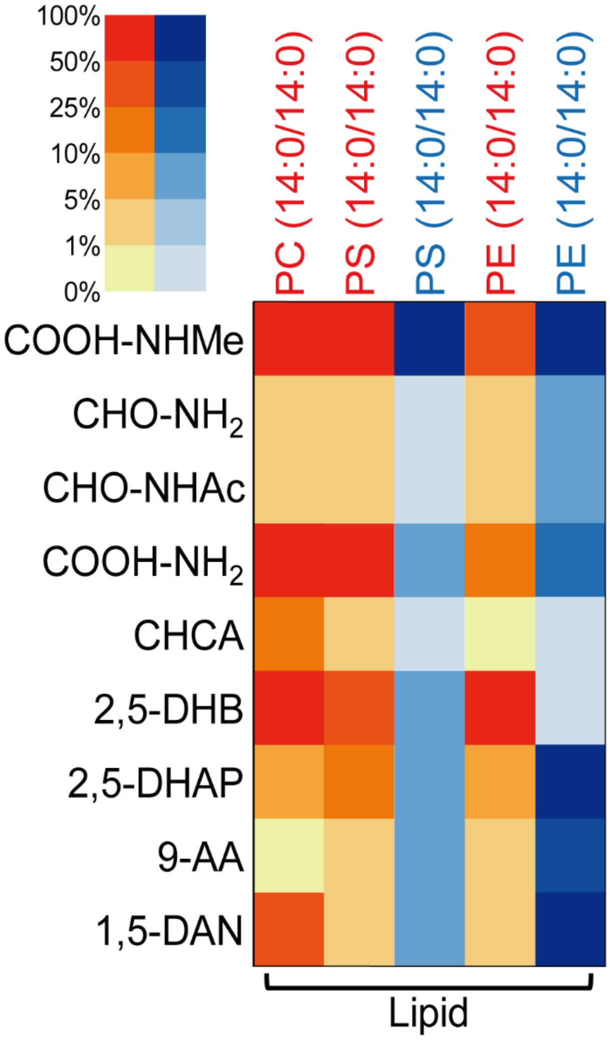

Figure 3. Signal comparison of lipid standards, PC(14:0/14:0), PS(14:0/14:0) and PE(14:0/14:0), using the synthesized compounds and commercially available matrices. The laser intensities used for different matrices were optimized to achieve best signals. Analytes in red were acquired in positive ion mode, while those in blue were acquired in negative ion mode.

These experimental results do not align with the extinction coefficient of the matrix: COOH-NHMe (**IV**) > CHO-NH_2 (**II**) > CHO-NHAc (**III**) > COOH-NH_2 (**I**) (see **Table 4**). This is not surprising because the extinction coefficient merely accounts for one of multiple factors for analyte desorption/ionization. Other factors, such as the difference in fluorescence lifetime among **I-IV**, also need be considered. Since the applied 355-nm laser has a pulse duration time of ~5 ns, matrices with longer fluorescence lifetime such as COOH-NH_2 (**I**) and COOH-NHMe (**IV**) (see **Table 2**) are expected to have a higher chance for multiphoton events. More importantly, matrix interaction with analyte is important when it comes to the MALDI process. Commonly, positive ions are observed as protonated, sodiated or potassiated ions ($[M+H]^+$, $[M+Na]^+$ and $[M+K]^+$), where negative ions are observed as deprotonated ions ($[M-H]^-$).[71,72,73,74,60,19,17,65] Therefore, in order to quantify the feasibility of the synthesized matrix, theoretical calculation based on density function theory (DFT) was conducted to acquire the corresponding proton affinity (PA) and deprotonation energy (DE), whose values can provide insights into the tendency towards producing $[M+H]^+$ and $[M-H]^-$, respectively. Among the synthesized matrices, COOH-NHMe (**IV**) showed relatively high PA and low DE (**Table 4.**),[67] and thus is expected to be a suitable matrix in both positive and negative modes. Importantly, the values of PA and DE of COOH-NHMe (**IV**) are comparable to those of commercial matrices that are solely suitable in positive or negative mode (see **Table 4.**), showing its high potential in practical matrix applications.

3-5 Investigation of Synthesized Compounds

To gain more insight into the efficacy of our synthesized compounds, we chose some of the most representative commercially available matrices to compare their performances. **Figure 3** shows the relative signal intensities of PC(14:0/14:0), PS(14:0/14:0) and PE(14:0/14:0) from the typical commercially available matrices. 2,5-DHB and CHCA provide lower ion abundance of negative ion relative to positive ion, and are commonly used in positive ion detection.[75] On the other hand, 9-AA and 1,5-DAN are suitable for negative ion detection. {Citation}[76,77] In comparison, compounds **I-IV**, having a simple aromatic ring endowed with acid-base bifunctionality are great candidates of MALDI matrices for dual polarity detection. **Figure 4.** compares the signal intensities of lipid and protein standards detectable with the COOH-NH_2 (**I**) and COOH-NHMe (**IV**) (commercially available) and commonly used matrices. Among them, lipids analyzed using COOH-NHMe (**IV**) as the matrix (**Figure 4**.) exhibited the highest ion signal compared to other compounds, even though the extinction coefficients of all studied matrices were within the same order of magnitude. The most comparative commercially available matrix was 1,5-DAN for lipid detection, though its protein signals were less impressive (**Figure 4.** and **Figure 5.**). Additional experiments were performed to analyze proteins extracted from mouse brains in both positive and negative ion mode, with results from triplicate analyses shown in **Figure S8-S10.**

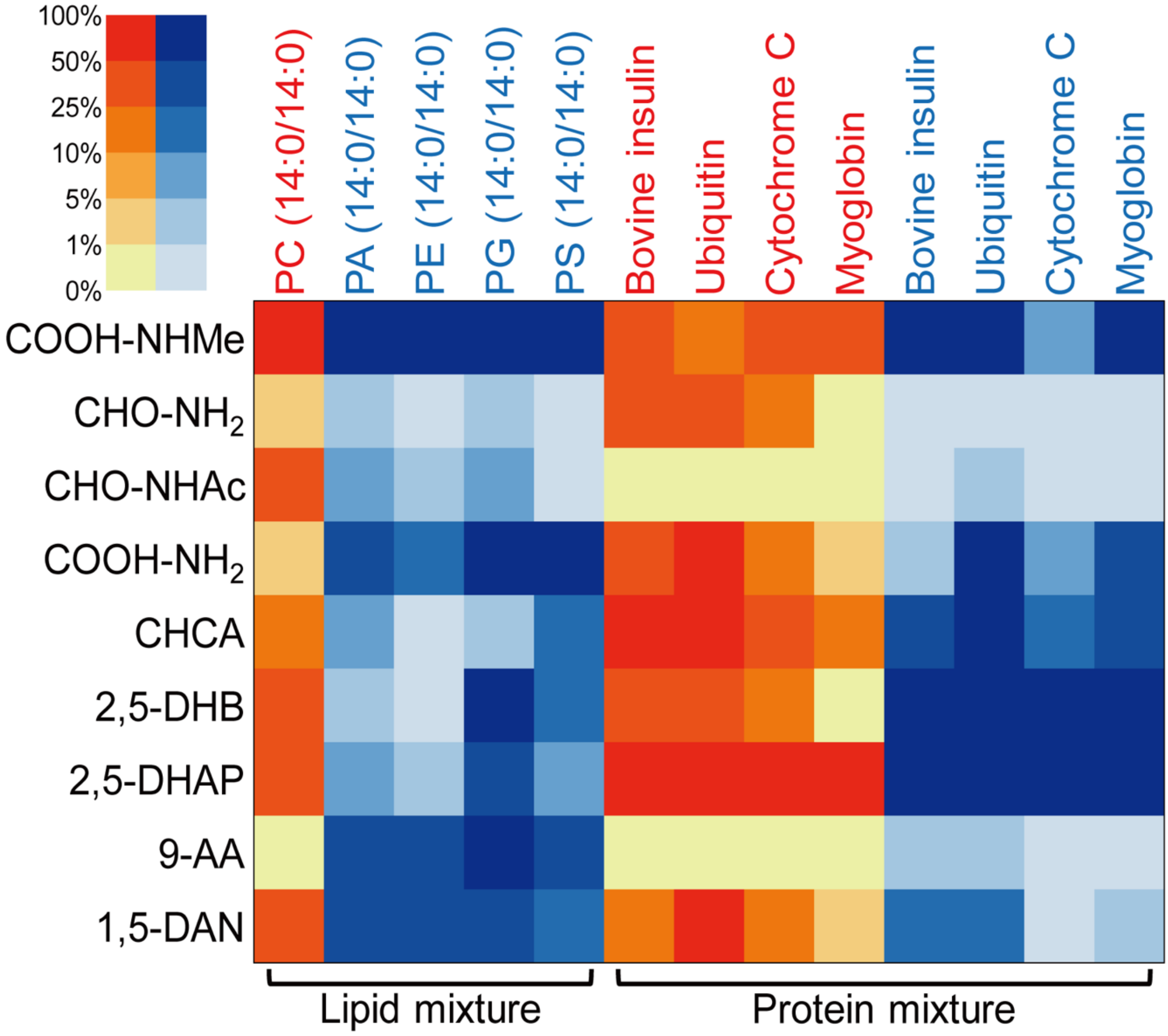

Figure 4. Comparison of the relative signal intensities of lipid species and proteins species when using the synthesized COOH-NH$_2$ (**I**), COOH-NHMe (**IV**) or some of the most representative commercially available matrices. The laser intensities used for different matrices were optimized to achieve the most optimal signal. The analytes written in red indicates signals were obtained in positive ion mode and blue in negative ion mode. COOH-NHMe (**IV**) had superior performance in lipid analysis and was also capable of analyzing proteins in both positive and negative mode.

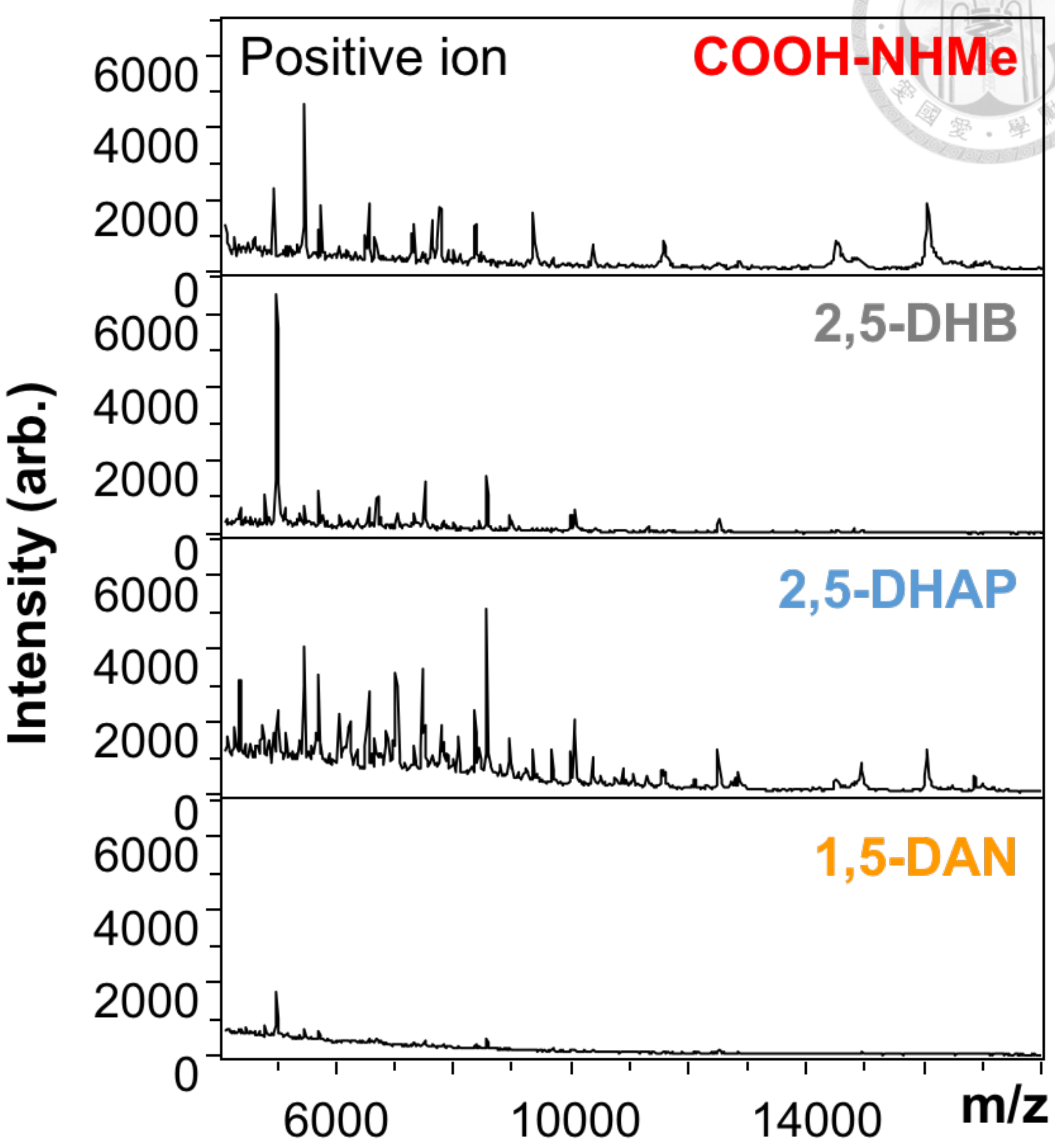

Figure 5. Mass spectra of the brain protein extracts obtained from samples prepared by COOH-NHMe (**IV**) and commonly used commercial matrices for protein analysis, 2,5-DHB, 2,5-DHAP and 1,5-DAN in positive ion mode.

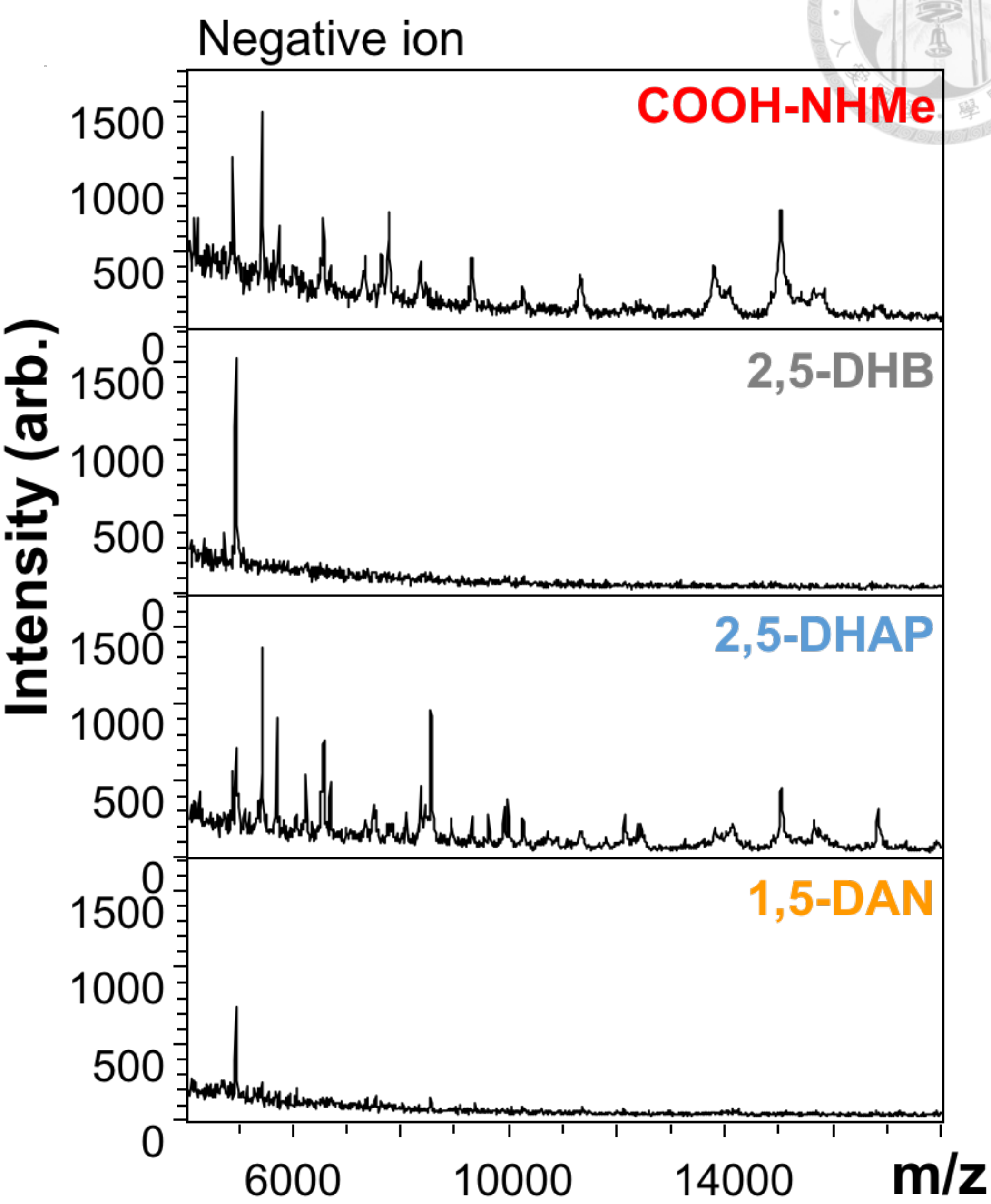

Figure 6. Mass spectra of the brain protein extract obtained from samples prepared by COOH-NHMe and commonly used commercial matrices for protein analysis, 2,5-DHB, 2,5-DHAP and 1,5-DAN in negative ion mode.

As shown in **Figure 5.** and **Figure 6**, a great number of protein species were observed with COOH-NHMe (**IV**) and 2,5-DHAP relative to 2,5-DHB. Moreover, relatively few protein species can be observed from 1,5-DAN, implying that this previously-reported dual polarity matrix may have limited mass coverage for biomolecules. MSI of protein distribution in Mouse brains section was performed by using COOH-NHMe (**IV**) (**Figure 7.**).

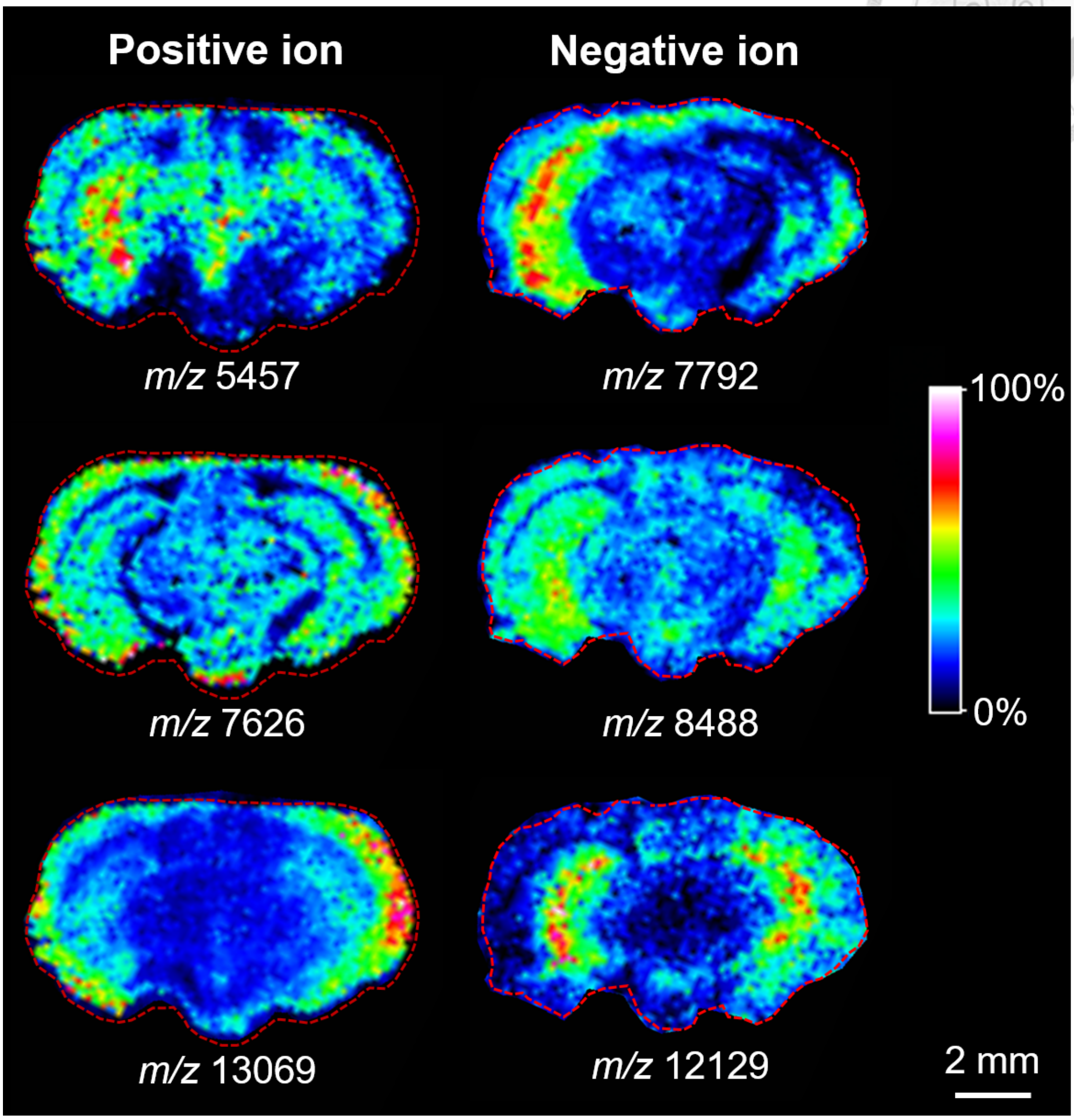

Figure 7. MSI of coronal mice brain sections sublimated with COOH-NHMe (**IV**) in positive and negative ion mode, demonstrating the capability of COOH-NHMe (**IV**) in mapping the protein distribution. MSI were accumulated 1000 laser shots per pixel and were acquired with a 1 kHz repetition rate. Laser operating power was set at 10% with a raster size of 150 μm and the laser focus was set to "**small**".

3-6 The Comparison with Commercial MALDI Matrices on Biological Samples in Positive and Negative Ion mode

We further demonstrated the superiority of COOH-NHMe (**IV**) in terms of the molecular coverage and dual-polarity compatibility in the MALDI-TOF measurement on mouse brains lipid extract. The comparison between COOH-NHMe (**IV**) and two of the most commonly used matrices for lipid analysis, 2,5-DHB (standard matrix for positive ion mode detection) and 9-AA (standard matrix for negative ion mode detection), is shown in **Figure 8.** Remarkably, COOH-NHMe (**IV**) showed a rich lipid profile in both positive and negative ion mode, whereas 2,5-DHB and 9-AA showed only limited coverage due to their single-polarity character.[78] Moreover, the comparison between COOH-NHMe (**IV**) and early reported ma-trices for dual polarity has been made. As a result, the performance of COOH-NHMe (**IV**) is as good as 2,6-DHAP and 1,5-DAN in both positive and negative ion mode (**Figure 9**). Note that due to the limited vacuum stability, 2,6-DHAP is not commonly applied for vacuum MALDI MSI, but instead used for atmospheric pressure (AP)-MALDI.[79,80]

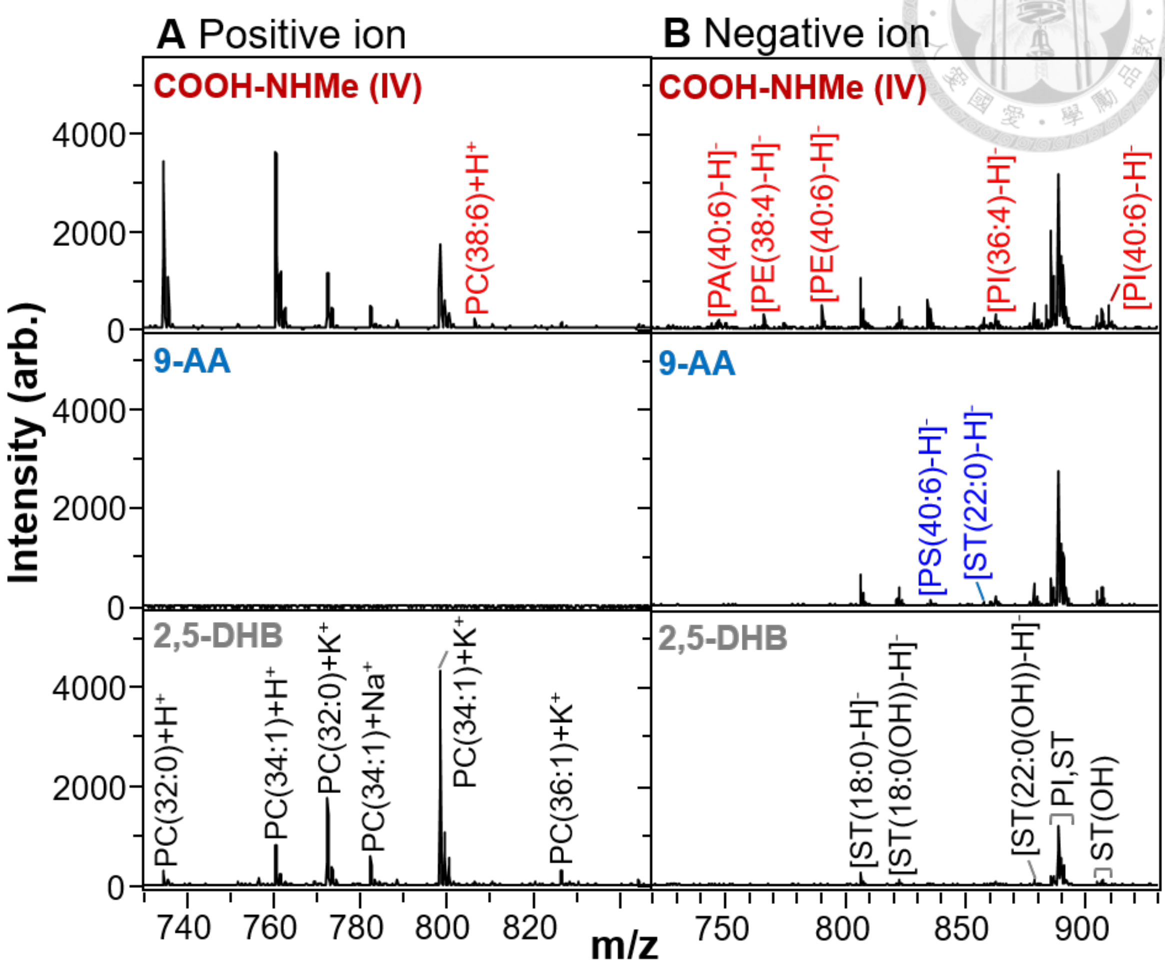

Figure 8. Mass spectra of the brain lipid extract obtained from samples prepared by COOH-NHMe (**IV**) and commonly used commercial matrices for lipid analysis, 9-AA and 2,5-DHB, in (A) positive and (B) negative ion mode respectively. COOH-NHMe (**IV**) outperformed the widely used commercial matrices for lipid analysis in both positive and negative mode. The ions marked in red indicate that the ions observed only using COOH-NHMe (**IV**) as matrix. The ions observed using 9-AA as matrix but not 2,5-DHB were marked in blue.

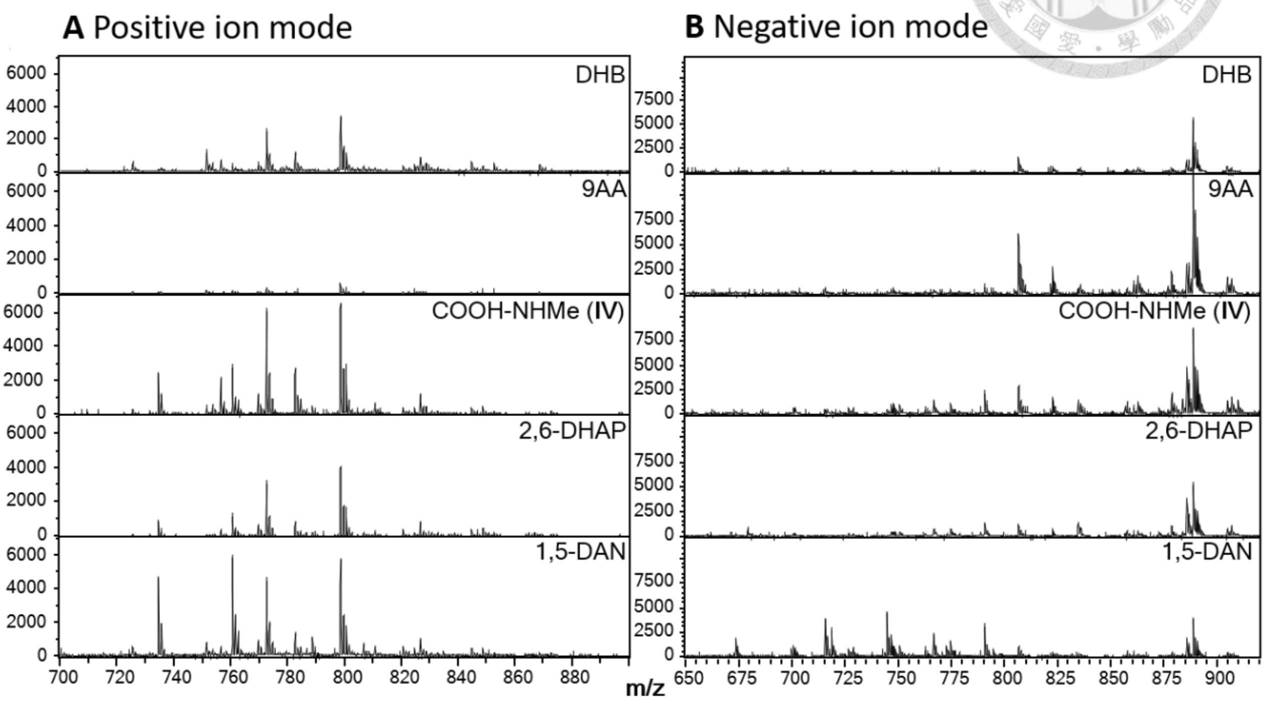

Figure 9. Mass spectra of the brain lipid extract obtained from samples prepared by 2,5-DHB, 9-AA, COOH-NHMe (**IV**), 2,6-DHAP and 1,5-DAN, in (A) positive and (B) negative ion mode respectively.

The positive (deprotonation of the matrix) and negative (protonated of the matrix) can be explained by their proton affinity and deprotonation energy (**Table 4.**). The deprotonation energy of 2,5-DHB is relatively low, so the proton transfers easily from matrix to analyte, producing protonated analyte ion. On the contrary, the proton affinity of 9-AA is relatively high and the proton easily transfers from analyte to matrix, yielding deprotonated analyte ions. **Figure 8A.** shows the signals of the positive ions, $[M+H]^+$, $[M+Na]^+$ and $[M+K]^+$. In **Figure 8B**, signals of negative ion represent [M-H]- correspond to phosphatidylethanolamines (PE), phosphatidic acids (PA), phosphatidylserines (PS), phosphatidylinositols (PI), sulfatides (ST) and hydroxylated sulfatides (ST(OH)). LC-MS/MS was conducted on the sample mouse brain extract to and the species detected were confirmed by LipidSearch™ (Thermo Fisher Scientific). Details of the assignments of mass spectra are listed in **Table S2** and **Table S3.** (See Table in **Appendix B3.**) The results obtained by using COOH-NHMe (**IV**) as a matrix revealed more lipid species than using 2,5-DHB and 9-AA. For example, $[PE(40:6)-H]^-$, $[PI(36:4)-H]^-$ and $[PI(40:6)-H]^-$ were observed when COOH-NHMe (**IV**) was used as the matrix but missing when using 2,5-DHB. Also, the spatial distribution of the three species only detectable by COOH-NHMe, spatial distributions of $[PE(40:6)-H]^-$, $[PI(36:4)-H]^-$ and $[PI(40:6)-H]^-$ are shown in **Figure 10**. Distinct distributions of lipids were thus obtained from COOH-NHMe (**IV**).

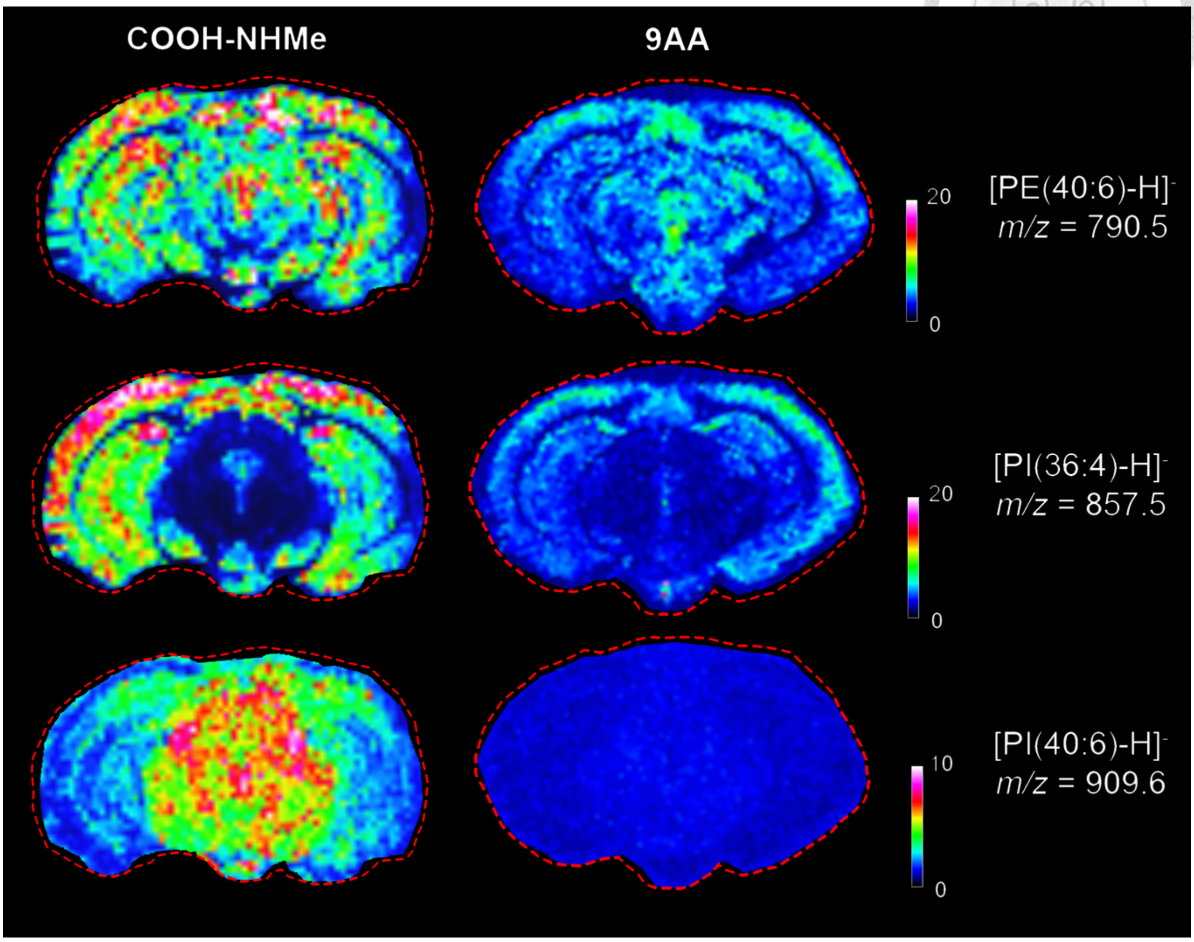

Figure 10. MSI of mouse brains sections sublimated with COOH-NHMe (**IV**) and 9AA in negative ion mode. The color scale for each ion species were under the same intensity threshold. The lipid species scan revealed the deprotonated ion at m/z 790.5, 857.5 and 909.6, corresponding to [PE(40:6)-H]$^-$, [PI(36:4)-H]$^-$ and [PI(40:6)-H]$^-$, respectively.

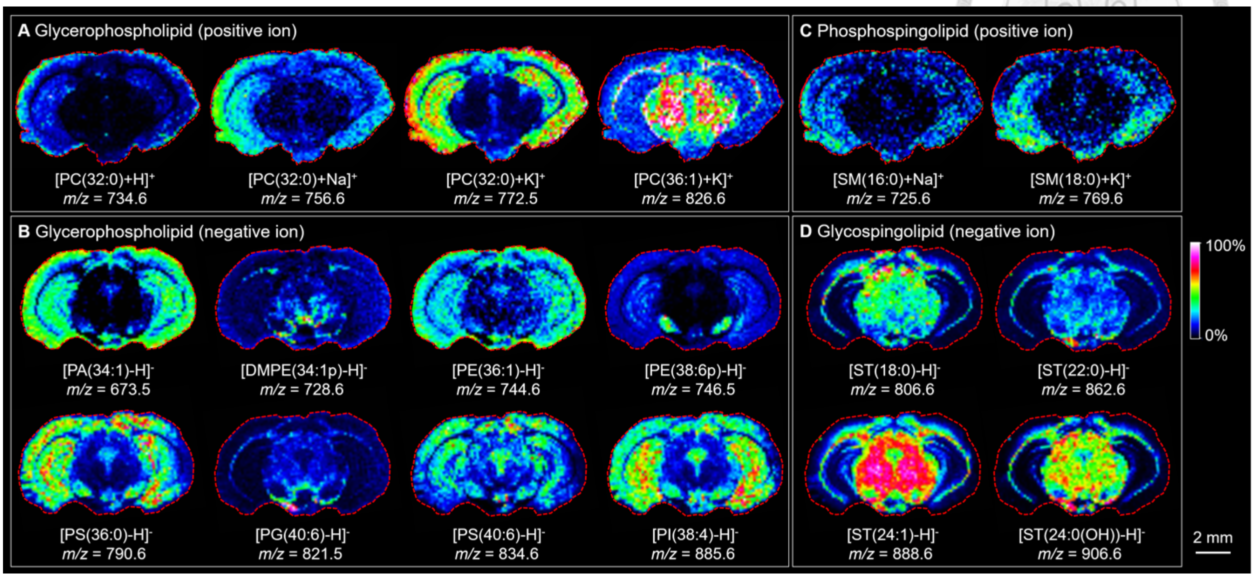

Figure 11. MSI of mouse brains sections sublimated with COOH-NHMe (**IV**) and 9AA in negative ion mode. The color scale for each ion species were under the same intensity threshold. The lipid species scan revealed the deprotonated ion at m/z 790.5, 857.5 and 909.6, corresponding to [PE(40:6)-H]$^-$, [PI(36:4)-H]$^-$ and [PI(40:6)-H]$^-$, respectively.

3-7 MALDI-MSI with Potential MALDI Matrix - COOH-NHMe (IV)

To demonstrate the capability of COOH-NHMe (**IV**) in mapping the lipid distribution, we applied it as the matrix for MALDI-TOF MSI on a coronal mouse brain section (**Figure 11** and **Figure S11** in **Appendix B-2.**). In the positive ion mode, we observed PC and sphingomyelin (SM) species, in which PC (36:1) was largely observed in the white matter of the brain, while PC (32:0) was revealed in the gray matter. These results were in agreement with the previous report using the other universal matrices.[81–83] In the negative ion mode, we observed several glycer-ophospholipids, e.g. PA (34:1), PE (36:1), PS (36:0), PI (38:4) in the gray matter and the dimethyl-phosphatidylethanolamine DMPE (34:1p), PG (40:6) in the white matter. ST was also resolved in the negative ion mode. As such, similar to the analysis of the brain lipid extract, untargeted molecular imaging of lipids can be successfully obtained by MALDI-TOF MSI with both positive ions and negative ions simultaneously within one experiment. Also, this matrix is potentially capable of performing high spatial resolution MSI, although most of our tests, due to the limit of facility, are limited at 80 μm within 2 hours under vacuum. Given that sublimation produces sub-nanometer crystals, with a more advanced system such as the Bruker rapifleX equipped with a 10 kHz laser, it would be possible to accomplish 5 μm MSI on an entire mouse brain section within 2 hours.

Conclusions

In this work, we synthesized a series of new anthranilic acid derivatives **I-IV**, of which COOH-NH_2 (**I**) and COOH-NHMe (**IV**) are endowed with acid/base bifunctional properties and have demonstrated their potential for dual polarity detection in MALDI-TOF mass spectrometry. The dual polarity character can be rationalized by its proton affinity and deprotonation energy. Of them, COOH-NHMe (**IV**) exhibits an outstanding efficiency in generating ions of a wide variety of biomolecules, including lipids and proteins, upon laser excitation. High quality molecular imaging of lipids in mouse brains sections was readily obtained by a commercial MALDI-TOF mass spectrometer using our newly designed organic matrix. As many new candidate compounds have been recently proposed as suitable dual polarity matrices, [73,84–86] we aim to compare our proposed matrix with these compounds in the near future. We believe that via a more thorough and systematic investigation that integrates the photophysical and chemical insights, a universal matrix for MALDI mass spectrometry shall soon be realized.

*This thesis is a revised version of the material as it appears in the published article of *Analytical Chemistry*, **2020**, 92, pp. 7139-7145. https://doi.org/10.1021/acs.analchem.0c00570. by Penghsuan Huang, Chun-Ying Huang, Ta-Chun Lin, Li-En Lin, Ethan Yang, Chuping Lee, Cheng-Chih Hsu, and Pi-Tai Chou. The thesis author was the primary author and investigator.

Reference

(1) Kempa, E. E.; Hollywood, K. A.; Smith, C. A.; Barran, P. E. High Throughput Screening of Complex Biological Samples with Mass Spectrometry – from Bulk Measurements to Single Cell Analysis. *Analyst* 2019, *144* (3), 872–891. https://doi.org/10.1039/C8AN01448E.

(2) Rohman, M.; Wingfield, J. High-Throughput Screening Using Mass Spectrometry within Drug Discovery. *Methods Mol. Biol. Clifton NJ* 2016, *1439*, 47–63. https://doi.org/10.1007/978-1-4939-3673-1_3.

(3) Kuo, T.-H.; Huang, H.-C.; Hsu, C.-C. Mass Spectrometry Imaging Guided Molecular Networking to Expedite Discovery and Structural Analysis of Agarwood Natural Products. *Anal. Chim. Acta* 2019, *1080*, 95–103. https://doi.org/10.1016/j.aca.2019.05.070.

(4) Franck, J.; Arafah, K.; Elayed, M.; Bonnel, D.; Vergara, D.; Jacquet, A.; Vinatier, D.; Wisztorski, M.; Day, R.; Fournier, I.; Salzet, M. MALDI Imaging Mass Spectrometry: STATE OF THE ART TECHNOLOGY IN CLINICAL PROTEOMICS. *Mol. Cell. Proteomics* 2009, *8* (9), 2023–2033. https://doi.org/10.1074/mcp.R800016-MCP200.

(5) Karlsson, O.; Hanrieder, J. Imaging Mass Spectrometry in Drug Development and Toxicology. *Arch. Toxicol.* 2017, *91* (6), 2283–2294. https://doi.org/10.1007/s00204-016-1905-6.

(6) Meistermann, H.; Norris, J. L.; Aerni, H.-R.; Cornett, D. S.; Friedlein, A.; Erskine, A. R.; Augustin, A.; De Vera Mudry, M. C.; Ruepp, S.; Suter, L.; Langen, H.; Caprioli, R.

M.; Ducret, A. Biomarker Discovery by Imaging Mass Spectrometry: Transthyretin Is a Biomarker for Gentamicin-Induced Nephrotoxicity in Rat. *Mol. Cell. Proteomics MCP* 2006, *5* (10), 1876–1886. https://doi.org/10.1074/mcp.M500399-MCP200.

(7) Schwamborn, K. Imaging Mass Spectrometry in Biomarker Discovery and Validation. *J. Proteomics* 2012, *75* (16), 4990–4998. https://doi.org/10.1016/j.jprot.2012.06.015.

(8) Scott, A. J.; Jones, J. W.; Orschell, C. M.; MacVittie, T. J.; Kane, M. A.; Ernst, R. K. Mass Spectrometry Imaging Enriches Biomarker Discovery Approaches with Candidate Mapping: *Health Phys.* 2014, *106* (1), 120–128. https://doi.org/10.1097/HP.0b013e3182a4ec2f.

(9) Nielsen, M. M. B.; Lambertsen, K. L.; Clausen, B. H.; Meyer, M.; Bhandari, D. R.; Larsen, S. T.; Poulsen, S. S.; Spengler, B.; Janfelt, C.; Hansen, H. S. Mass Spectrometry Imaging of Biomarker Lipids for Phagocytosis and Signalling during Focal Cerebral Ischaemia. *Sci. Rep.* 2016, *6* (1), 1–14. https://doi.org/10.1038/srep39571.

(10) Kim, S.-W.; Roh, J.; Park, C.-S. Immunohistochemistry for Pathologists: Protocols, Pitfalls, and Tips. *J. Pathol. Transl. Med.* 2016, *50* (6), 411–418. https://doi.org/10.4132/jptm.2016.08.08.

(11) Karas, Michael.; Bachmann, Doris.; Hillenkamp, Franz. Influence of the Wavelength in High-Irradiance Ultraviolet Laser Desorption Mass Spectrometry of Organic Molecules. *Anal. Chem.* 1985, *57* (14), 2935–2939. https://doi.org/10.1021/ac00291a042.

(12) Tanaka, K.; Waki, H.; Ido, Y.; Akita, S.; Yoshida, Y.; Yoshida, T.; Matsuo, T. Protein and Polymer Analyses up to m/z 100 000 by Laser Ionization Time-of-Flight Mass Spectrometry. *Rapid Commun. Mass Spectrom.* 1988, *2* (8), 151–153. https://doi.org/10.1002/rcm.1290020802.

(13) Shevchenko, A.; Loboda, A.; Shevchenko, A.; Ens, W.; Standing, K. G. MALDI Quadrupole Time-of-Flight Mass Spectrometry: A Powerful Tool for Proteomic Research. *Anal. Chem.* 2000, *72* (9), 2132–2141. https://doi.org/10.1021/ac9913659.

(14) Suckau, D.; Resemann, A.; Schuerenberg, M.; Hufnagel, P.; Franzen, J.; Holle, A. A Novel MALDI LIFT-TOF/TOF Mass Spectrometer for Proteomics. *Anal. Bioanal. Chem.* 2003, *376* (7), 952–965. https://doi.org/10.1007/s00216-003-2057-0.

(15) Fuchs, B.; Schiller, J. Application of MALDI-TOF Mass Spectrometry in Lipidomics. *Eur. J. Lipid Sci. Technol.* 2009, *111* (1), 83–98. https://doi.org/10.1002/ejlt.200800223.

(16) Woods, A. S.; Jackson, S. N. Brain Tissue Lipidomics: Direct Probing Using Matrix-Assisted Laser Desorption/Ionization Mass Spectrometry. *AAPS J.* 2006, *8* (2), E391–E395. https://doi.org/10.1007/BF02854910.

(17) Lu, I.-C.; Lee, C.; Lee, Y.-T.; Ni, C.-K. Ionization Mechanism of Matrix-Assisted Laser Desorption/Ionization. *Annu. Rev. Anal. Chem.* 2015, *8* (1), 21–39. https://doi.org/10.1146/annurev-anchem-071114-040315.

(18) Knochenmuss, R.; Zenobi, R. MALDI Ionization: The Role of In-Plume Processes. *Chem. Rev.* 2003, *103* (2), 441–452. https://doi.org/10.1021/cr0103773.

(19) Lu, I.-C.; Lee, C.; Chen, H.-Y.; Lin, H.-Y.; Hung, S.-W.; Dyakov, Y. A.; Hsu, K.-T.; Liao, C.-Y.; Lee, Y.-Y.; Tseng, C.-M.; Lee, Y.-T.; Ni, C.-K. Ion Intensity and Thermal Proton Transfer in Ultraviolet Matrix-Assisted Laser Desorption/Ionization. *J. Phys. Chem. B* 2014, *118* (15), 4132–4139. https://doi.org/10.1021/jp5008076.

(20) Leopold, J.; Popkova, Y.; Engel, K. M.; Schiller, J. Recent Developments of Useful MALDI Matrices for the Mass Spectrometric Characterization of Lipids. *Biomolecules* 2018, *8* (4). https://doi.org/10.3390/biom8040173.

(21) Shroff, R.; Svatoš, A. Proton Sponge: A Novel and Versatile MALDI Matrix for the Analysis of Metabolites Using Mass Spectrometry. *Anal. Chem.* 2009, *81* (19), 7954–7959. https://doi.org/10.1021/ac901048z.

(22) Dong, X.; Cheng, J.; Li, J.; Wang, Y. Graphene as a Novel Matrix for the Analysis of Small Molecules by MALDI-TOF MS. *Anal. Chem.* 2010, *82* (14), 6208–6214. https://doi.org/10.1021/ac101022m.

(23) Berry, K. A. Z.; Hankin, J. A.; Barkley, R. M.; Spraggins, J. M.; Caprioli, R. M.; Murphy, R. C. MALDI Imaging of Lipid Biochemistry in Tissues by Mass Spectrometry. *Chem. Rev.* 2011, *111* (10), 6491–6512. https://doi.org/10.1021/cr200280p.

(24) McDonnell, L. A.; Piersma, S. R.; MaartenAltelaar, A. F.; Mize, T. H.; Luxembourg, S. L.; Verhaert, P. D. E. M.; van Minnen, J.; Heeren, R. M. A. Subcellular Imaging Mass Spectrometry of Brain Tissue. *J. Mass Spectrom. JMS* 2005, *40* (2), 160–168. https://doi.org/10.1002/jms.735.

(25) Eberlin, L. S.; Norton, I.; Dill, A. L.; Golby, A. J.; Ligon, K. L.; Santagata, S.; Cooks, R. G.; Agar, N. Y. R. Classifying Human Brain Tumors by Lipid Imaging with Mass Spectrometry. *Cancer Res.* 2012, *72* (3), 645–654. https://doi.org/10.1158/0008-5472.CAN-11-2465.

(26) Guo, S.; Wang, Y.; Zhou, D.; Li, Z. Significantly Increased Monounsaturated Lipids Relative to Polyunsaturated Lipids in Six Types of Cancer Microenvironment Are Observed by Mass Spectrometry Imaging. *Sci. Rep.* 2014, *4*, 5959. https://doi.org/10.1038/srep05959.

(27) Mehlem, A.; Hagberg, C. E.; Muhl, L.; Eriksson, U.; Falkevall, A. Imaging of Neutral Lipids by Oil Red O for Analyzing the Metabolic Status in Health and Disease. *Nat. Protoc.* 2013, *8* (6), 1149–1154. https://doi.org/10.1038/nprot.2013.055.

(28) Rs, Y.; Nk, T. Lipid Integration in Neurodegeneration: An Overview of Alzheimer's Disease. *Mol. Neurobiol.* 2014, *50* (1), 168–176. https://doi.org/10.1007/s12035-014-8661-5.

(29) Norris, J. L.; Caprioli, R. M. Analysis of Tissue Specimens by Matrix-Assisted Laser Desorption/Ionization Imaging Mass Spectrometry in Biological and Clinical Research. *Chem. Rev.* 2013, *113* (4), 2309–2342. https://doi.org/10.1021/cr3004295.

(30) Hsu, C.-C.; Chou, P.-T.; Zare, R. N. Imaging of Proteins in Tissue Samples Using Nanospray Desorption Electrospray Ionization Mass Spectrometry. *Anal. Chem.* 2015, *87* (22), 11171–11175. https://doi.org/10.1021/acs.analchem.5b03389.

(31) Hsu, C.-C.; Dorrestein, P. C. Visualizing Life with Ambient Mass Spectrometry. *Curr. Opin. Biotechnol.* 2015, *31*, 24–34. https://doi.org/10.1016/j.copbio.2014.07.005.

(32) Caprioli, R. M.; Farmer, T. B.; Gile, J. Molecular Imaging of Biological Samples: Localization of Peptides and Proteins Using MALDI-TOF MS. *Anal. Chem.* 1997, *69* (23), 4751–4760. https://doi.org/10.1021/ac970888i.

(33) Lanni, E. J.; Rubakhin, S. S.; Sweedler, J. V. Mass Spectrometry Imaging and Profiling of Single Cells. *J. Proteomics* 2012, *75* (16), 5036–5051. https://doi.org/10.1016/j.jprot.2012.03.017.

(34) Bednařík, A.; Bölsker, S.; Soltwisch, J.; Dreisewerd, K. An On-Tissue Paternò-Büchi Reaction for Localization of Carbon-Carbon Double Bonds in Phospholipids and Glycolipids by Matrix-Assisted Laser-Desorption-Ionization Mass-Spectrometry

Imaging. *Angew. Chem. Int. Ed Engl.* 2018, *57* (37), 12092–12096. https://doi.org/10.1002/anie.201806635.

(35) Paine, M. R. L.; Poad, B. L. J.; Eijkel, G. B.; Marshall, D. L.; Blanksby, S. J.; Heeren, R. M. A.; Ellis, S. R. Mass Spectrometry Imaging with Isomeric Resolution Enabled by Ozone-Induced Dissociation. *Angew. Chem. Int. Ed.* 2018, *57* (33), 10530–10534. https://doi.org/10.1002/anie.201802937.

(36) Neumann, E. K.; Comi, T. J.; Rubakhin, S. S.; Sweedler, J. V. Lipid Heterogeneity between Astrocytes and Neurons Revealed by Single-Cell MALDI-MS Combined with Immunocytochemical Classification. *Angew. Chem. Int. Ed.* 2019, *58* (18), 5910–5914. https://doi.org/10.1002/anie.201812892.

(37) McDonnell, L. A.; Corthals, G. L.; Willems, S. M.; van Remoortere, A.; van Zeijl, R. J. M.; Deelder, A. M. Peptide and Protein Imaging Mass Spectrometry in Cancer Research. *J. Proteomics* 2010, *73* (10), 1921–1944. https://doi.org/10.1016/j.jprot.2010.05.007.

(38) McDonnell, L. A.; Heeren, R. M. A. Imaging Mass Spectrometry. *Mass Spectrom. Rev.* 2007, *26* (4), 606–643. https://doi.org/10.1002/mas.20124.

(39) Mirnezami, R.; Spagou, K.; Vorkas, P. A.; Lewis, M. R.; Kinross, J.; Want, E.; Shion, H.; Goldin, R. D.; Darzi, A.; Takats, Z.; Holmes, E.; Cloarec, O.; Nicholson, J. K. Chemical Mapping of the Colorectal Cancer Microenvironment via MALDI Imaging Mass Spectrometry (MALDI-MSI) Reveals Novel Cancer-Associated Field Effects. *Mol. Oncol.* 2014, *8* (1), 39–49. https://doi.org/10.1016/j.molonc.2013.08.010.

(40) Wang, F.; Yang, P.; Choi, J.-S.; Antovski, P.; Zhu, Y.; Xu, X.; Kuo, T.-H.; Lin, L.-E.; Kim, D. N. H.; Huang, P.-C.; Xu, H.; Lee, C.-F.; Wang, C.; Hsu, C.-C.; Chen, K.; Weiss,

P. S.; Tseng, H.-R. Cross-Linked Fluorescent Supramolecular Nanoparticles for Intradermal Controlled Release of Antifungal Drug-A Therapeutic Approach for Onychomycosis. *ACS Nano* 2018, *12* (7), 6851–6859. https://doi.org/10.1021/acsnano.8b02099.

(41) Soltwisch, J.; Kettling, H.; Vens-Cappell, S.; Wiegelmann, M.; Muthing, J.; Dreisewerd, K. Mass Spectrometry Imaging with Laser-Induced Postionization. *Science* 2015, *348* (6231), 211–215. https://doi.org/10.1126/science.aaa1051.

(42) Murphy, R. C.; Hankin, J. A.; Barkley, R. M. Imaging of Lipid Species by MALDI Mass Spectrometry. *J. Lipid Res.* 2009, *50 Suppl*, S317-322. https://doi.org/10.1194/jlr.R800051-JLR200.

(43) Jackson, S. N.; Ugarov, M.; Egan, T.; Post, J. D.; Langlais, D.; Schultz, J. A.; Woods, A. S. MALDI-Ion Mobility-TOFMS Imaging of Lipids in Rat Brain Tissue. *J. Mass Spectrom. JMS* 2007, *42* (8), 1093–1098. https://doi.org/10.1002/jms.1245.

(44) Sparvero, L. J.; Amoscato, A. A.; Dixon, C. E.; Long, J. B.; Kochanek, P. M.; Pitt, B. R.; Bayir, H.; Kagan, V. E. Mapping of Phospholipids by MALDI Imaging (MALDI-MSI): Realities and Expectations. *Chem. Phys. Lipids* 2012, *165* (5), 545–562. https://doi.org/10.1016/j.chemphyslip.2012.06.001.

(45) Demeure, K.; Quinton, L.; Gabelica, V.; De Pauw, E. Rational Selection of the Optimum MALDI Matrix for Top-Down Proteomics by In-Source Decay. *Anal. Chem.* 2007, *79* (22), 8678–8685. https://doi.org/10.1021/ac070849z.

(46) L, M.; R, S.; Fr, D.; G, M.; P, T. The Double Nature of 1,5-Diaminonaphthalene as Matrix-Assisted Laser Desorption/Ionization Matrix: Some Experimental Evidence of

the Protonation and Reduction Mechanisms. *Rapid Commun. Mass Spectrom. RCM* 2011, *25* (20), 3091–3096. https://doi.org/10.1002/rcm.5201.

(47) Thomas, A.; Déglon, J.; Lenglet, S.; Mach, F.; Mangin, P.; Wolfender, J.-L.; Steffens, S.; Staub, C. High-Throughput Phospholipidic Fingerprinting by Online Desorption of Dried Spots and Quadrupole-Linear Ion Trap Mass Spectrometry: Evaluation of Atherosclerosis Biomarkers in Mouse Plasma. *Anal. Chem.* 2010, *82* (15), 6687–6694. https://doi.org/10.1021/ac101421b.

(48) Thomas, A.; Charbonneau, J. L.; Fournaise, E.; Chaurand, P. Sublimation of New Matrix Candidates for High Spatial Resolution Imaging Mass Spectrometry of Lipids: Enhanced Information in Both Positive and Negative Polarities after 1,5-Diaminonapthalene Deposition. *Anal. Chem.* 2012, *84* (4), 2048–2054. https://doi.org/10.1021/ac2033547.

(49) Li, B.; Sun, R.; Gordon, A.; Ge, J.; Zhang, Y.; Li, P.; Yang, H. 3-Aminophthalhydrazide (Luminol) As a Matrix for Dual-Polarity MALDI MS Imaging. *Anal. Chem.* 2019, *91* (13), 8221–8228. https://doi.org/10.1021/acs.analchem.9b00803.

(50) Jia, M.-Q.; You, S.-L. N-Heterocyclic Carbene-Catalyzed Enantioselective Intramolecular N-Tethered Aldehyde–Ketone Benzoin Reactions. *ACS Catal.* 2013, *3* (4), 622–624. https://doi.org/10.1021/cs4000014.

(51) Saab, F.; Bénéteau, V.; Schoentgen, F.; Mérour, J.-Y.; Routier, S. Convenient Access to C-2 or C-5 Substituted 4-Azaindole Derivatives. *Tetrahedron* 2010, *66* (1), 102–110. https://doi.org/10.1016/j.tet.2009.11.040.

(52) Geddis, S. M.; Hagerman, C. E.; Galloway, W. R. J. D.; Sore, H. F.; Goodman, J. M.; Spring, D. R. (Z)-Selective Takai Olefination of Salicylaldehydes. *Beilstein J. Org. Chem.* 2017, *13* (1), 323–328. https://doi.org/10.3762/bjoc.13.35.

(53) Thomson, J. E.; Campbell, C. D.; Concellón, C.; Duguet, N.; Rix, K.; Slawin, A. M. Z.; Smith, A. D. Probing the Efficiency of N-Heterocyclic Carbene Promoted O- to C-Carboxyl Transfer of Oxazolyl Carbonates. *J. Org. Chem.* 2008, *73* (7), 2784–2791. https://doi.org/10.1021/jo702720a.

(54) Zapała, L.; Woźnicka, E.; Kalembkiewicz, J. Tautomeric and Microscopic Protonation Equilibria of Anthranilic Acid and Its Derivatives. *J. Solut. Chem.* 2014, *43*, 1167–1183. https://doi.org/10.1007/s10953-014-0190-3.

(55) Böhme, K.; Fernández-No, I. C.; Barros-Velázquez, J.; Gallardo, J. M.; Cañas, B.; Calo-Mata, P. Comparative Analysis of Protein Extraction Methods for the Identification of Seafood-Borne Pathogenic and Spoilage Bacteria by MALDI-TOF Mass Spectrometry. *Anal. Methods* 2010, *2* (12), 1941–1947. https://doi.org/10.1039/C0AY00457J.

(56) Lin, L.-E.; Su, P.-R.; Wu, H.-Y.; Hsu, C.-C. A Simple Sonication Improves Protein Signal in Matrix-Assisted Laser Desorption Ionization Imaging. *J. Am. Soc. Mass Spectrom.* 2018, *29* (4), 796–799. https://doi.org/10.1007/s13361-018-1889-y.

(57) Kuo, T.-H.; Chung, H.-H.; Chang, H.-Y.; Lin, C.-W.; Wang, M.-Y.; Shen, T.-L.; Hsu, C.-C. Deep Lipidomics and Molecular Imaging of Unsaturated Lipid Isomers: A Universal Strategy Initiated by MCPBA Epoxidation. *Anal. Chem.* 2019, *91* (18), 11905–11915. https://doi.org/10.1021/acs.analchem.9b02667.

(58) Hardy, G. E.; Kaska, W. C.; Chandra, B. P.; Zink, J. I. Triboluminescence-Structure Relationships in Polymorphs of Hexaphenylcarbodiphosphorane and Anthranilic Acid, Molecular Crystals, and Salts. *J. Am. Chem. Soc.* 1981, *103* (5), 1074–1079. https://doi.org/10.1021/ja00395a014.

(59) Dhaneshwar, N. N.; Pant, L. M. The Structure of N-Methylanthranilic Acid. *Acta Crystallogr. B* 1972, *28* (2), 647–649. https://doi.org/10.1107/S0567740872002912.

(60) Karas, M.; Bachmann, D.; Bahr, U.; Hillenkamp, F. Matrix-Assisted Ultraviolet Laser Desorption of Non-Volatile Compounds. *Int. J. Mass Spectrom. Ion Process.* 1987, *78*, 53–68. https://doi.org/10.1016/0168-1176(87)87041-6.

(61) Chiurato, M.; Boulahjar, R.; Routier, S.; Troin, Y.; Guillaumet, G. New Efficient Access to Fused (Het)Aryltetrahydroindolizinones via N-Acyl Iminium Intermediates. *Tetrahedron* 2010, *25* (66), 4647–4653. https://doi.org/10.1016/j.tet.2010.03.100.

(62) Hmida, F.; Ayed, B.; Haddad, A. Hydrothermal Synthesis of a New Organic–Inorganic Hybrid with Dawson Type Polyanions as Building Blocks: Na3(C7NH8O2)3[P2W18O62]·16H2O. *J. Mol. Struct.* 2016, *1116*, 218–225. https://doi.org/10.1016/j.molstruc.2016.03.046.

(63) Boroff, J. A.; Matesich, Z. D.; Stuetzer, D. C.; Sobeck, S. J. S. Solvent Impact on the Photophysical Properties and Excited State Behavior of P-Aminobenzoic Acids. *J. Photochem. Photobiol. Chem.* 2015, *C* (305), 60–66. https://doi.org/10.1016/j.jphotochem.2015.03.005.

(64) Thayer, M. P.; McGuire, C.; Stennett, E. M. S.; Lockhart, M. K.; Canache, D.; Novak, M.; Schmidtke, S. J. PH-Dependent Spectral Properties of Para-Aminobenzoic Acid

and Its Derivatives. *Spectrochim. Acta. A. Mol. Biomol. Spectrosc.* 2011, *84* (1), 227–232. https://doi.org/10.1016/j.saa.2011.09.032.

(65) Mirabelli, M. F.; Zenobi, R. Observing Proton Transfer Reactions Inside the MALDI Plume: Experimental and Theoretical Insight into MALDI Gas-Phase Reactions. *J. Am. Soc. Mass Spectrom.* 2017, *28* (8), 1676–1686. https://doi.org/10.1007/s13361-017-1677-0.

(66) Breuker, K.; Knochenmuss, R.; Zenobi, R. Proton Transfer Reactions of Matrix-Assisted Laser Desorption/Ionization Matrix Monomers and Dimers. *J. Am. Soc. Mass Spectrom.* 1999, *10* (11), 1111–1123. https://doi.org/10.1016/S1044-0305(99)00095-1.

(67) Lee, C.; Inutan, E. D.; Chen, J. L.; Mukeku, M. M.; Weidner, S. M.; Trimpin, S.; Ni, C.-K. Toward Understanding the Ionization Mechanism of Matrix-Assisted Ionization Using Mass Spectrometry Experiment and Theory. *Rapid Commun. Mass Spectrom. 0* (0). https://doi.org/10.1002/rcm.8382.

(68) Forbes, W. F. LIGHT ABSORPTION STUDIES: PART XI ELECTRONIC ABSORPTION SPECTRA OF NITROBENZENES. *Can. J. Chem.* 1958, *36* (10), 1350–1361. https://doi.org/10.1139/v58-200.

(69) Min, Y. L.; He, G. Q.; Xu, Q. J.; Chen, Y. C. Enhanced Photoluminescence Emission of 3-Aminobenzoic Acid by Complexation with M Cations [M=cobalt, Zinc]. *J. Alloys Compd.* 2013, *578*, 448–453. https://doi.org/10.1016/j.jallcom.2013.06.078.

(70) Skupiński, W.; Pichnej, L.; Pakula, R.; Jahn-Andrychowska, W.; Trojanowska, Z.; Butkiewicz, K. Preparation of 4-Methylaminobenzoic Acid from Anaesthesin® (4-Aminobenzoic Acid Ethyl Ester) via Phase-Transfer Methylation of Its Amino Group. Herstellung von 4-Methylaminobenzoesäure Aus Anaesthesin® (4-Aminobenzoesäureethylester) Durch Phasentransfer-Methylierung Seiner

Aminogruppe. *Arch. Pharm. (Weinheim)* 1986, *319* (9), 862–864. https://doi.org/10.1002/ardp.19863190915.

(71) Zemski Berry, K. A.; Hankin, J. A.; Barkley, R. M.; Spraggins, J. M.; Caprioli, R. M.; Murphy, R. C. MALDI Imaging of Lipid Biochemistry in Tissues by Mass Spectrometry. *Chem. Rev.* 2011, *111* (10), 6491–6512. https://doi.org/10.1021/cr200280p.

(72) Guo, S.; Wang, Y.; Zhou, D.; Li, Z. Significantly Increased Monounsaturated Lipids Relative to Polyunsaturated Lipids in Six Types of Cancer Microenvironment Are Observed by Mass Spectrometry Imaging. *Sci. Rep.* 2014, *4*, 5959. https://doi.org/10.1038/srep05959.

(73) Thomas, A.; Charbonneau, J. L.; Fournaise, E.; Chaurand, P. Sublimation of New Matrix Candidates for High Spatial Resolution Imaging Mass Spectrometry of Lipids: Enhanced Information in Both Positive and Negative Polarities after 1,5-Diaminonapthalene Deposition. *Anal. Chem.* 2012, *84* (4), 2048–2054. https://doi.org/10.1021/ac2033547.

(74) Karas, Michael.; Bachmann, Doris.; Hillenkamp, Franz. Influence of the Wavelength in High-Irradiance Ultraviolet Laser Desorption Mass Spectrometry of Organic Molecules. *Anal. Chem.* 1985, *57* (14), 2935–2939. https://doi.org/10.1021/ac00291a042.

(75) Schröter, J.; Fülöp, A.; Hopf, C.; Schiller, J. The Combination of 2,5-Dihydroxybenzoic Acid and 2,5-Dihydroxyacetophenone Matrices for Unequivocal Assignment of Phosphatidylethanolamine Species in Complex Mixtures. *Anal. Bioanal. Chem.* 2018, *410* (9), 2437–2447. https://doi.org/10.1007/s00216-018-0926-9.

(76) Thomas, A.; Charbonneau, J. L.; Fournaise, E.; Chaurand, P. Sublimation of New Matrix Candidates for High Spatial Resolution Imaging Mass Spectrometry of Lipids:

Enhanced Information in Both Positive and Negative Polarities after 1,5-Diaminonapthalene Deposition. *Anal. Chem.* 2012, *84* (4), 2048–2054. https://doi.org/10.1021/ac2033547.

(77) Fuchs, B.; Bischoff, A.; Süss, R.; Teuber, K.; Schürenberg, M.; Suckau, D.; Schiller, J. Phosphatidylcholines and -Ethanolamines Can Be Easily Mistaken in Phospholipid Mixtures: A Negative Ion MALDI-TOF MS Study with 9-Aminoacridine as Matrix and Egg Yolk as Selected Example. *Anal. Bioanal. Chem.* 2009, *395* (8), 2479–2487. https://doi.org/10.1007/s00216-009-3032-1.

(78) Leopold, J.; Popkova, Y.; Engel, K. M.; Schiller, J. Recent Developments of Useful MALDI Matrices for the Mass Spectrometric Characterization of Lipids. *Biomolecules* 2018, *8* (4). https://doi.org/10.3390/biom8040173.

(79) Wang, H.-Y. J.; Jackson, S. N.; Woods, A. S. Direct MALDI-MS Analysis of Cardiolipin from Rat Organs Sections. *J. Am. Soc. Mass Spectrom.* 2007, *18* (3), 567–577. https://doi.org/10.1016/j.jasms.2006.10.023.

(80) Sakai, M.; Martinez-Arguelles, D. B.; Patterson, N. H.; Chaurand, P.; Papadopoulos, V. In Search of the Molecular Mechanisms Mediating the Inhibitory Effect of the GnRH Antagonist Degarelix on Human Prostate Cell Growth. *PLOS ONE* 2015, *10* (3), e0120670. https://doi.org/10.1371/journal.pone.0120670.

(81) Li, S.; Zhang, Y.; Liu, J.; Han, J.; Guan, M.; Yang, H.; Lin, Y.; Xiong, S.; Zhao, Z. Electrospray Deposition Device Used to Precisely Control the Matrix Crystal to Improve the Performance of MALDI MSI. *Sci. Rep.* 2016, *6*, 37903. https://doi.org/10.1038/srep37903.

(82) Wiseman, J. M.; Ifa, D. R.; Song, Q.; Cooks, R. G. Tissue Imaging at Atmospheric Pressure Using Desorption Electrospray Ionization (DESI) Mass Spectrometry. *Angew. Chem. Int. Ed.* 2006, *45* (43), 7188–7192. https://doi.org/10.1002/anie.200602449.

(83) Eberlin, L. S.; Ifa, D. R.; Wu, C.; Cooks, R. G. Three-Dimensional Vizualization of Mouse Brain by Lipid Analysis Using Ambient Ionization Mass Spectrometry. *Angew. Chem. Int. Ed Engl.* 2010, *49* (5), 873–876. https://doi.org/10.1002/anie.200906283.

(84) Wu, Q.; Chu, J. L.; Rubakhin, S. S.; Gillette, M. U.; Sweedler, J. V. Dopamine-Modified TiO2 Monolith-Assisted LDI MS Imaging for Simultaneous Localization of Small Metabolites and Lipids in Mouse Brain Tissue with Enhanced Detection Selectivity and Sensitivity. *Chem. Sci.* 2017, *8* (5), 3926–3938. https://doi.org/10.1039/C7SC00937B.

(85) Horatz, K.; Giampà, M.; Karpov, Y.; Sahre, K.; Bednarz, H.; Kiriy, A.; Voit, B.; Niehaus, K.; Hadjichristidis, N.; Michels, D. L.; Lissel, F. Conjugated Polymers as a New Class of Dual-Mode Matrices for MALDI Mass Spectrometry and Imaging. *J. Am. Chem. Soc.* 2018, *140* (36), 11416–11423. https://doi.org/10.1021/jacs.8b06637.

(86) Ellis, S. R.; Cappell, J.; Potočnik, N. O.; Balluff, B.; Hamaide, J.; Linden, A. V. der; Heeren, R. M. A. More from Less: High-Throughput Dual Polarity Lipid Imaging of Biological Tissues. *Analyst* 2016, *141* (12), 3832–3841. https://doi.org/10.1039/C6AN00169F.

(87) Jia, M.-Q.; You, S.-L. N-Heterocyclic Carbene-Catalyzed Enantioselective Intramolecular N-Tethered Aldehyde–Ketone Benzoin Reactions. *ACS Catal.* 2013, *3* (4), 622–624. https://doi.org/10.1021/cs4000014.

(88) Geddis, S. M.; Hagerman, C. E.; Galloway, W. R. J. D.; Sore, H. F.; Goodman, J. M.; Spring, D. R. (Z)-Selective Takai Olefination of Salicylaldehydes. *Beilstein J. Org. Chem.* 2017, *13*, 323–328. https://doi.org/10.3762/bjoc.13.35.

(89) Ra, A.; L, M. New Gas-Phase Cascade Reactions of Stabilized Phosphorus Ylides Leading to Ring-Fused Indoles and to Quinolines. *J. Org. Chem.* 2008, *73* (24), 9781–9783. https://doi.org/10.1021/jo801716z.

(90) Nepomuceno, G. M.; Chan, K. M.; Huynh, V.; Martin, K. S.; Moore, J. T.; O'Brien, T. E.; Pollo, L. A. E.; Sarabia, F. J.; Tadeus, C.; Yao, Z.; Anderson, D. E.; Ames, J. B.; Shaw, J. T. Synthesis and Evaluation of Quinazolines as Inhibitors of the Bacterial Cell Division Protein FtsZ. *ACS Med. Chem. Lett.* 2015, *6* (3), 308–312. https://doi.org/10.1021/ml500497s.

(91) Okamura, T.; Nakagawa, J. Contribution of Intramolecular NH···O Hydrogen Bonds to Magnesium–Carboxylate Bonds. *Inorg. Chem.* 2013, *52* (19), 10812–10824. https://doi.org/10.1021/ic400671v.

(92) Shanta, S. R.; Zhou, L.-H.; Park, Y. S.; Kim, Y. H.; Kim, Y.; Kim, K. P. Binary Matrix for MALDI Imaging Mass Spectrometry of Phospholipids in Both Ion Modes. *Anal. Chem.* 2011, *83* (4), 1252–1259. https://doi.org/10.1021/ac1029659.

(93) Ellis, S. R.; Soltwisch, J.; Paine, M. R. L.; Dreisewerd, K.; Heeren, R. M. A. Laser Post-Ionisation Combined with a High Resolving Power Orbitrap Mass Spectrometer for Enhanced MALDI-MS Imaging of Lipids. *Chem. Commun.* 2017, *53* (53), 7246–7249. https://doi.org/10.1039/C7CC02325A.

(94) R. Ellis, S.; Soltwisch, J.; L. Paine, M. R.; Dreisewerd, K.; A. Heeren, R. M. Laser Post-Ionisation Combined with a High Resolving Power Orbitrap Mass Spectrometer for

Enhanced MALDI-MS Imaging of Lipids. *Chem. Commun.* 2017, *53* (53), 7246–7249. https://doi.org/10.1039/C7CC02325A.

(95) Guo, S.; Wang, Y.; Zhou, D.; Li, Z. Significantly Increased Monounsaturated Lipids Relative to Polyunsaturated Lipids in Six Types of Cancer Microenvironment Are Observed by Mass Spectrometry Imaging. *Sci. Rep.* 2014, *4*, 5959.

Appendix A. Synthesis of a series of anthranilic acid derivatives.

A-1 Synthesis of 2-aminobenzaldehyde (CHO-NH$_2$, II). [51,87]

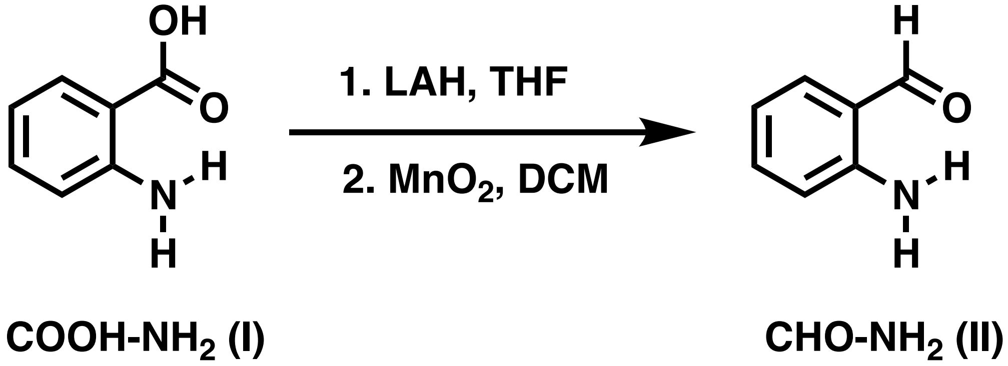

To a solution of anthranilic acid (1.0 g, 7.30 mmol) in dry THF (20 mL) was added dropwise a solution of lithium aluminum hydride (LAH) in THF (2.4M, 4.6 mL, 11.04 mmol) while the temperature was maintained at -30°C with stirring. The resulting mixture was allowed to warm to room temperature and stirred in the same temperature for additional 6 h. Until the end of the reaction, the mixture was hydrolyzed by addition of water (20 mL) and 5% NaOH (2.0 mL). The resulting suspension was extracted with EtOAc (3 × 50 mL). The combined organic layer was dried over anhydrous $MgSO_4$. The dried organic solution was then filtered and concentrated under reduced pressure. The residue was recrystallized from ethyl acetate and hexane, affording the corresponding 2-aminobenzyl alcohol quantitatively as a white solid. A solution of 2-aminobenzyl alcohol (0.70 g, 5.68 mmol) was dissolved in DCM (50 mL). Manganese (IV) oxide (3.95 g, 45.43 mmol) was added and the reaction mixture was stirred at room temperature for about 12 h. Manganese (IV) oxide was filtered off and the resulting filtrate was concentrated under reduced pressure. The residue was purified by column chromatography on silica gel (hexane:EtOAc = 10:1) to afford CHO-NH$_2$ (**II**) (0.46 g, 67%) as yellow solid. ^{1}H NMR (400

MHz, DMSO-d_6, 298 K) δ (ppm): 9.81 (s, 1H), 7.52 (d, *J* = 8.0 Hz, 1H), 7.30 (t, *J* = 8.0 Hz, 1H), 7.11 (b, 1H), 6.75 (d, *J* = 8.0 Hz, 1H), 6.64 (t, *J* = 8.0 Hz, 1H); ^{13}C NMR (100 MHz, DMSO-d_6, 298 K) δ (ppm): 193.97, 150.66, 135.55, 135.04, 117.74, 115.80, 114.91.

A-2 Synthesis of N-(2-formylphenyl)acetamide (CHO-NHAc, III). [88]

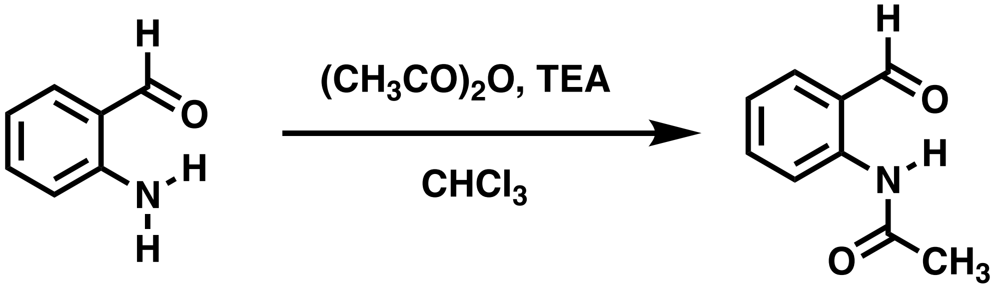

CHO-NH$_2$ (II)

CHO-NHAc (III)

2-Aminobenzaldehyde (CHO-NHAc, **II**, 0.3 g, 2.48 mmol), acetic anhydride (0.33 g, 3.22mmol) and triethylamine (TEA, 0.376 g, 3.72 mmol) were dissolved in $CHCl_3$ (15 mL). The mixture was refluxed at 60 °C for 24 h. After cooling to room temperature, the reaction mixture was poured into water (60 mL), and the aqueous layer was extracted with $CHCl_3$ (3 × 30 mL). The combined organic layer was washed with 1M HCl (60 mL) and dried over anhydrous $MgSO_4$. The dried organic solution was filtered and concentrated under reduced pressure. The residue was purified by column chromatography on silica gel (hexane:CH_2Cl_2 = 5:1) to afford CHO-NHAc (**III**) (0.235 g, 58%) as white solid. ^{1}H NMR (400 MHz, DMSO-d_6, 298 K) δ (ppm): 10.71 (b, 1H), 9.96 (s, 1H), 8.10 (d, J = 8.0 Hz, 1H), 7.84 (d, *J* = 12.0 Hz, 1H), 7.66 (m, 1H), 7.30 (m, 1H), 2.15 (s, 3H); ^{13}C NMR (100 MHz, DMSO-d_6, 298 K) δ (ppm): 193.9, 169.2, 139.8, 135.2, 132.8, 124.4, 123.8, 121.1, 24.3.

A-3 Synthesis of 2-(methylamino)benzoic acid (COOH-NHMe, IV).[89]

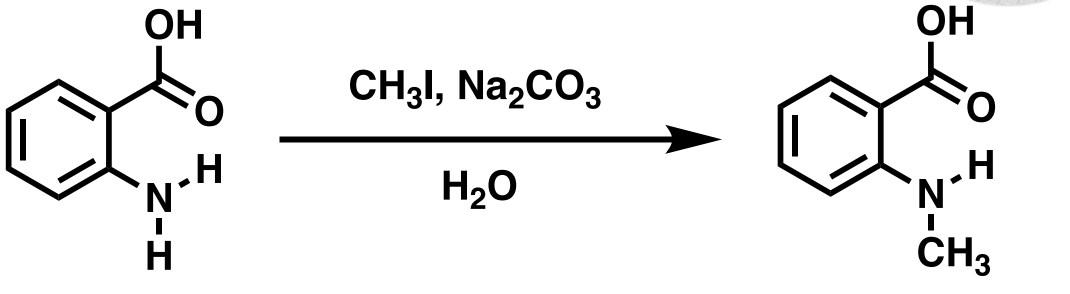

COOH-NH$_2$ (I) **COOH-NHMe (IV)**

To a solution of sodium carbonate (4.0 g, 37.9 mmol) in water (70 mL) was added anthranilic acid (COOH-NH$_2$, **I**, 10.0 g, 72.9 mmol) with stirring, followed by dropwise addition of methyl iodide (5.5 mL, 87.5 mmol) at room temperature. After the addition was complete, the mixture was refluxed at 110 °C for 4 h. After cooling to room temperature, water (300 mL) was added to the solution, the organic layer was separated, and the aqueous layer was extracted with EtOAc (3 × 150 mL). The combined organic layer was dried over anhydrous $MgSO_4$. The dried organic solution was filtered and concentrated under reduced pressure. The residue was purified by column chromatography on silica gel (hexane:EtOAc = 5:2) to afford COOH-NHMe (**IV**) (6.95 g, 63%) as white solid. ^{1}H NMR (400 MHz, DMSO-d$_6$, 298 K) δ (ppm): 7.77 (dd, *J* = 12.0, 4.0 Hz, 1H), 7.40-7.35 (m, 1H), 6.67 (d, *J* = 8.0 Hz, 1H), 6.55 (t, *J* = 8.0 Hz, 1H), 2.83 (s, 3H); ^{13}C NMR (100 MHz, DMSO-d$_6$, 298 K) δ (ppm): 169.90, 151.68, 134.47, 131.55, 113.92, 110.67, 109.88, 29.16.

A-4 Synthesis of 2-acetamidobenzoic acid (COOH-NHAc, V).[90]

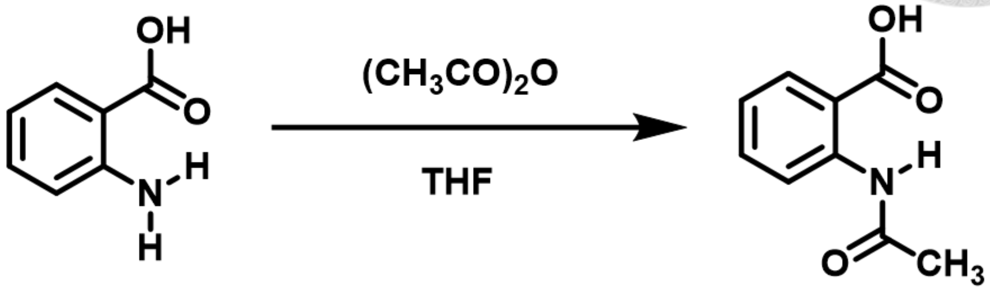

COOH-NH_2 (I)

COOH-NHAc (V)

To a solution of anthranilic acid (2.0 g, 14.6 mmol) in THF (30 mL), acetic anhydride (1.6 mL, 16.8 mmol) was added with stirring and the resulting mixture was then heated to reflux for 1h. After cooling to room temperature, the reaction mixture was poured into water (100 mL), and the aqueous layer was extracted with ethyl acetate (3 × 50 mL). The combined organic layer was dried over anhydrous $MgSO_4$. The dried organic solution was filtered and concentrated under reduced pressure. The residue was purified by column chromatography on silica gel (hexane:EtOAc = 2:1) to afford COOH-NHAc (**V**) (1.88 g, 72%) as white solid. ^1H NMR (400 MHz, DMSO-d_6, 298 K) δ (ppm): 13.57 (b, 1H), 11.05 (b, 1H), 8.45 (dd, J = 12.0, 4.0 Hz, 1H), 7.96 (dd, *J* = 12.0, 4.0 Hz, 1H), 7.57 (t, J = 8.0 Hz, 1H), 7.14 (t, J = 8.0 Hz, 1H), 2.12 (s, 3H); ^{13}C NMR (100 MHz, DMSO-d_6, 298 K) δ (ppm): 169.45, 169.43, 140.83, 133.95, 131.01, 122.51, 119.92, 116.48, 24.98.

A-5 Synthesis of 2-(2,2,2-trifluoroacetamido)benzoic acid(COOH-NHCOCF$_3$, VI).[91]

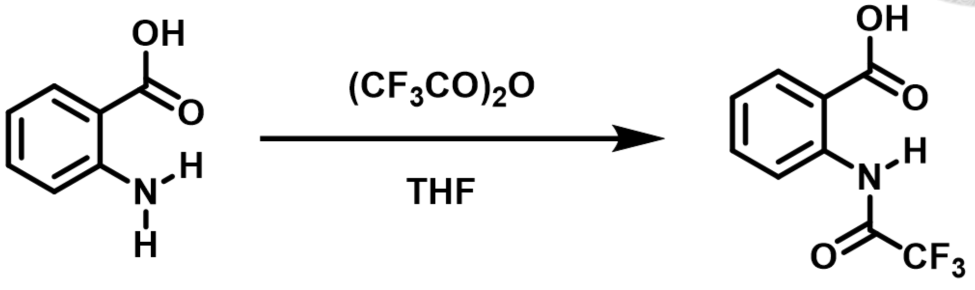

COOH-NH$_2$ (I)

COOH-NHCOCF$_3$ (VI)

To a stirred solution of anthranilic acid (1.87 g, 13.6 mmol) in THF (30 mL), trifluoroacetic anhydride (2.4 mL, 17.3 mmol) was added at 0°C and the resulting mixture was then stirred at room temperature for 16h. At the end of the reaction, the solvent was concentrated under reduced pressure to give a white powder. The residue was dissolved in ethyl acetate, washed with saturated NaCl aqueous solution, and dried over anhydrous $MgSO_4$. The dried organic solution was filtered and concentrated under reduced pressure. The residue was purified by column chromatography on silica gel (hexane:EtOAc = 5:2) to afford COOH-NHCOCF$_3$ (**VI**) (1.85 g, 58%) as white solid. ^{1}H NMR (400 MHz, DMSO-d_6, 298 K) δ (ppm): 12.50 (brs, 1H), 8.27 (d, J = 8.0 Hz, 1H), 8.05 (d, J = 8.0 Hz, 1H), 7.71 (m, 1H), 7.36 (t, J = 8.0 Hz, 1H); ^{13}C NMR (100 MHz, DMSO-d_6, 298 K) δ (ppm): 169.3, 154.8, 154.4, 154.1, 153.7, 137.5, 134.3, 131.3, 125.5, 121.3, 119.9, 119.3, 117.0, 114.2, 111.3; ^{19}F NMR (376 MHz, DMSO-d_6, 298 K) δ (ppm): -75.67.

A-6 Synthesis of 2,2,2-trifluoro-N-(2-formylphenyl)acetamide (CHO-NHCOCF$_3$, VII).

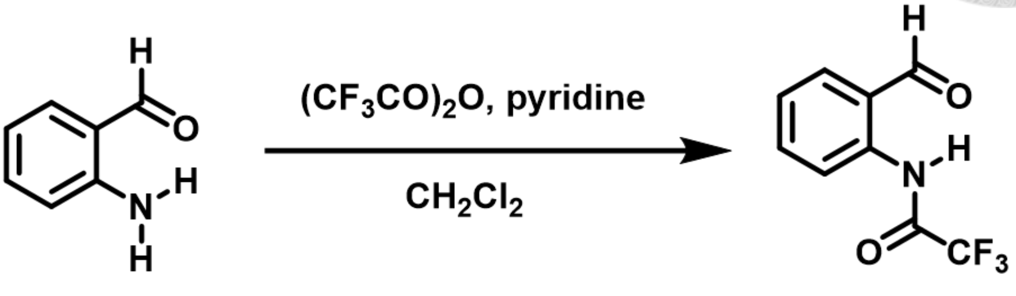

CHO-NH$_2$ (II)

CHO-NHCOCF$_3$ (VII)

To a cold solution of 2-aminobenzaldehyde (0.225 g, 1.86 mmol) in anhydrous CH_2Cl_2 (15 mL) was added anhydrous pyridine (0.3 mL, 3.72 mmol), followed by dropwise addition of trifluoroacetic anhydride (0.336 mL, 2.42 mmol). After the addition was complete, the resulting mixture was warmed to room temperature and stirred in the same temperature for additional 4 h. Until the end of the reaction, 1M HCl (5 mL) was added to the solution, the organic layer was separated, and the aqueous layer was extracted with CH_2Cl_2 (3 × 10 mL). The combined organic layer was dried over anhydrous $MgSO_4$. The dried organic solution was filtered and concentrated under reduced pressure. The residue was purified by column chromatography on silica gel (hexane:CH_2Cl_2 = 5:1) to afford CHO-NHCOCF$_3$ (**VII**) (0.286 g, 71%) as white solid. ^{1}H NMR (400 MHz, DMSO-d$_6$, 298 K) δ (ppm): 11.94 (b, 1H), 10.04 (s, 1H), 8.05 (d, J = 12.0 Hz, 1H), 7.99 (dd, *J* = 12.0, 4.0 Hz, 1H), 7.79 (m, 1H), 7.53 (m, 1H); ^{13}C NMR (100 MHz, DMSO-d$_6$, 298 K) δ (ppm): 194.39, 155.68, 155.31, 154.94, 154.57, 136.58, 135.56, 133.67, 126.46, 125.74, 122.49, 119.87, 117.00, 114.13, 111.26; ^{19}F NMR (376 MHz, DMSO-d$_6$, 298 K) δ (ppm): -75.32; HRMS (EI) m/z: [M+] calc'd for C9H6F3NO2 [217.0351]; found 217.0351.

A-7 Synthesis of (2-(methylamino)phenyl)methanol (S1).

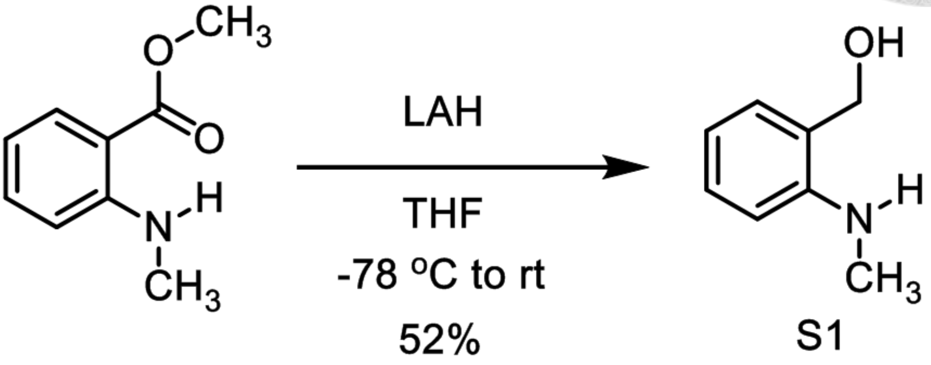

Methyl *N*-methylanthranilate (6.42 g, 38.9 mmol) in dry THF (25 mL) was added rapidly to a stirred solution of lithium aluminum hydride (LAH, 2.4 M in THF, 24.3 mL, 58.2 mmol) in dry THF (100 mL) at -78 °C by a cannula. The reaction mixture was allowed to warm to room temperature and stirred in the same temperature for additional 5h. Until the end of the reaction, water (100 mL) was slowly added to the solution. The aqueous layer was extracted with EtOAc (3 × 100 mL). The combined organic layers were dried over $MgSO_4$. The dried solution was filtered and concentrated under reduced pressure. The residue was purified by column chromatography on silica gel (hexane:EtOAc = 5:2) to afford **S1** (3.26 g, 61%) as colorless oil. ^1H NMR (400 MHz, DMSO-d_6, 298 K) δ (ppm): 7.10 (m, 2H), 6.57 (t, *J* = 8.0 Hz, 1H), 6.52 (d, *J* = 8.0 Hz, 1H), 5.13 (m, 1H), 5.07 (t, *J* = 4.0 Hz, 1H), 4.41 (d, *J* = 4.0 Hz, 2H), 2.73 (d, *J* = 4.0 Hz, 3H); ^{13}C NMR (100 MHz, DMSO-d_6, 298 K) δ (ppm): 147.4, 128.0, 127.3, 125.7, 115.2, 108.8, 61.2, 29.9.

A-8 Synthesis of 2-(methylamino)benzaldehyde (CHO-NHMe, IX).

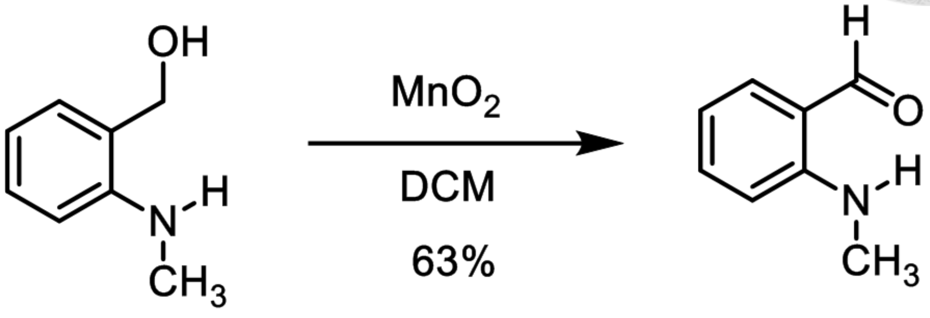

S1 CHO-NHMe

(2-(methylamino)phenyl)methanol (S1, 0.43 g, 3.17 mmol) in dry DCM (8 mL) was added rapidly to a stirred solution of manganese(IV) oxide (MnO_2, 1.1 g, 12.66 mmol) in dry DCM (12 mL) by a cannula. Keep the reaction temperature at 30 °C for 18 h. After cooling to room temperature, the reaction mixture was filtrated, and the combined organic layers were concentrated under reduced pressure. The residue was purified by column chromatography on silica gel (hexane:EtOAc = 5:1) to afford **IX** (0.27 g, 63%) as yellow oil. ^{1}H NMR (400 MHz, DMSO-d_6, 298 K) δ (ppm): 9.80 (s, 1H), 8.14 (b, 1H), 7.58 (dd, *J* = 12.0, 4.0 Hz, 1H), 7.45 (t, *J* = 8.0 Hz, 1H), 6.70 (m, 2H), 2.86 (d, *J* = 4.0 Hz, 3H); ^{13}C NMR (100 MHz, DMSO-d_6, 298 K) δ (ppm): 194.0, 150.8, 136.5, 135.9, 118.0, 114.5, 110.5, 28.8; LRMS (EI) m/z: [M+] calc'd for C8H9NO [135.1]; found 135.1.

Appendix B. Supplementary Information

B-1 Control Experiments

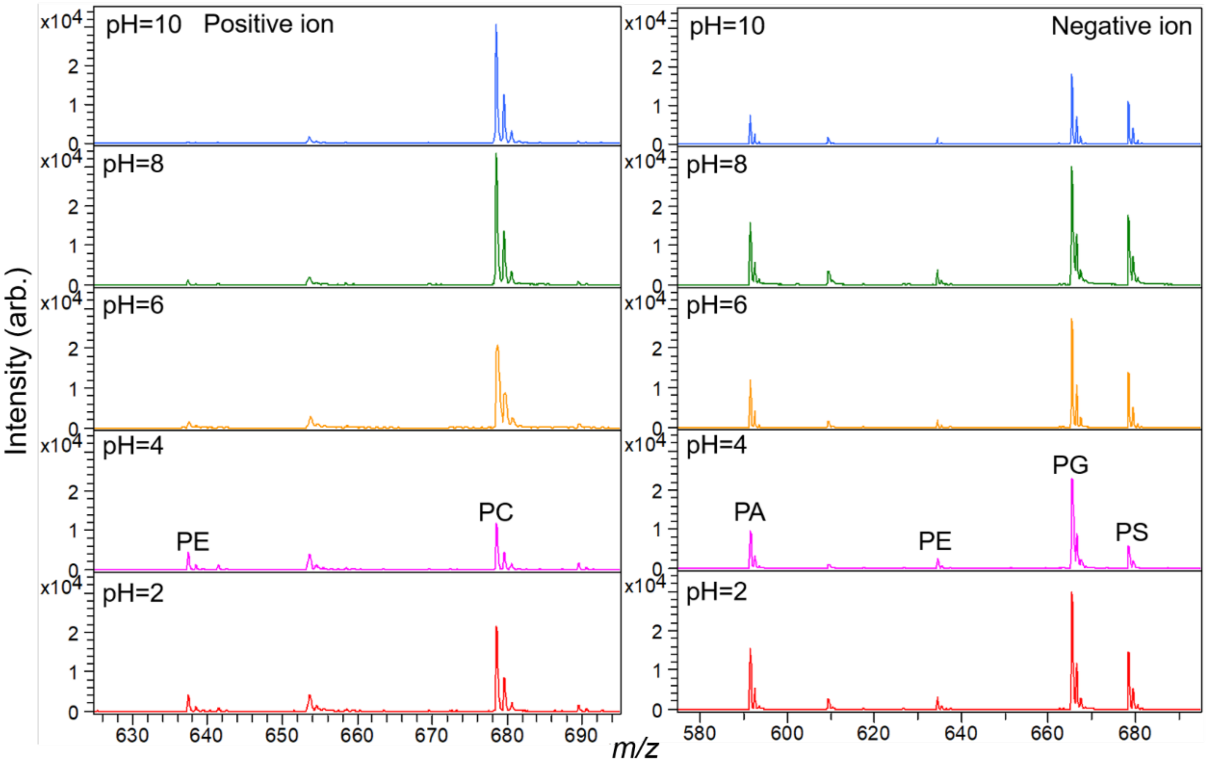

Figure S1. Mass spectra of lipid signals obtained from samples prepared by using COOH-NHMe (**IV**) at different pH values in positive and negative ion mode, respectively. Lipid species are observed at m/z 637.4, 678.5, 591.5, 634.5, 665.5 and 678.6 corresponding to protonated PE(14:0/14:0), protonated PC(14:0/14:0), deprotonated PA(14:0/14:0), deprotonated PE(14:0/14:0), deprotonated PG(14:0/14:0) and deprotonated PS(14:0/14:0), respectively. Each mass spectrum was an accumulation of 300 laser shots.

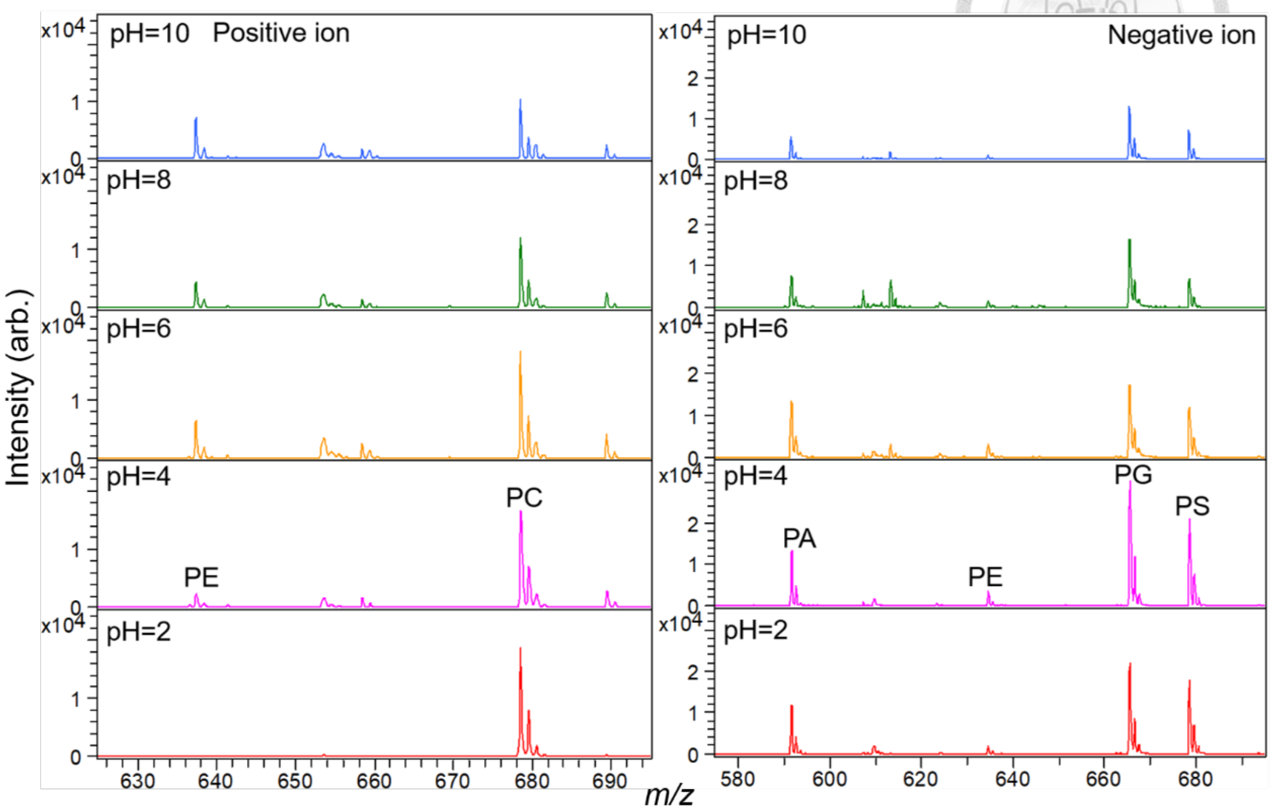

Figure S2. COOH-NH_2 (**I**) Mass spectra of lipid signals obtained from samples prepared by using COOH-NH_2 (**I**) at different pH values in positive and negative ion mode, respectively. Lipid species are observed at *m/z* 637.4, 678.5, 591.5, 634.5, 665.5 and 678.6, corresponding to protonated PE(14:0/14:0), protonated PC(14:0/14:0), deprotonated PA(14:0/14:0), deprotonated PE(14:0/14:0), deprotonated PG(14:0/14:0) and deprotonated PS(14:0/14:0), respectively. Each mass spectrum is an accumulation of 300 laser shots.

Comparison of matrices using statistical analysis

Protein (bovine insulin, ubiquitin, cytochrom C and myoglobin) and lipid (PA, PC, PG and PS) standard were used as analyte for comparison of eight matrices, including COOH-NHMe (**IV**), COOH-NH$_2$ (**I**), CHCA, 2,5-DHB, 2,5-DHAP, SA, 9-AA and 1,5-DAN. Ion yield, signal-to-noise and mass resolution were considered to optimize the laser energy for each matrix. After the optimization, MS data were accumulated three times for statistical analysis as shown in **Figure S8-9.** The laser spot was set to medium, while the laser energies were set between 30% to 80%. The detail information was described in the figure legend.

As we know, "hot spots" remain a common problem for MALDI samples, so the standard deviations are large. However, from the statistical result, it showed that COOH-NHMe (**IV**) had better performance in lipid analysis and was also capable of analyzing proteins in positive ion modes. For the comparison of these matrices, COOH-NHMe (**IV**), SA and 2,5-DHAP provide high performance in positive ion detection, but SA show slightly better result than COOH-NHMe (**IV**) and 2,5-DHAP in negative ion detection. To compare these eight matrices, a maximum analyte signal was selected as normalized parameter. The analyte signals from these eight matrices were divide by the maximum analyte signal. Heat map represents their relative intensity as shown in **Figure S10.**

B-2 Supplementary Figures

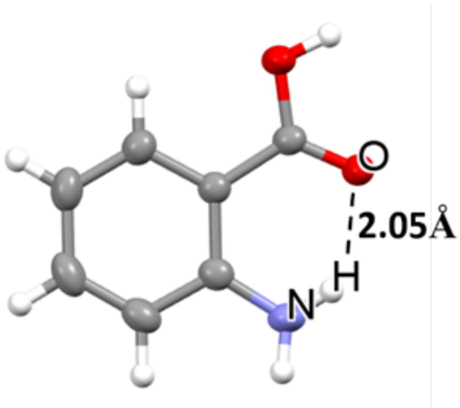

Figure S3. Crystal structure of COOH-NH_2 (**I**) resolved from single X-ray analysis. The corresponding O-N distance was measured to be 2.70 Å.

NMR spectra (alcohol.)

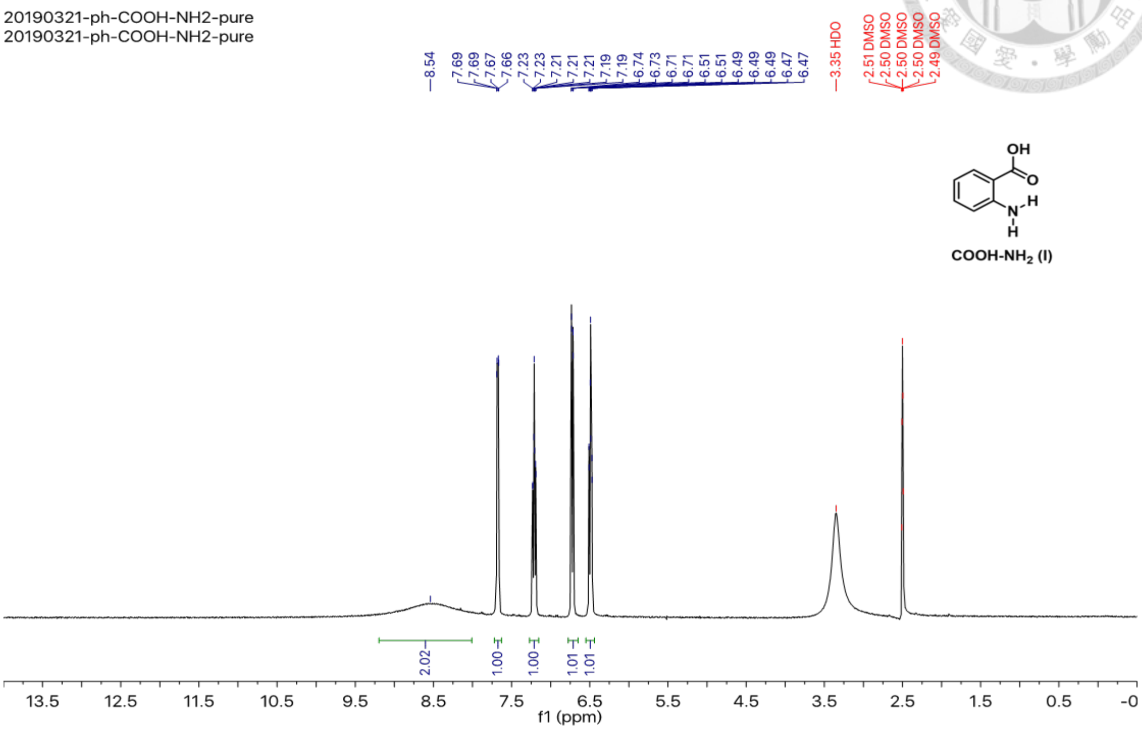

Figure S4. ^{1}H NMR spectrum (400 MHz, DMSO-d$_6$, 298K) of **COOH-NH$_2$ (I).**

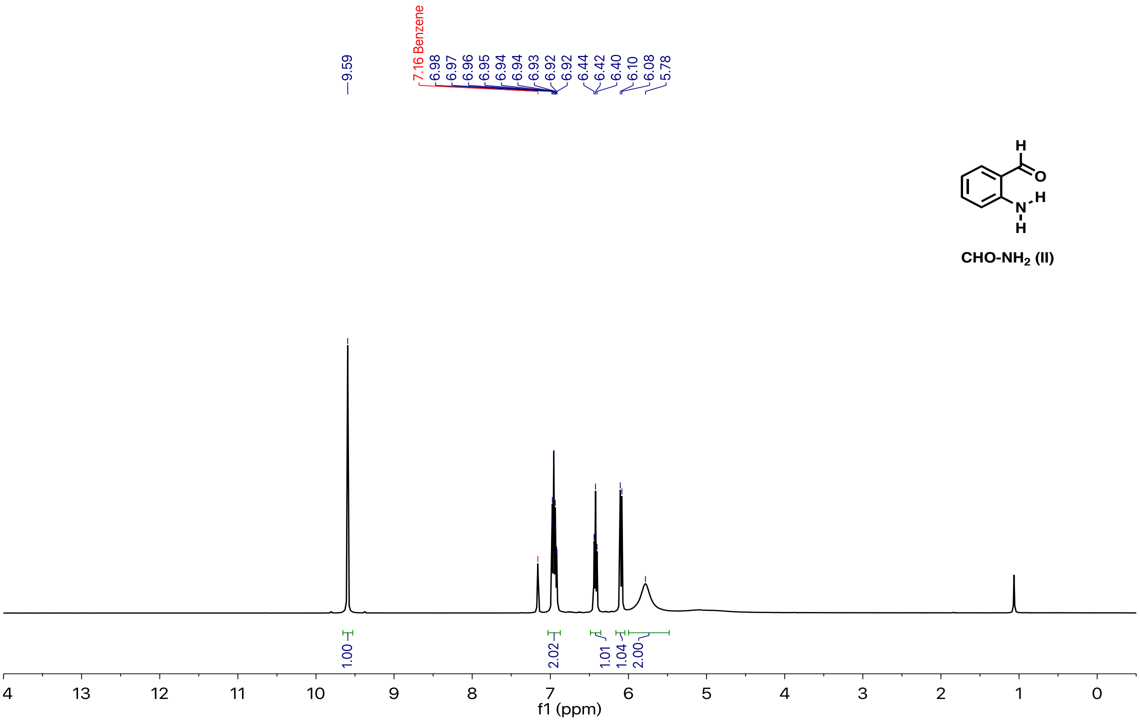

Figure S5. ^{1}H NMR spectrum (400 MHz, Benzene-d$_6$, 298K) of **CHO-NH$_2$ (II).**

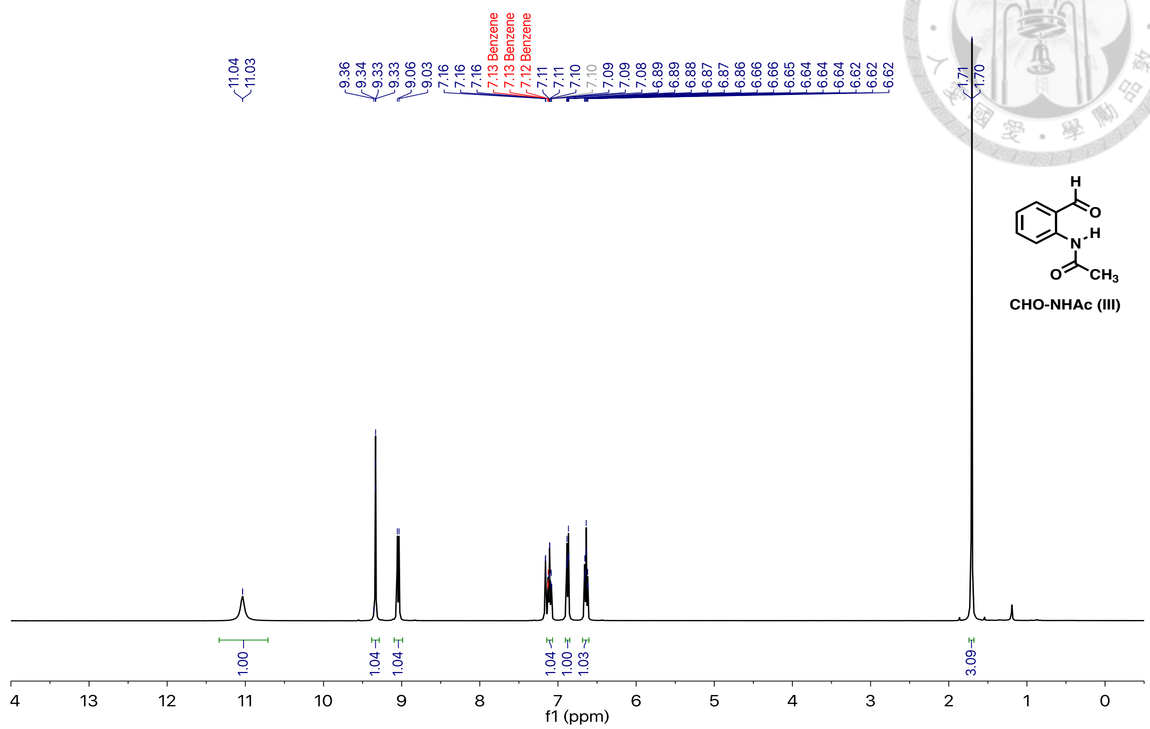

Figure S6. ^{1}H NMR spectrum (400 MHz, Benzene-d6, 298K) of **CHO-NHAc (III).**

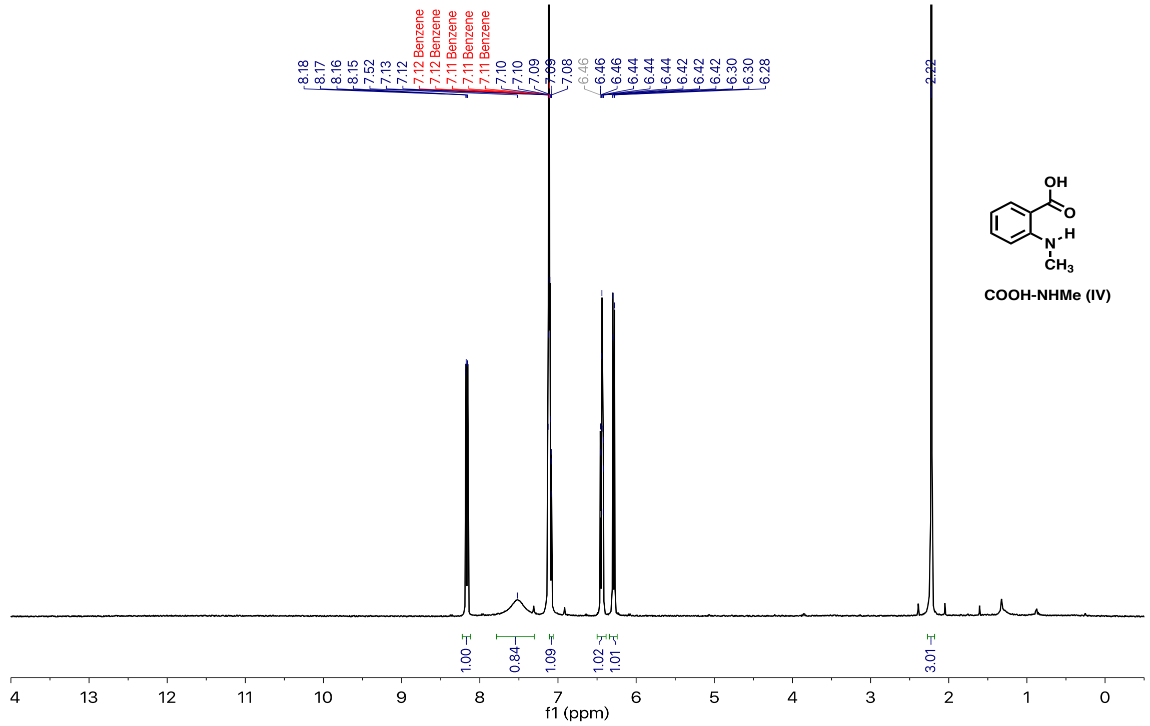

Figure S7. ^{1}H NMR spectrum (400 MHz, Benzene-d$_6$, 298K) of **COOH-NHMe (IV).**

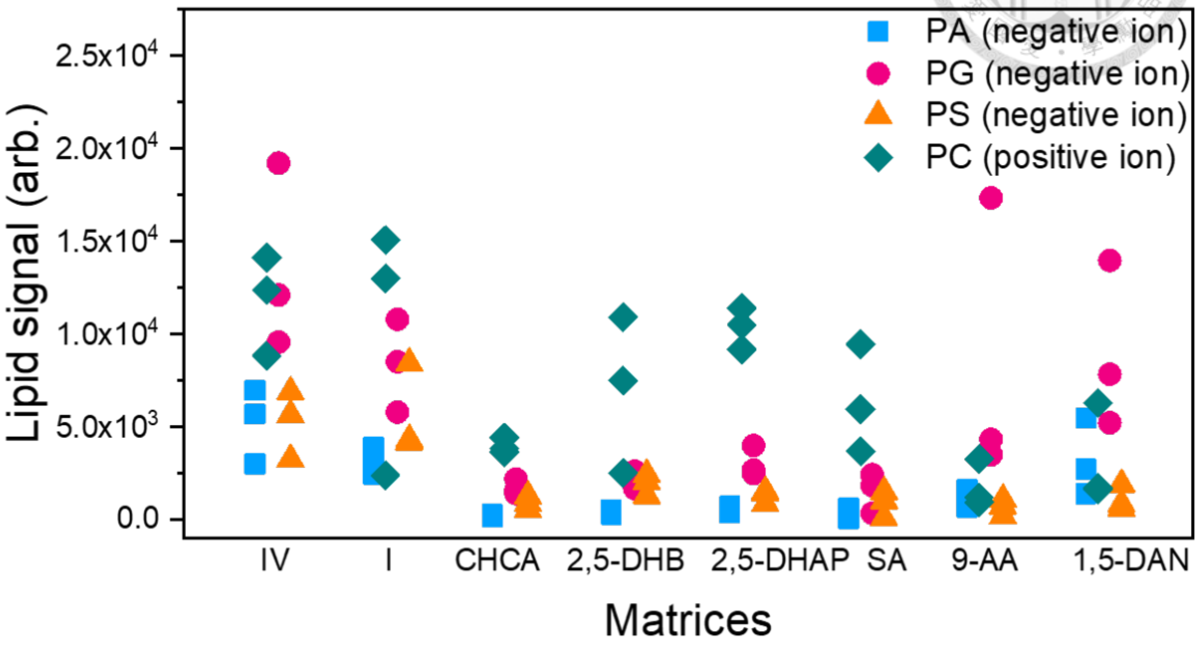

Figure S8. Signal comparison of PA(14:0/14:0), PG(14:0/14:0), PS(14:0/14:0) and PC(14:0/14:0) from the lipid mixture using new MALDI matrices COOH-NH_2 (**I**), COOH-NHMe (**IV**) and some of the most representative commercially available matrices (CHCA, 2,5-DHB, 2,5-DHAP, SA, 9-AA and 1,5-DAN). Deprotonated PA(14:0/14:0), deprotonated PG(14:0/14:0) and deprotonated PS(14:0/14:0) are observed in the negative ion mode. Protonated PC(14:0/14:0) is observed in the positive. Laser energy: COOH-NHMe (**IV**) 70%, COOH-NH_2 (**I**) 50%, CHCA 30%, 2,5-DHB 70%, SA 50%, 9-AA 70%, 1,5-DAN 70%.

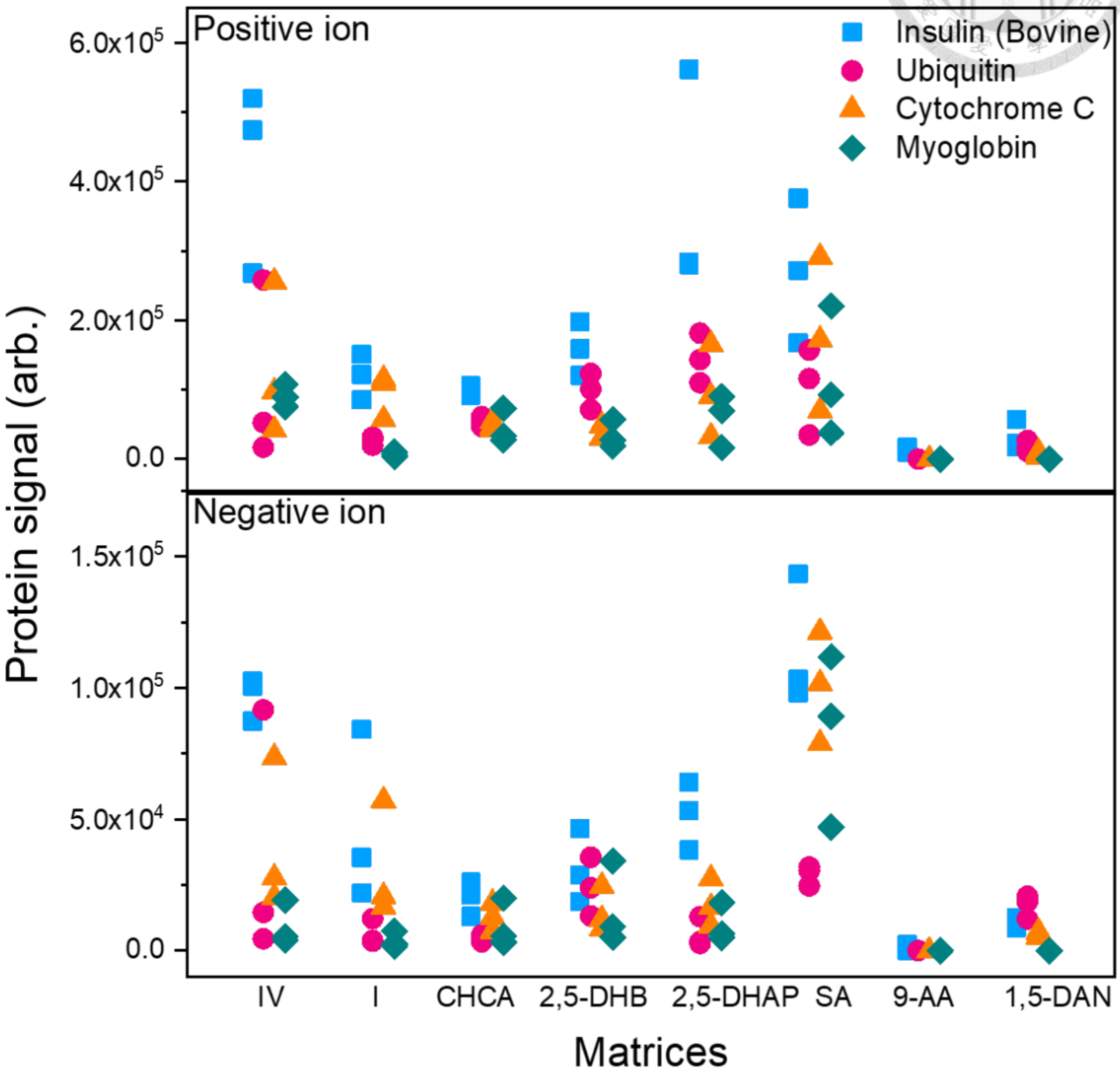

Figure S9. Signal comparison of insulin, ubiquitin, cytochrome C and myoglobin from the protein mixture using the new MALDI matrices COOH-NH_2 (**I**), COOH-NHMe (**IV**) and some of the most representative commercially available matrices (CHCA, 2,5-DHB, 2,5-DHAP, SA, 9-AA and 1,5-DAN) in both positive and negative ion mode. Laser energy: COOH-NHMe (**IV**) 70%, COOH-NH_2 (**I**) 70%, CHCA 30%, 2,5-DHB 50%, SA 70%, 9-AA 70%, 1,5-DAN 70%.

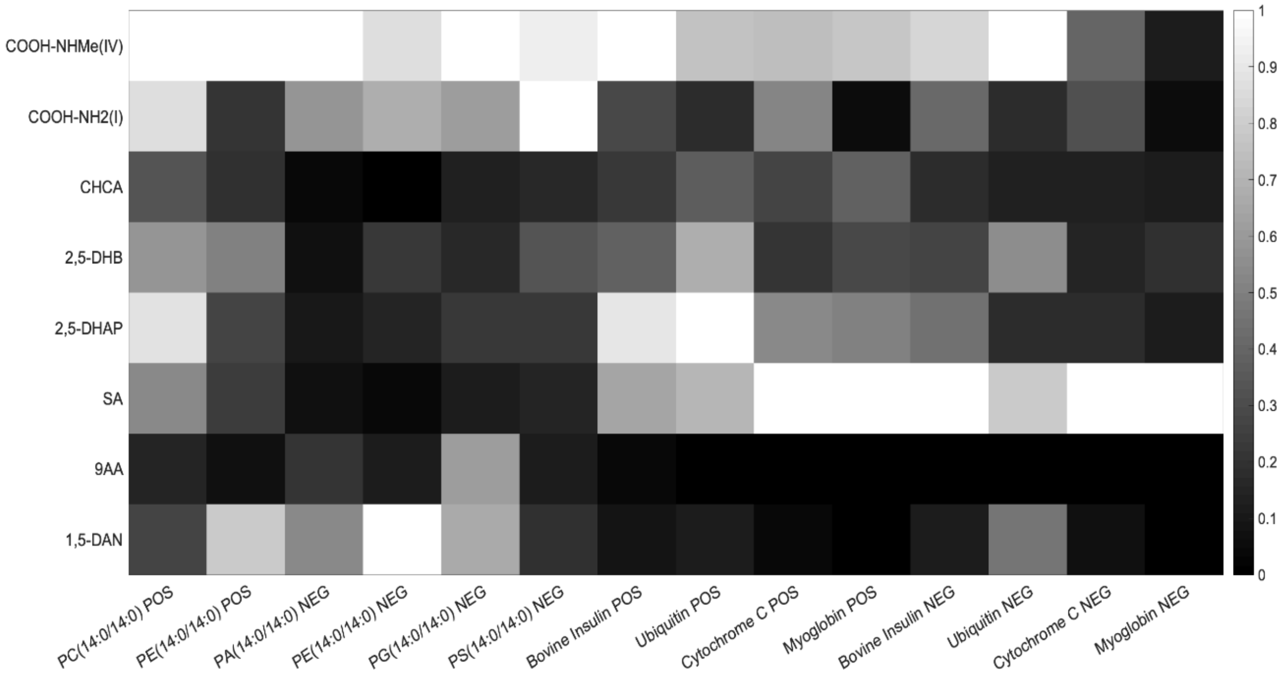

Figure S10. Signal comparison of the lipid mixture and the protein mixture using the new MALDI matrices COOH-NH_2 (**I**) and COOH-NHMe (**IV**) and some of the most representative commercially available matrices (CHCA, 2,5-DHB, 2,5-DHAP, SA, 9-AA and 1,5-DAN). The laser intensities used for different matrices were optimized to achieve best signals. According to the results of **Figure S8** and **S9**, a maximum analyte signal was selected as normalized parameter. The analyte signals from these eight matrices were divide by the maximum analyte signal. The analytes written with "**POS**" indicates signals were obtained in positive ion mode and "**NEG**" in negative ion mode. COOH-NHMe (**IV**) had superior performance in lipid analysis and was also capable of analyzing proteins in both positive and negative ion modes.

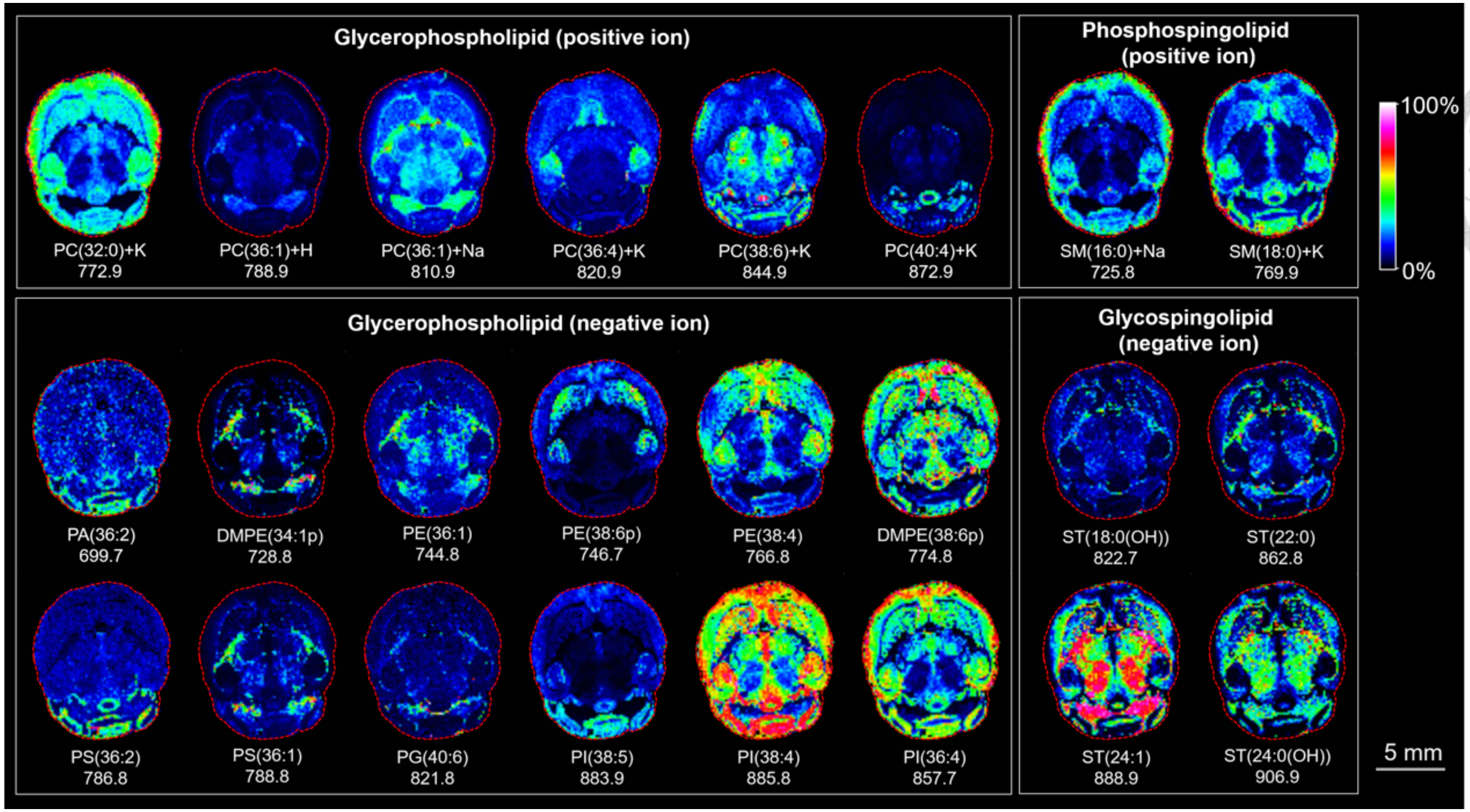

Figure S11. MSI of horizontal mice brain sections sublimated with COOH-NHMe (**IV**) in positive and negative ion mode. We observed glycerophospholipids in both (A) positive and (B) negative ion modes, (C) phosphosphingolipids in positive ion mode, and (D) glyco-sphingolipids in negative ion mode. MSI were accumulated 100 laser shots per pixel and were acquired with a 1 kHz repetition rate. Laser operating power was set at 50% with a raster size of 150 μm.

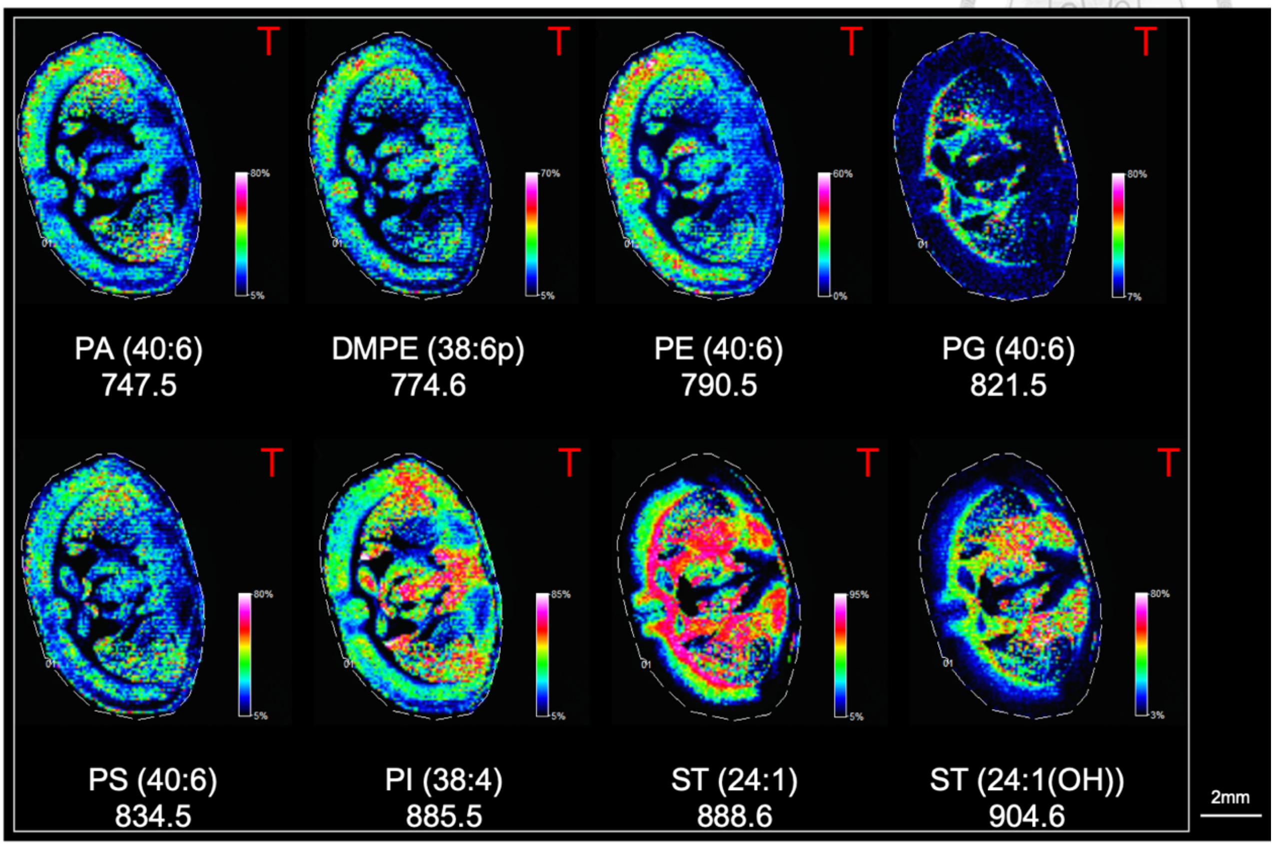

Figure S12. High spatial resolution MSI of a coronal mouse brain section sublimated with COOH-NHMe (**IV**) in negative ion mode. Negatively charged lipid species were observed using common sublimation method. MSI were accumulated by sum of 100 laser shots per pixel and were acquired with a 1 kHz repetition rate. Laser operating power was set at 50% with a raster size of 80 μm.

NMR spectra of the rest synthesized compounds

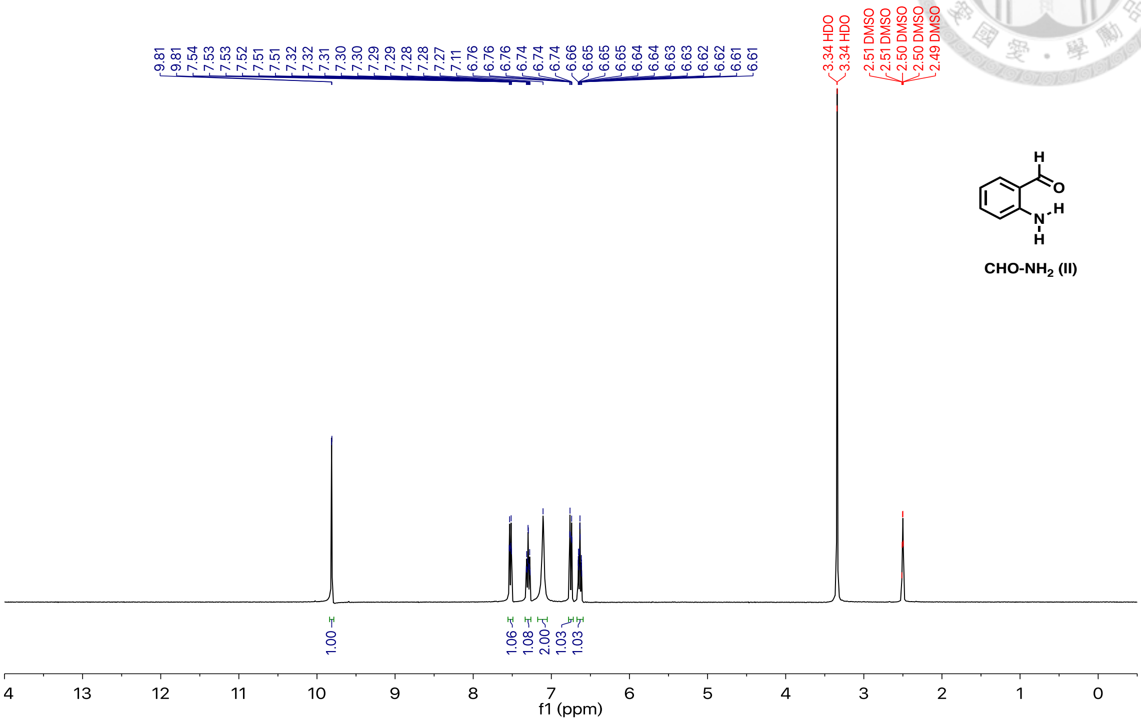

Figure S13. ^{1}H NMR spectrum (400 MHz, DMSO-d6, 298K) of **CHO-NH2 (II).**

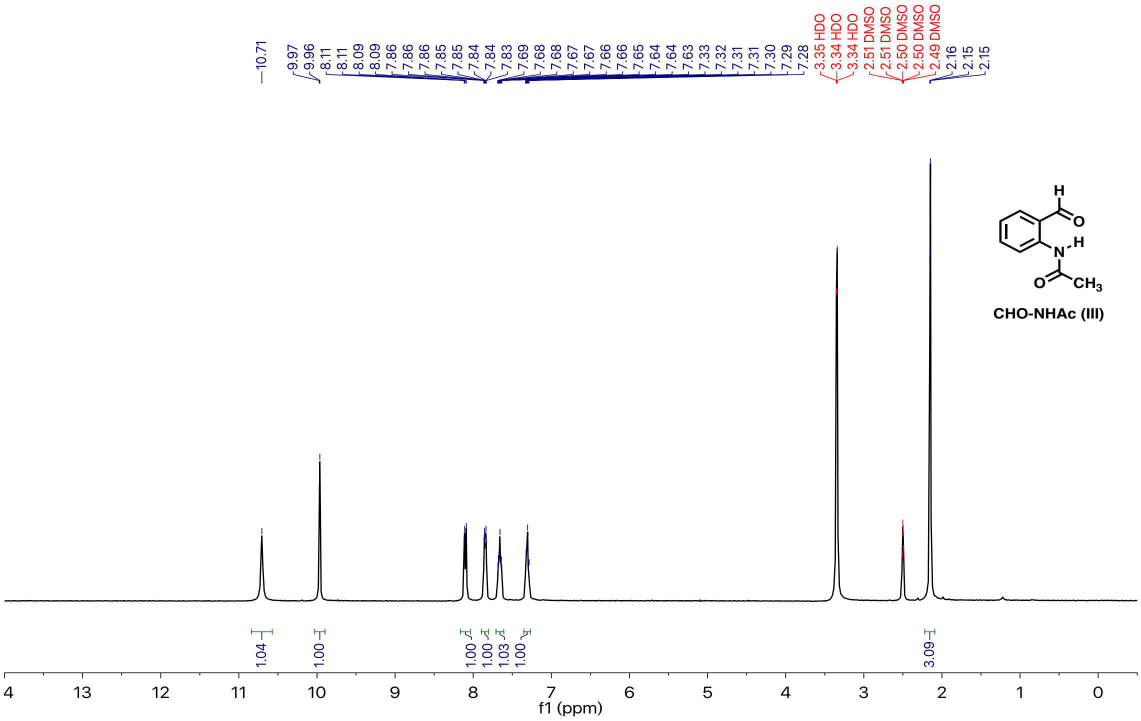

Figure S14. ^{1}H NMR spectrum (400 MHz, DMSO-d$_6$, 298K) of **CHO-NHAc (III).**

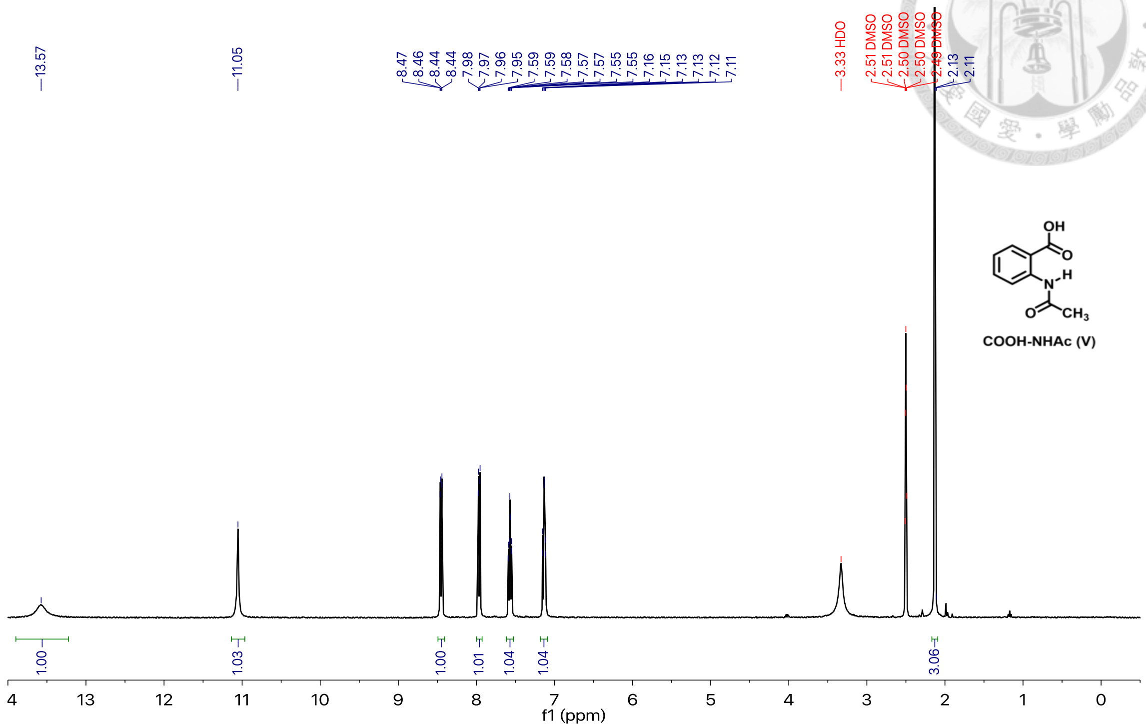

Figure S15. ^{1}H NMR spectrum (400 MHz, DMSO-d$_6$, 298K) of **COOH-NHAc (V).**

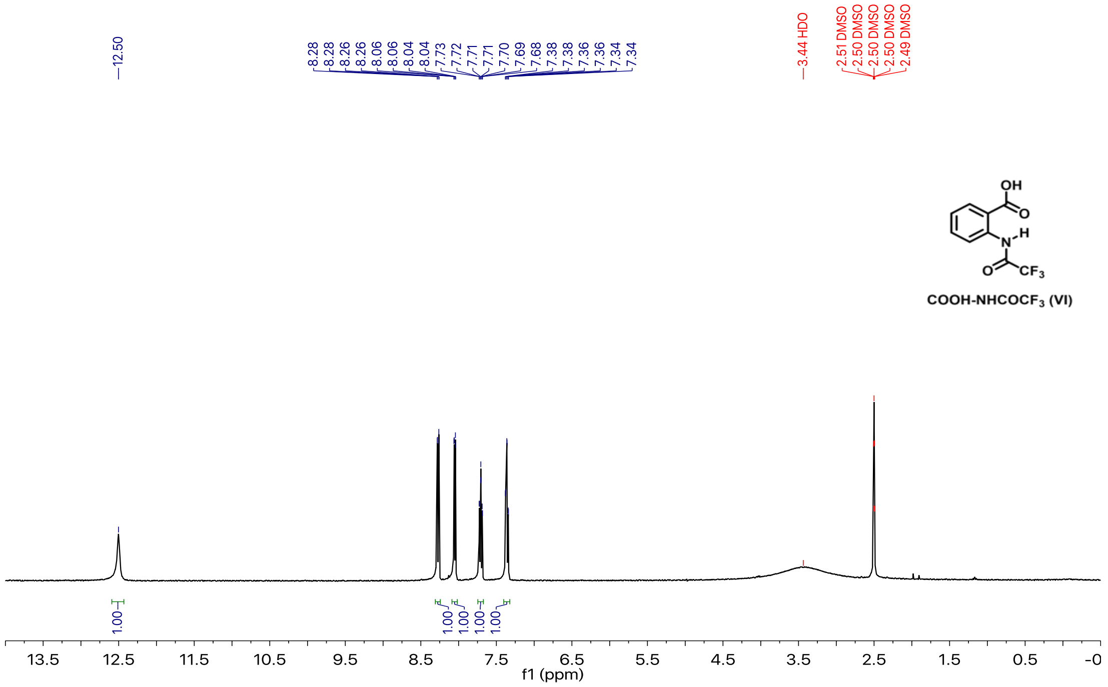

Figure S16. ^{1}H NMR spectrum (400 MHz, DMSO-d$_6$, 298K) of **COOH-NHCOCF$_3$ (VI).**

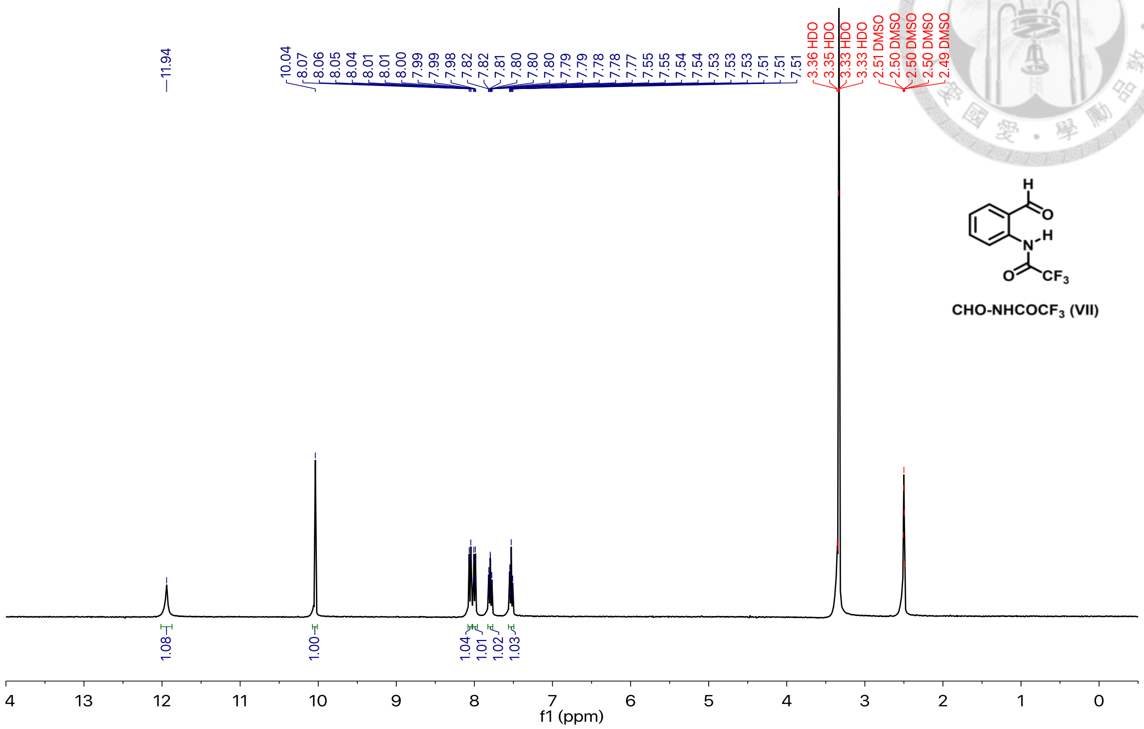

Figure S17. ^{1}H NMR spectrum (400 MHz, DMSO-d$_6$, 298K) of **CHO-NHCOCF$_3$ (VII).**

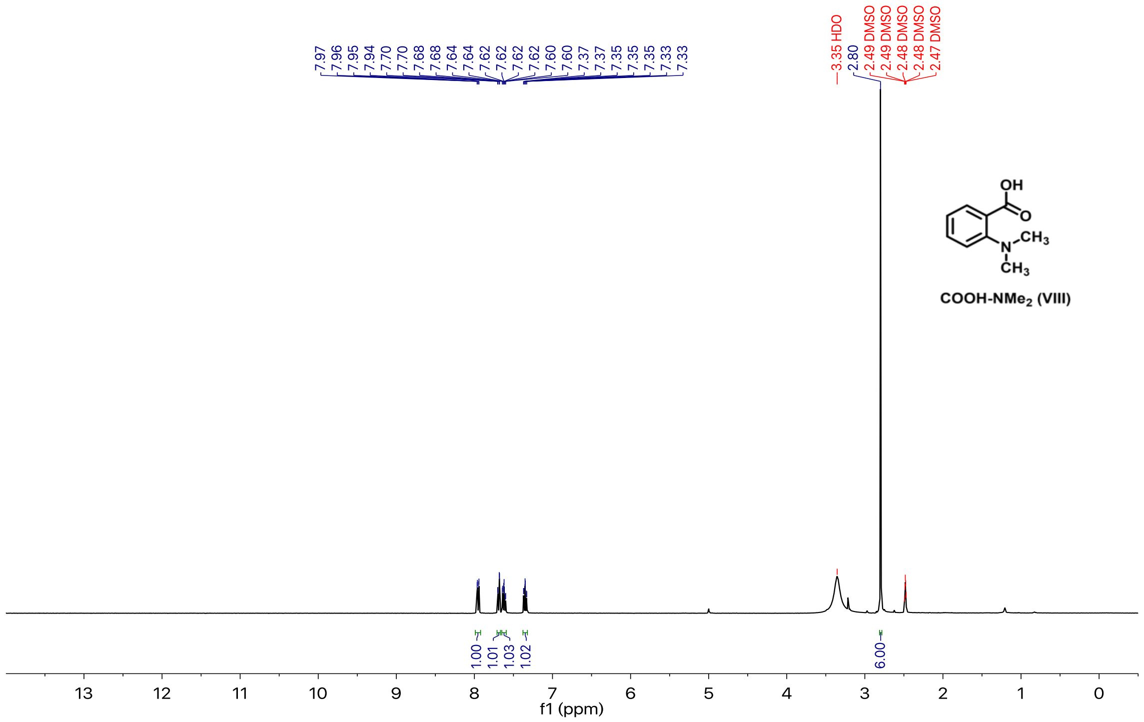

Figure S18. ^{1}H NMR spectrum (400 MHz, DMSO-d$_6$, 298K) of **COOH-NMe$_2$ (VIII).**

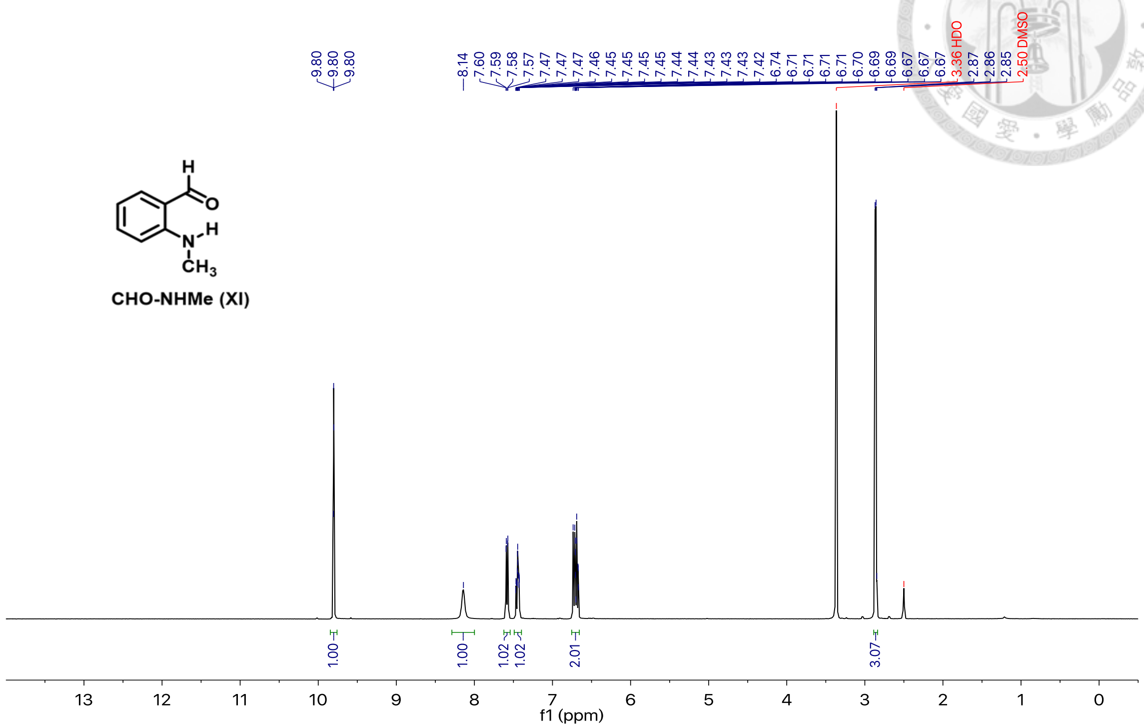

Figure S19. ^{1}H NMR spectrum (400 MHz, DMSO-d6, 298K) of **CHO-NHMe (IX)**

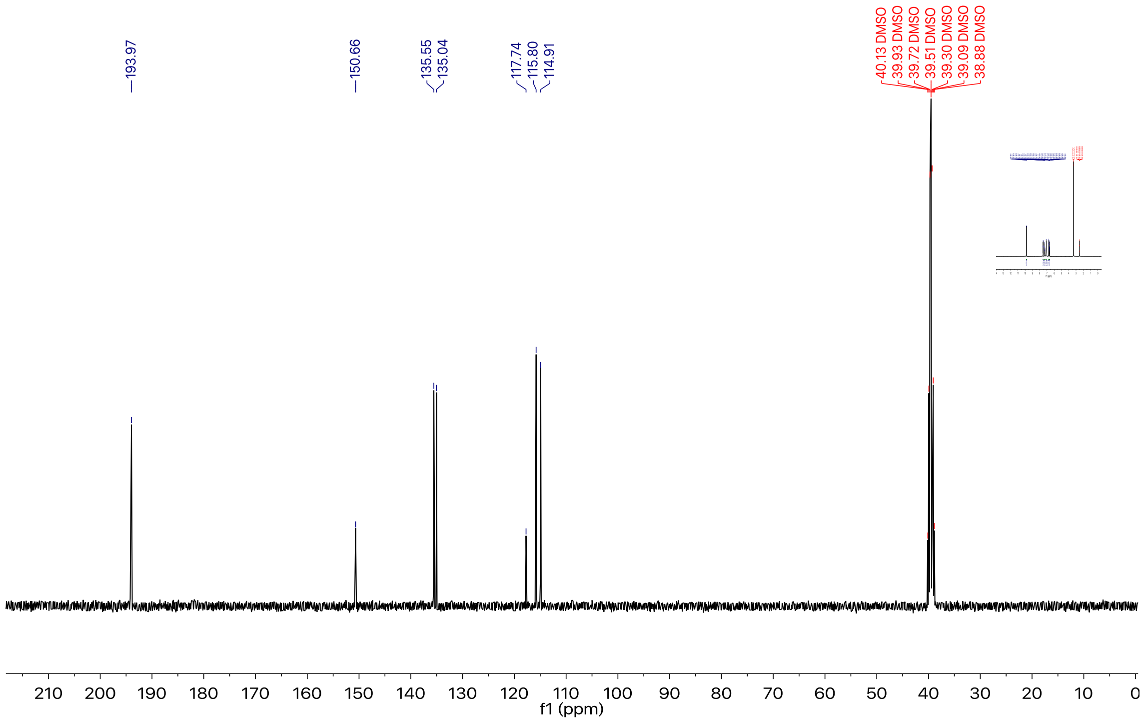

Figure S20. ^{13}C NMR spectrum (100 MHz, DMSO-d$_6$, 298K) of **CHO-NH$_2$ (II).**

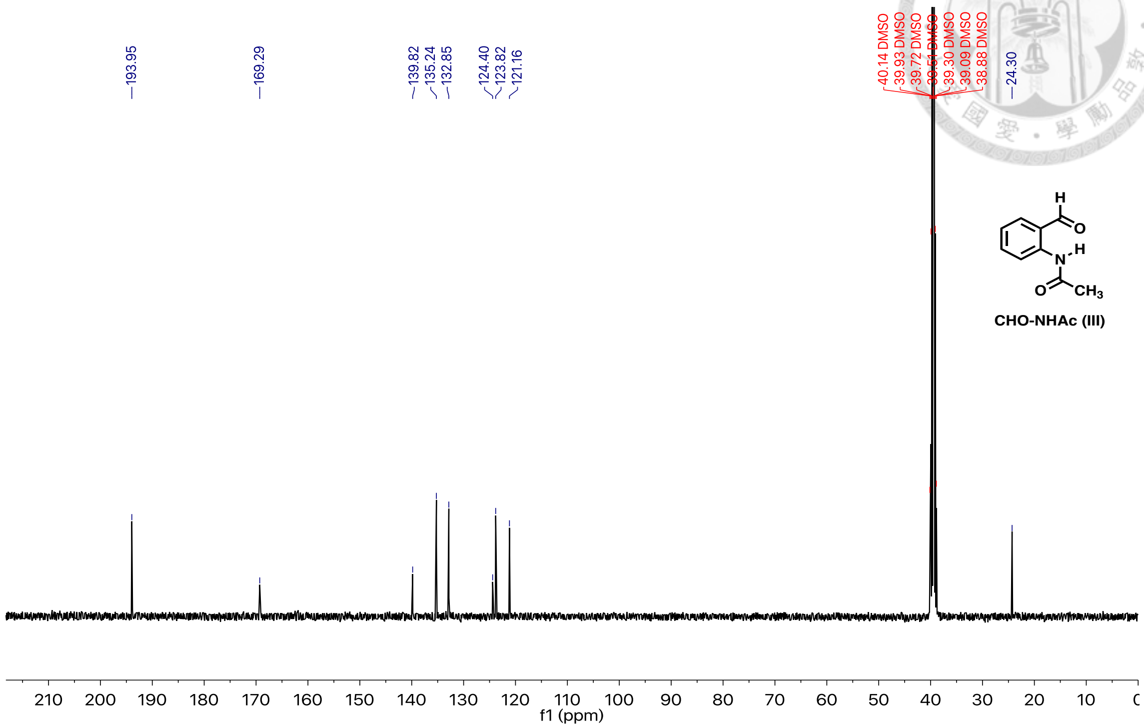

Figure S21. ^{13}C NMR spectrum (100 MHz, DMSO-d_6, 298K) of **CHO-NHAc (III).**

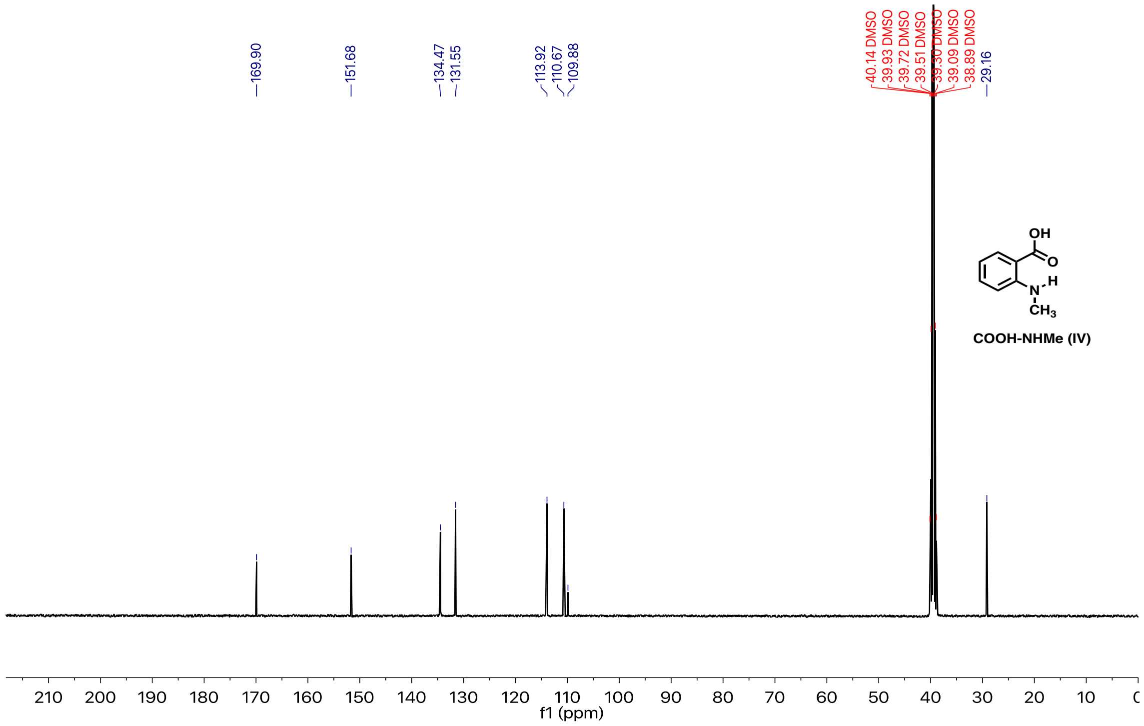

Figure S22. ^{13}C NMR spectrum (100 MHz, DMSO-d_6, 298K) of **COOH-NHMe (IV).**

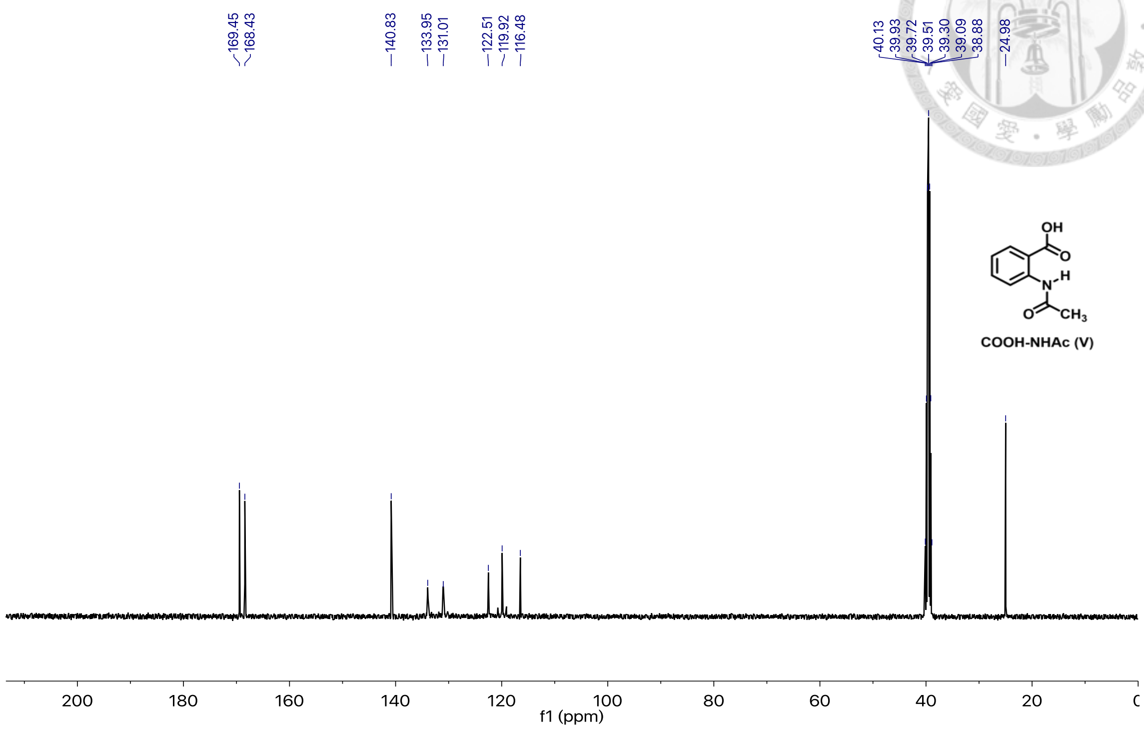

Figure S23. ^{13}C NMR spectrum (100 MHz, DMSO-d$_6$, 298K) of **COOH-NHAc (V).**

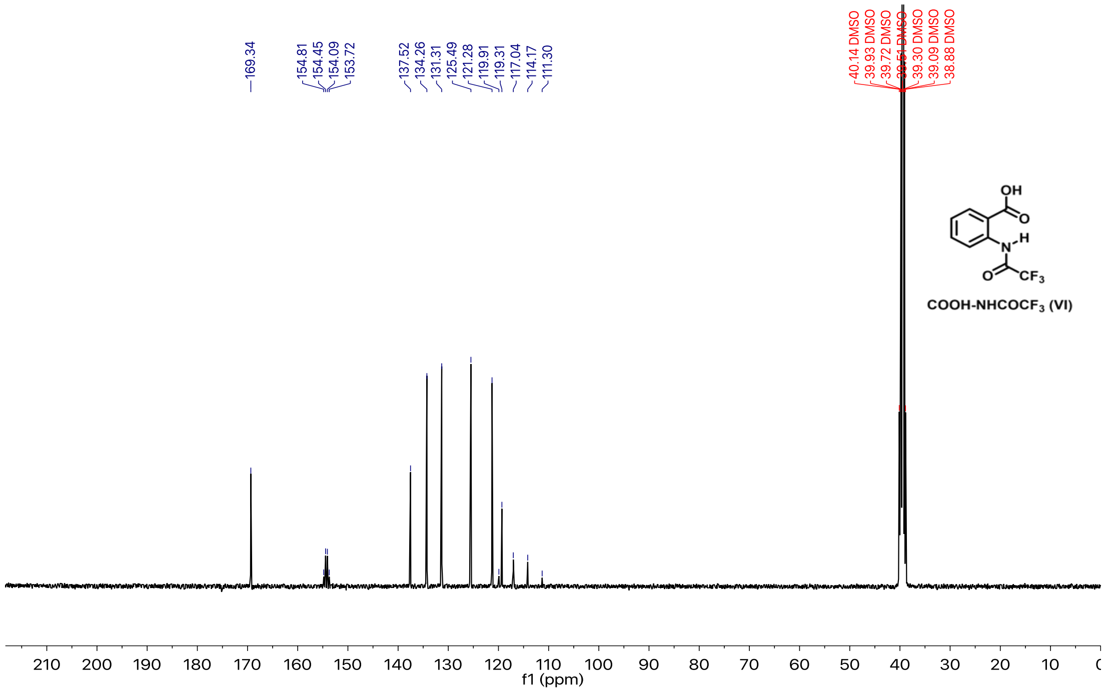

Figure S24. ^{13}C NMR spectrum (100 MHz, DMSO-d$_6$, 298K) of **COOH-NHCOCF$_3$ (VI).**

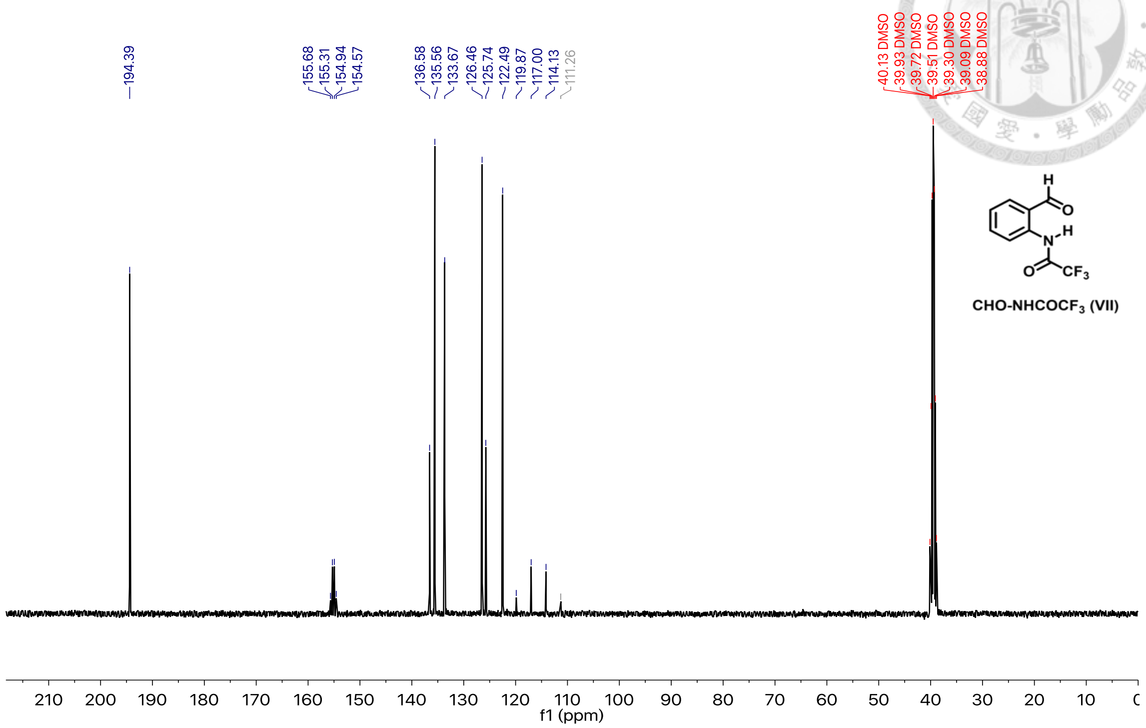

Figure S25. ^{13}C NMR spectrum (100 MHz, DMSO-d$_6$, 298K) of **CHO-NHCOCF$_3$ (VII).**

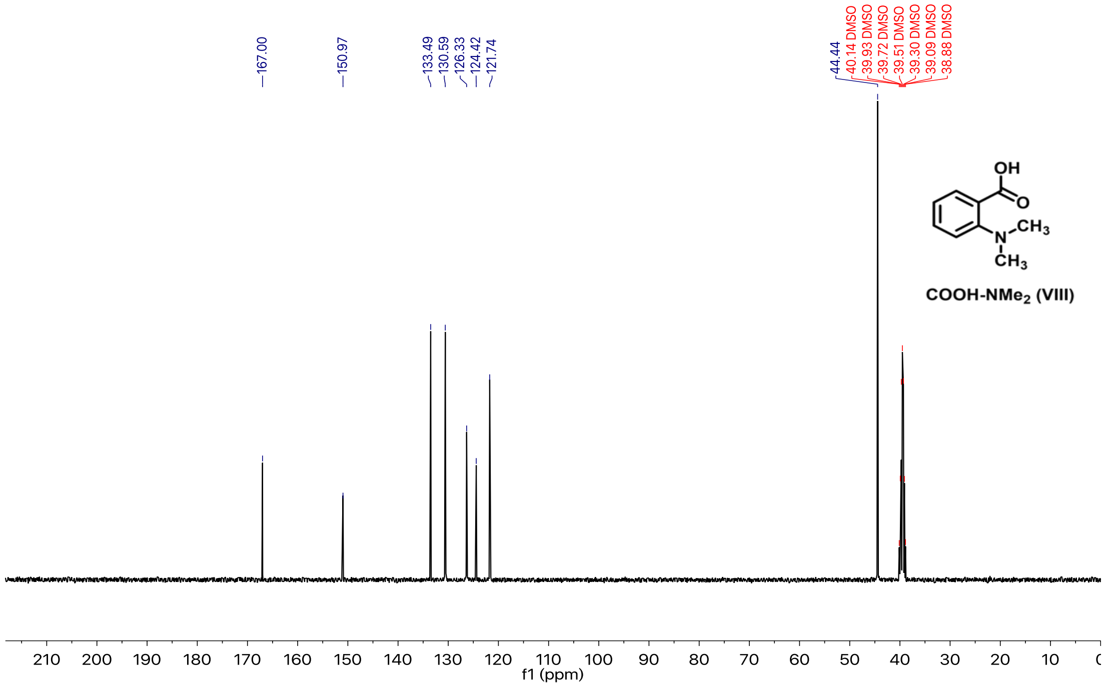

Figure S26. ^{13}C NMR spectrum (100 MHz, DMSO-d$_6$, 298K) of **COOH-NMe$_2$ (VIII).**

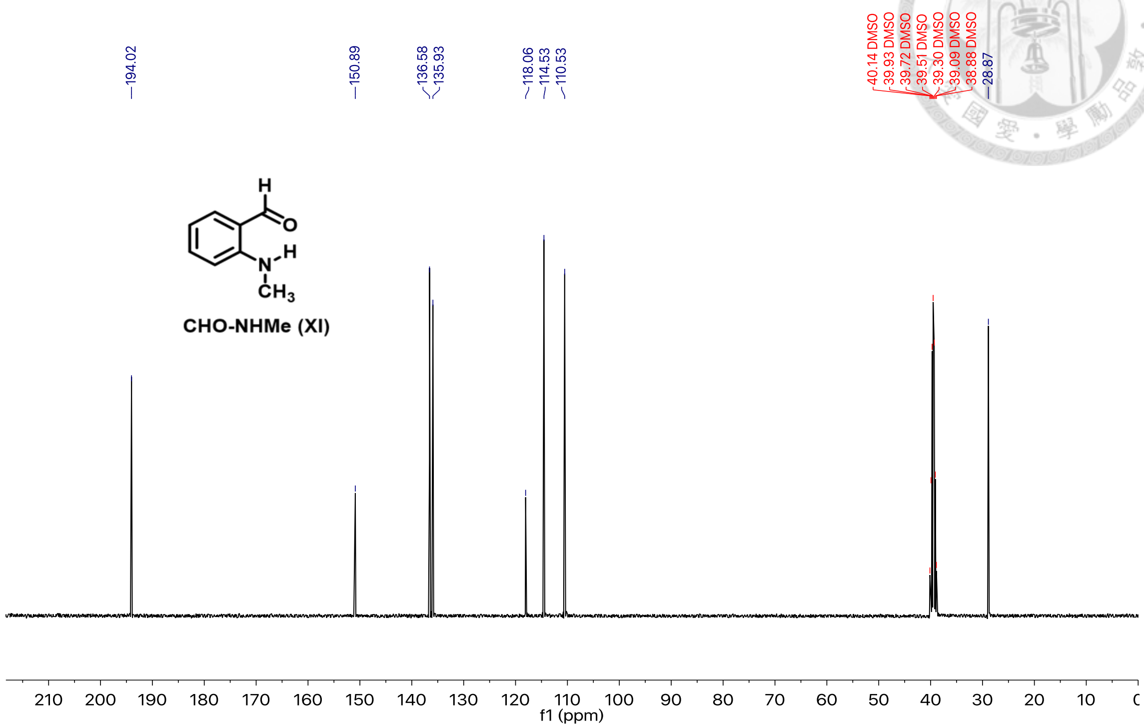

Figure S27. ^{13}C NMR spectrum (100 MHz, DMSO-d_6, 298K) of **CHO-NHMe (IX).**

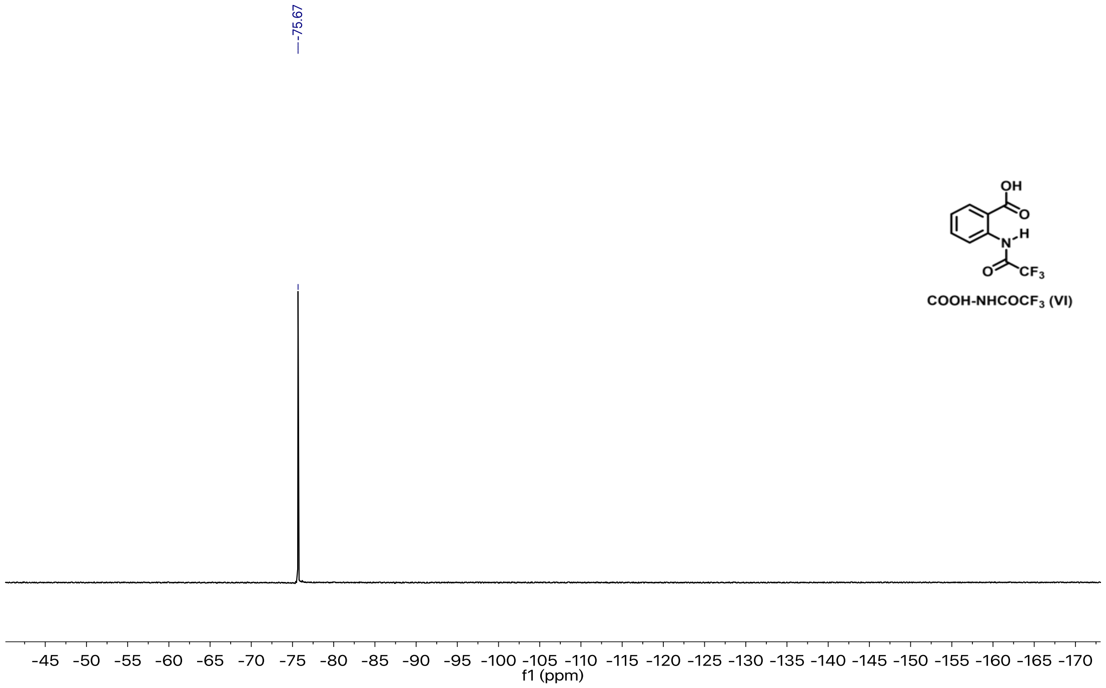

Figure S28. ^{19}F NMR spectrum (376 MHz, DMSO-d_6, 298K) of **COOH-NHCOCF$_3$ (VI).**

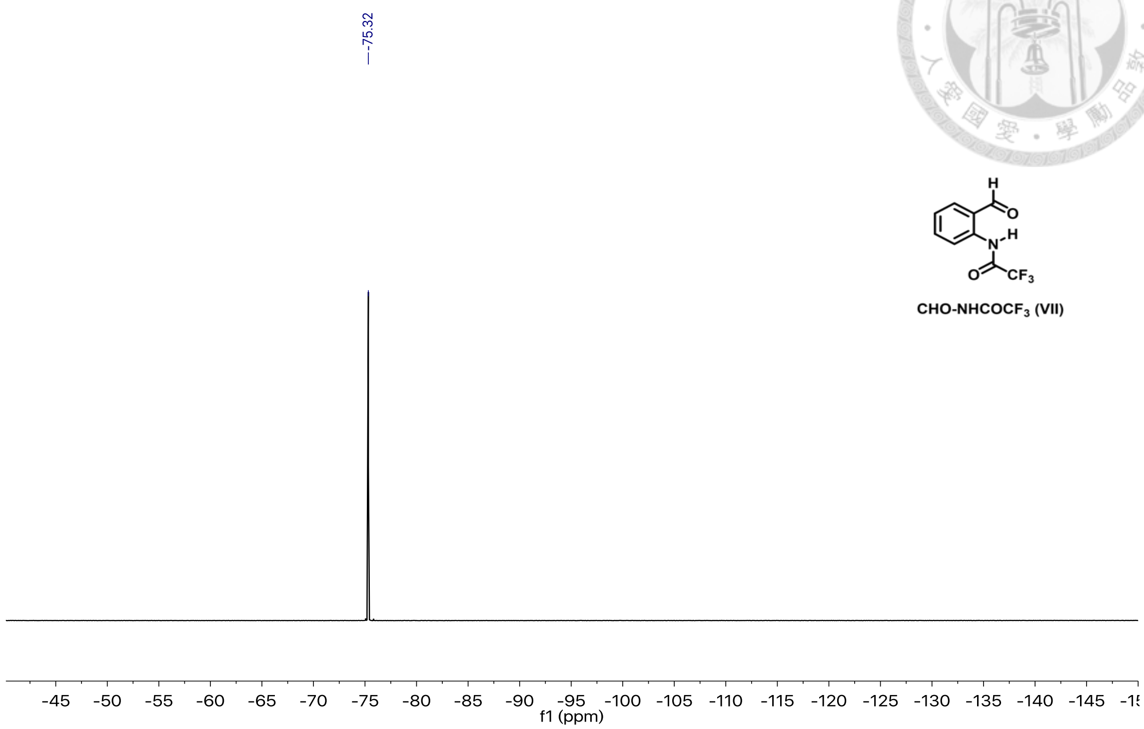

Figure S29. ^{19}F NMR spectrum (376 MHz, DMSO-d$_6$, 298K) of **CHO-NHCOCF$_3$ (VII).**

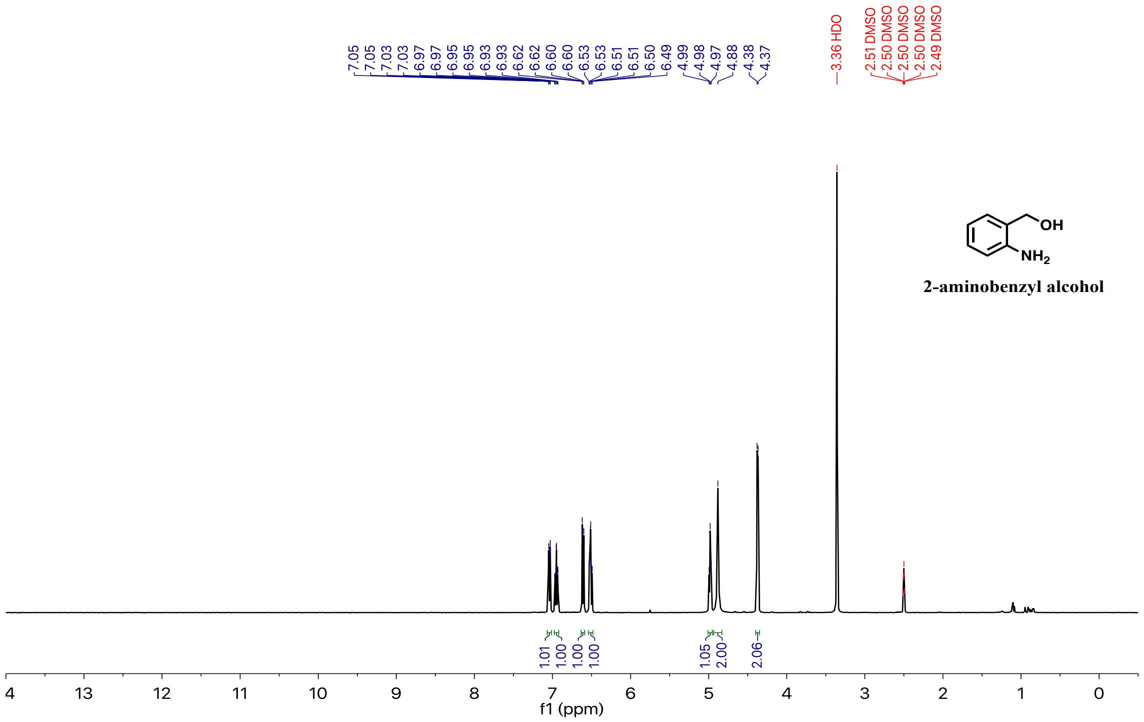

Figure S30. ^{1}H NMR spectrum (400 MHz, DMSO-d$_6$, 298K) of **2-aminobenzyl alcohol.**

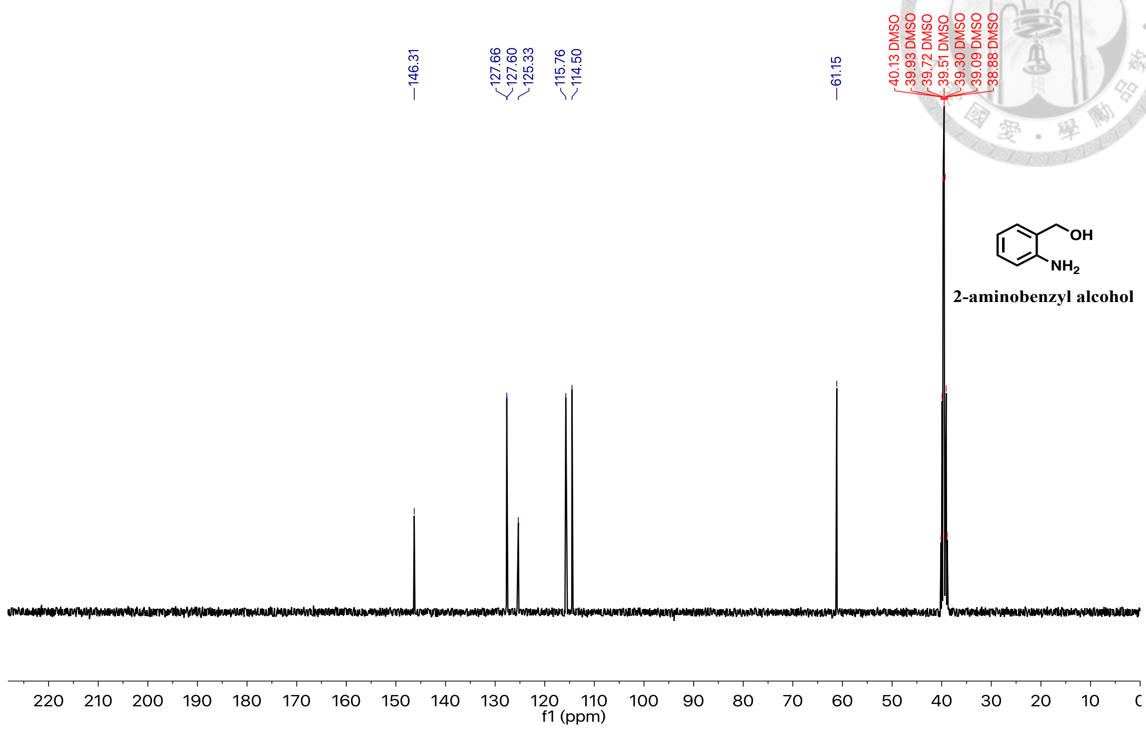

Figure S31. ^{13}C NMR spectrum (100 MHz, DMSO-d_6, 298K) of **2-aminobenzyl alcohol.**

B-3 Supplementary Tables

Table S1. Calculated Frontier Orbital of the anthranilic acid derivatives.

compound	structure	HOMO	LUMO
COOH-NH$_2$ **(I)**	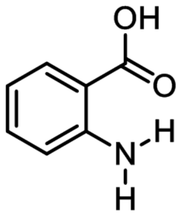	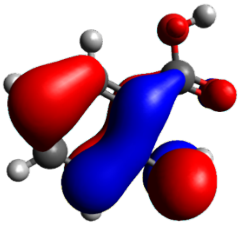	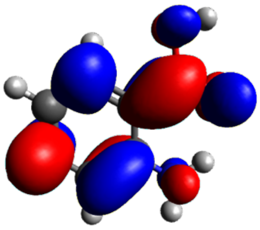
CHO-NH$_2$ **(II)**	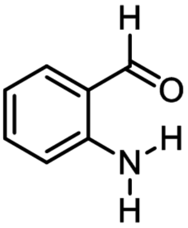	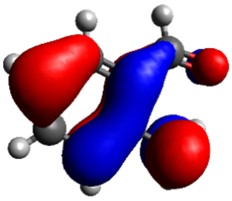	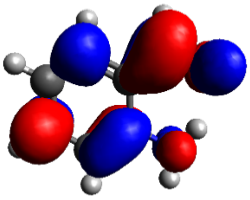
CHO-NHAc **(III)**	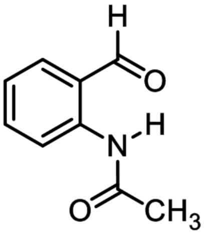	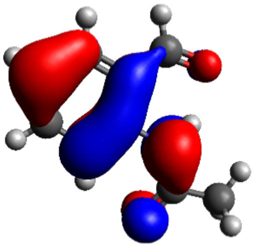	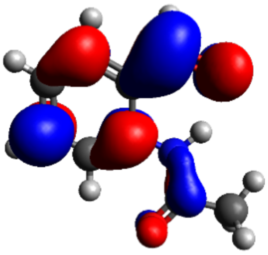
COOH-NHMe **(IV)**	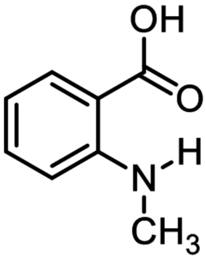	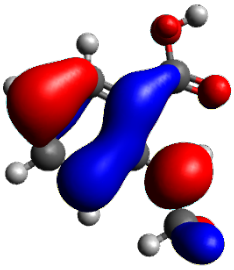	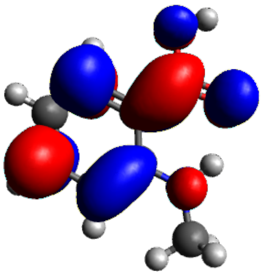

Table S2. Mass peak assignments for lipid species in positive ion mode for mice brain. Peaks assignments were based on LC-MS/MS analysis or comparing to previous research.[23,92,93]

Tentatively proposed identity	**Exp. *m/z***	**Cal. *m/z***
[SM(d18:0_16:0)+Na]$^+$	725.80	725.56
[PC(32:0)+H]$^+$	734.63	734.57
[SM(d18:0_18:0)+Na]$^+$	753.66	753.59
[PC(32:0)+Na]$^+$	756.63	756.55
[PC(34:1)+H]$^+$	760.66	760.59
[SM(d18:0_18:0)+K]$^+$	769.64	769.56
[PC(34:0)+H]$^+$	762.67	762.60
[PC(32:1)+K]$^+$	770.63	770.51
[PC(32:0)+K]$^+$	772.61	772.53
[PC(34:1)+Na]$^+$	782.65	782.57
[PC(36:1)+H]$^+$	788.70	788.62
[PC(34:1)+K]$^+$	798.64	798.54
[PC(34:0)+K]$^+$	800.66	800.56
[PC(36:1)+Na]$^+$	810.69	810.60
[PC(36:4)+K]$^+$	820.64	820.53
[PC(36:1)+K]$^+$	826.64	826.57
[PC(38:6)+K]$^+$	844.63	844.53
[PC(38:4)+K]$^+$	848.74	844.56
[PC(40:4)+K]$^+$	872.64	872.53

Table S3. Mass peak assignments for lipid species in negative ion mode for mice brain. Peaks assignments were based on LC-MS/MS analysis or comparing to previous research. [92,93,94,95]

Tentatively proposed identity	**Exp. *m/z***	**Cal. *m/z***
[PA(34:1)-H]$^-$	673.54	673.48
[PE(34:1p)-H]$^-$	700.67	700.53
[PE(34:1)-H]$^-$	716.65	716.52
[PE(34:0)-H]$^-$	718.68	718.54
[DMPE(34:4p)-H]$^-$	722.64	722.51
[DMPE(34:2p)-H]$^-$	726.67	726.54
[DMPE(34:1p)-H]$^-$	728.69	728.56
[PE(36:2)-H]$^-$	742.67	742.54
[PE(36:1)-H]$^-$	744.69	744.56
[PE(38:6p)-H]$^-$	746.63	746.53
[PA(40:6)-H]$^-$	747.59	747.50
[DMPE(36:4p)-H]$^-$	750.68	750.54
[PE(38:6)-H]$^-$	762.64	762.51
[PE(38:4)-H]$^-$	766.67	766.54
[DMPE(38:6p)-H]$^-$	774.67	774.57
[PE(40:6e)-H]$^-$	776.67	776.56
[PE(40:4p)-H]$^-$	778.71	778.58
[PS(36:2)-H]$^-$	786.66	786.53
[PS(36:1)-H]$^-$	788.68	788.54

[PE(40:6)-H]$^-$	790.67	790.54
[PE(40:4)-H]$^-$	794.69	794.57
[ST(18:0)-H]$^-$	806.70	806.55
[PS(38:4)-H]$^-$	810.66	810.53
[PG(40:6)-H]$^-$	821.75	821.53
[ST(18:0(OH))-H]$^-$	822.69	822.54
[PS(40:6)-H]$^-$	834.67	834.53
[ST(20:0(OH))-H]$^-$	850.73	850.57
[PI(36:4)-H]$^-$	857.67	857.52
[ST(22:1)-H]$^-$	860.74	860.59
[PI(36:2)-H]$^-$	861.74	861.55
[ST(22:0)-H]$^-$	862.76	862.61
[PI(36:1)-H]$^-$	863.74	863.57
[ST(22:1(OH))-H]$^-$	876.77	876.58
[ST(22:0(OH))-H]$^-$	878.76	879.60
[PI(38:5)-H]$^-$	883.75	883.54
[PI(38:4)-H]$^-$	885.76	885.55
[PI(38:3)-H]$^-$	887.74	887.56
[ST(24:1)-H]$^-$	888.79	888.62
[ST(24:0)-H]$^-$	890.79	890.64
[ST(24:1(OH))-H]$^-$	904.78	904.62
[ST(24:0(OH))-H]$^-$	906.80	906.64
[PI(40:6)-H]$^-$	909.78	909.55

X-ray Crystallographic Data

Crystallographic data. The X-ray crystal structure for the anthranilic acid derivatives reported in this article have been submitted to the Cambridge Crystallographic Data Centre (CCDC), with the deposition number CCDC 1948704 (COOH-NH_2, I), 1947215 (CHO-NHAc, III), 1947199 (COOH-NHMe, IV), 1947202 (COOH-NHAc, V), 1947210 (COOH-$NHCOCF_3$, VI), 1947216 (CHO-$NHCOCF_3$, VII) and 1947201 (COOH-NMe_2, VIII), respectively. These data can be obtained free of charge from The Cambridge Crystallographic Data Centre via www.ccdc.cam.ac.

Table S4. Crystal data and structure refinement for COOH-NH_2 (I).

Identification code	ic19906	
Empirical formula	C7 H7 N O2	
Formula weight	137.14	
Temperature	200(2) K	
Wavelength	1.54178 Å	
Crystal system	Orthorhombic	
Space group	Pbca	
Unit cell dimensions	a = 11.6358(2) Å	α= 90°.
	b = 7.12450(10) Å	β= 90°.
	c = 15.9044(3) Å	γ= 90°.
Volume	1318.46(4) $Å^3$	
Z	8	
Density (calculated)	1.382 Mg/m^3	

Absorption coefficient	0.859 mm^{-1}
F(000)	576
Crystal size	0.316 x 0.126 x 0.100 mm^{3}
Theta range for data collection	6.743 to 74.941°.
Index ranges	-14<=h<=13, -8<=k<=7, -19<=l<=19
Reflections collected	5821
Independent reflections	1347 [R(int) = 0.0303]
Completeness to theta = 67.679°	99.1 %
Absorption correction	Semi-empirical from equivalents
Max. and min. transmission	0.7539 and 0.6819
Refinement method	Full-matrix least-squares on F^{2}
Data / restraints / parameters	1347 / 0 / 119
Goodness-of-fit on F^{2}	1.062
Final R indices [I>2sigma(I)]	R1 = 0.0339, wR2 = 0.0892
R indices (all data)	R1 = 0.0353, wR2 = 0.0912
Extinction coefficient	n/a
Largest diff. peak and hole	0.270 and -0.177 e.Å^{-3}

Table S5. X-ray single crystal data and structure refinements of CHO-NHAc (III).

Identification code	ic19354	
Empirical formula	C18 H18 N2 O4	
Formula weight	326.34	
Temperature	200(2) K	
Wavelength	1.54178 Å	
Crystal system	Monoclinic	
Space group	$P2_1/c$	
Unit cell dimensions	a = 8.6561(2) Å	α= 90°.
	b = 26.3567(6) Å	β= 90.3438(8)°.
	c = 7.0706(2) Å	γ= 90°.
Volume	1613.10(7) Å^3	
Z	4	
Density (calculated)	1.344 Mg/m^3	
Absorption coefficient	0.792 mm^{-1}	
F(000)	688	
Crystal size	0.191 x 0.104 x 0.086 mm^3	
Theta range for data collection	3.354 to 74.986°.	
Index ranges	-9<=h<=10, -33<=k<=33, -8<=l<=8	
Reflections collected	10871	
Independent reflections	3309 [R(int) = 0.0191]	
Completeness to theta = 67.679°	99.7 %	
Absorption correction	Semi-empirical from equivalents	

Max. and min. transmission	0.7539 and 0.6236
Refinement method	Full-matrix least-squares on F^2
Data / restraints / parameters	3309 / 0 / 249
Goodness-of-fit on F^2	1.030
Final R indices [I>2sigma(I)]	R1 = 0.0354, wR2 = 0.0942
R indices (all data)	R1 = 0.0373, wR2 = 0.0972
Extinction coefficient	n/a
Largest diff. peak and hole	0.222 and -0.160 e.Å^{-3}

Table S6. X-ray single crystal data and structure refinements of COOH-NHMe (IV).

Identification code	ic19414	
Empirical formula	C8 H9 N O2	
Formula weight	151.16	
Temperature	200(2) K	
Wavelength	1.54178 Å	
Crystal system	Monoclinic	
Space group	$P2_1/c$	
Unit cell dimensions	a = 7.7626(2) Å	α= 90°.
	b = 14.9495(4) Å	β= 113.3719(6)°.
	c = 6.9402(2) Å	γ= 90°.
Volume	739.31(3) Å^3	
Z	4	
Density (calculated)	1.358 Mg/m^3	
Absorption coefficient	0.815 mm^{-1}	
F(000)	320	
Crystal size	0.293 x 0.163 x 0.104 mm^3	
Theta range for data collection	6.883 to 74.981°.	
Index ranges	-9<=h<=8, -18<=k<=18, -7<=l<=8	
Reflections collected	4214	
Independent reflections	1513 [R(int) = 0.0194]	
Completeness to theta = 67.679°	99.4 %	
Absorption correction	Semi-empirical from equivalents	

Max. and min. transmission	0.7539 and 0.6713
Refinement method	Full-matrix least-squares on F^2
Data / restraints / parameters	1513 / 0 / 102
Goodness-of-fit on F^2	1.058
Final R indices [I>2sigma(I)]	R1 = 0.0366, wR2 = 0.1016
R indices (all data)	R1 = 0.0376, wR2 = 0.1029
Extinction coefficient	n/a
Largest diff. peak and hole	0.260 and -0.189 e.Å^{-3}

Table S7. X-ray single crystal data and structure refinements of COOH-NHAc (V).

Identification code	ic19820	
Empirical formula	$C_9 H_9 N O_3$	
Formula weight	179.17	
Temperature	200(2) K	
Wavelength	1.54178 Å	
Crystal system	Orthorhombic	
Space group	Fdd2	
Unit cell dimensions	a = 10.6729(2) Å	α= 90°.
	b = 30.1181(6) Å	β= 90°.
	c = 10.5791(2) Å	γ= 90°.
Volume	3400.62(11) $Å^3$	
Z	16	
Density (calculated)	1.400 Mg/m^3	
Absorption coefficient	0.894 mm^{-1}	
F(000)	1504	
Crystal size	0.146 x 0.102 x 0.082 mm^3	
Theta range for data collection	6.070 to 74.999°.	
Index ranges	-13<=h<=13, -37<=k<=37, -13<=l<=9	
Reflections collected	4487	
Independent reflections	1394 [R(int) = 0.0226]	
Completeness to theta = 67.679°	99.8 %	
Absorption correction	Semi-empirical from equivalents	

Max. and min. transmission	0.7539 and 0.6706
Refinement method	Full-matrix least-squares on F^2
Data / restraints / parameters	1394 / 2 / 120
Goodness-of-fit on F^2	1.112
Final R indices [I>2sigma(I)]	R1 = 0.0301, wR2 = 0.0832
R indices (all data)	R1 = 0.0304, wR2 = 0.0839
Absolute structure parameter	0.12(11)
Extinction coefficient	n/a
Largest diff. peak and hole	0.161 and -0.151 e.Å^{-3}

Table S8. X-ray single crystal data and structure refinements of COOH-NHCOCF$_3$ (VI).

Identification code	ic19616	
Empirical formula	C9 H6 F3 N O3	
Formula weight	233.15	
Temperature	200(2) K	
Wavelength	0.71073 Å	
Crystal system	Triclinic	
Space group	P-1	
Unit cell dimensions	a = 4.9354(2) Å	α= 97.9438(12)°.
	b = 10.0249(3) Å	β= 102.1271(12)°.
	c = 10.0770(4) Å	γ= 99.2361(11)°.
Volume	473.44(3) Å^3	
Z	2	
Density (calculated)	1.635 Mg/m^3	
Absorption coefficient	0.160 mm^{-1}	
F(000)	236	
Crystal size	0.251 x 0.150 x 0.146 mm^3	
Theta range for data collection	2.688 to 29.998°.	
Index ranges	-6<=h<=6, -14<=k<=14, -14<=l<=14	
Reflections collected	5440	
Independent reflections	2733 [R(int) = 0.0156]	
Completeness to theta = 25.242°	98.5 %	
Absorption correction	Semi-empirical from equivalents	

Max. and min. transmission	0.7460 and 0.6501
Refinement method	Full-matrix least-squares on F^2
Data / restraints / parameters	2733 / 16 / 153
Goodness-of-fit on F^2	1.043
Final R indices [I>2sigma(I)]	R1 = 0.0462, wR2 = 0.1253
R indices (all data)	R1 = 0.0508, wR2 = 0.1297
Extinction coefficient	n/a
Largest diff. peak and hole	0.425 and -0.445 e.$Å^{-3}$

Table S9. X-ray single crystal data and structure refinements of CHO-NHCOCF$_3$ (VII).

Identification code	ic19356	
Empirical formula	C9 H6 F3 N O2	
Formula weight	217.15	
Temperature	200(2) K	
Wavelength	1.54178 Å	
Crystal system	Orthorhombic	
Space group	Pbcm	
Unit cell dimensions	a = 8.4925(2) Å	α= 90°.
	b = 16.3061(4) Å	β= 90°.
	c = 6.5289(2) Å	γ= 90°.
Volume	904.12(4) Å^3	
Z	4	
Density (calculated)	1.595 Mg/m^3	
Absorption coefficient	1.366 mm^{-1}	
F(000)	440	
Crystal size	0.210 x 0.108 x 0.043 mm^3	
Theta range for data collection	5.208 to 74.913°.	
Index ranges	-10<=h<=10, -20<=k<=20, -7<=l<=8	
Reflections collected	6084	
Independent reflections	1019 [R(int) = 0.0254]	
Completeness to theta = 67.679°	99.8 %	
Absorption correction	Semi-empirical from equivalents	

Max. and min. transmission	0.7539 and 0.5708
Refinement method	Full-matrix least-squares on F^2
Data / restraints / parameters	1019 / 7 / 110
Goodness-of-fit on F^2	1.069
Final R indices [I>2sigma(I)]	R1 = 0.0577, wR2 = 0.1569
R indices (all data)	R1 = 0.0602, wR2 = 0.1624
Extinction coefficient	n/a
Largest diff. peak and hole	0.574 and -0.195 e.Å^{-3}

Table S10. X-ray single crystal data and structure refinements of COOH-NMe$_2$ (IIIV).

Identification code	ic19403	
Empirical formula	C9 H11 N O2	
Formula weight	165.19	
Temperature	200(2) K	
Wavelength	1.54178 Å	
Crystal system	Monoclinic	
Space group	$P2_1/n$	
Unit cell dimensions	a = 7.5334(2) Å	α= 90°.
	b = 15.6848(4) Å	β= 100.2859(7)°.
	c = 7.6229(2) Å	γ= 90°.
Volume	886.25(4) Å^3	
Z	4	
Density (calculated)	1.238 Mg/m^3	
Absorption coefficient	0.721 mm^{-1}	
F(000)	352	
Crystal size	0.347 x 0.173 x 0.132 mm^3	
Theta range for data collection	6.542 to 74.987°.	
Index ranges	-9<=h<=9, -19<=k<=19, -9<=l<=8	
Reflections collected	5594	
Independent reflections	1821 [R(int) = 0.0268]	
Completeness to theta = 67.679°	99.2 %	
Absorption correction	Semi-empirical from equivalents	

Max. and min. transmission	0.7539 and 0.6478
Refinement method	Full-matrix least-squares on F^2
Data / restraints / parameters	1821 / 0 / 115
Goodness-of-fit on F^2	1.078
Final R indices [I>2sigma(I)]	R1 = 0.0395, wR2 = 0.1012
R indices (all data)	R1 = 0.0409, wR2 = 0.1025
Extinction coefficient	n/a
Largest diff. peak and hole	0.227 and -0.164 e.Å^{-3}